Development of Capacitive Imaging Technology for Measuring Skin Hydration and Other Skin Properties

Christos Bontozoglou

https://orcid.org/0000-0002-2081-3143

A thesis submitted in partial fulfillment of the requirements of London South Bank University for the degree of Doctor of Philosophy

June 2021

I would like to thank my supervisor, Dr. Perry Xiao, for his professional guidance, personal enthusiasm and friendly support throughout my PhD studies. Also, thanks to Biox Systems Ltd for the partial funding and its team members for their generous knowledge exchange. Last but not least, many thanks to my family and friends for encouraging and advising me.

Abstract

In this thesis, capacitive imaging systems are assessed for their suitability in skin research studies, as multi-purpose and portable laboratory equipment. The water content of the human skin, the status of the skin barrier, its permeability by solvents, and the skin texture are crucial pieces of information in pharmaceutical and cosmetic industries for the development of skin treatment products. Normally, multiple high-end scientific instruments with expensive dedicated analysis software are employed to measure the above skin properties. The aim of this work is to demonstrate how fingerprint sensors, originally designed for biometric security, can be exploited to achieve reliable skin hydration readings and analyse multiple other skin properties while maintaining low cost and portability.

To begin with, the anatomy of human skin is summarised alongside the functional properties of each skin layer. The skin hydration instruments study the outermost layer of skin and its appendages, so their thickness, biology, functions, hydration levels and water holding capabilities are presented in the literature review in order to understand the target measurands. Since capacitive imaging, rather than single sensor, probes are employed in this work, the skin texture and its importance in cosmetic science are also studied as a part of the target measurand. In order to understand how this technology fits in the current skin research instrument market, well established measurement apparatuses are presented. These include opto-thermal transient emission radiometry and confocal Raman microspectroscopy for skin hydration and solvent permeation measurements as well as depth profiling. Then, electrical hygrometry and the dynamic vapour sortpion measurement principles are outlined, which focus on water diffusion and sorption measurements correspondingly. Since the skin texture will also be studied in this work, dermatoscopy is also summarised. A literature review on the non-invasive electrical-based measurement method is achieved, alongside the stratum corneum and viable skin capacitance and conductance as functions of sampling frequency. The latter allows to establish the criteria for the suitability of electrical based apparatuses in skin hydration measurements. More specifically, it is concluded that the measurement depth of the instrument should not be reaching viable skin and that the sampling frequency should be constant and below 100kHz for capacitive measurements. The presentation of existing electrical based skin hydration probes in the market demonstrates the current development stage of this technology, and it enables the expression of the research aim and its objectives for this work.

In order to improve trust in the use of capacitive imaging technology for measuring skin hydration, apart from visualisation, established electrical based skin hydration probes are examined and compared with a capacitive

imaging sensor. The criteria for this comparison derive from the literature review, i.e. the sampling frequency and the penetration depth of the electric field. The sampling frequency is measured directly on the hardware using an oscilloscope, while the measurement depth is estimated using an electrostatic model. The development of this model for different sensor geometries is presented and it is evaluated against different models as well as experimental results in the literature. It is concluded that low cost instruments tend to have high measurement depth that makes them unsuitable for stratum corneum hydration measurements. Higher end instruments, although they are using high sampling frequency, have safe penetration depth but low measurement sensitivity. The capacitive imaging sensor shown acceptable penetration depth, on the high end of the expected range, and good measurement sensitivity due to the miniaturisation of the technology.

A common disadvantage of most of these instruments is that the readouts are provided in arbitrary units, so experimental results cannot be compared directly with the literature when different scientific equipment has been used. To overcome this disadvantage, and based on the previous analysis of capacitive measurement principle, a system calibration is proposed to convert system capacitance or arbitrary units to dielectric permittivity units, a property of the sample measurand. This allows the calculation of hydration and solvent percentage concentration within the sample and so direct comparison with a wider range of reported results in the literature. Furthermore, image analysis techniques are applied on the dielectric permittivity images to allow targeting and relocating skin regions of interest, as well as excluding pixels with bad sample contact that distort the results. Next, the measurement reliability of the capacitive imaging arrays is examined through in-vivo and in-vitro experiments as well as side-by-side comparative measurements with single sensor skin hydration probes. The advantages of the developed calibration method and image analysis tools are demonstrated via the introduction of new system applications in the skin research, including skin damage characterisation via occlusion, skin solvent penetration and water desorption in hair samples experiments. It has to be mentioned that a small number of subjects is used in these experiments and the results are compared with the literature, so the statistical significance is not clearly examined. Next, advanced image processing techniques are adapted and applied on the capacitive skin images to expand further the application of this technology. More specifically, the skin micro-relief aspects of interest in cosmetic industry are summarised, and algorithmic approaches for measuring the micro-relief orientation and intensity as well as the automatic skin grids account are reviewed and experimentally evaluated.

The main research aim and its objective have been achieved, with their methodologies clearly presented the their implementations evaluated with ex-

perimental results. However, vulnerabilities of this technology have also been exposed and suggestions for further improvement are provided in the conclusions.

Contents

List of Tables

List of Figures

Chapter 1

Introduction

The research aim of this work is to determine suitability and propose advantages of capacitive imaging arrays, while building upon the commercialised Epsilon E100 hydration imaging system by Biox Systems Ltd. [1]. This chapter serves two purposes, first, it familiarises the reader with the human skin and appendages anatomy in order to clarify the target measurand. Second, it presents various skin research instruments with different measurement apparatuses in order to identify how capacitive and resistive probes fit in the skin research market, and enable the clarification of the research aim and its objectives.

1.1 Anatomy of Human Skin and Appendages

The human skin, as represented in Figure 1.1, is separated into three main layers, the subcutis, the dermis and the epidermis. In a nutshell, the subcutis connects the skin to the underlying tissue, the dermis protects from external mechanical forces and the epidermis provides chemical and diffusion protection [2].

Subcutis

The subcutis or hypodermis serves two main functions, it stores fat to provide thermal insulation and protection from external forces, and it binds the rest of the skin layers with the underlying bones and muscles. It "consists of blood vessels, loose, areolar connective tissue and adipose tissue" [4].

Dermis

Dermis is the middle and thickest layer of the skin and it consists of two sublayers, the reticular and the papillary sublayer. The reticular is well circulated by blood, it is part of the autonomic nervous system since it contains sympathetic nerves, and it is responsible for keeping the overlying skin layers hydrated by binding water. Also,

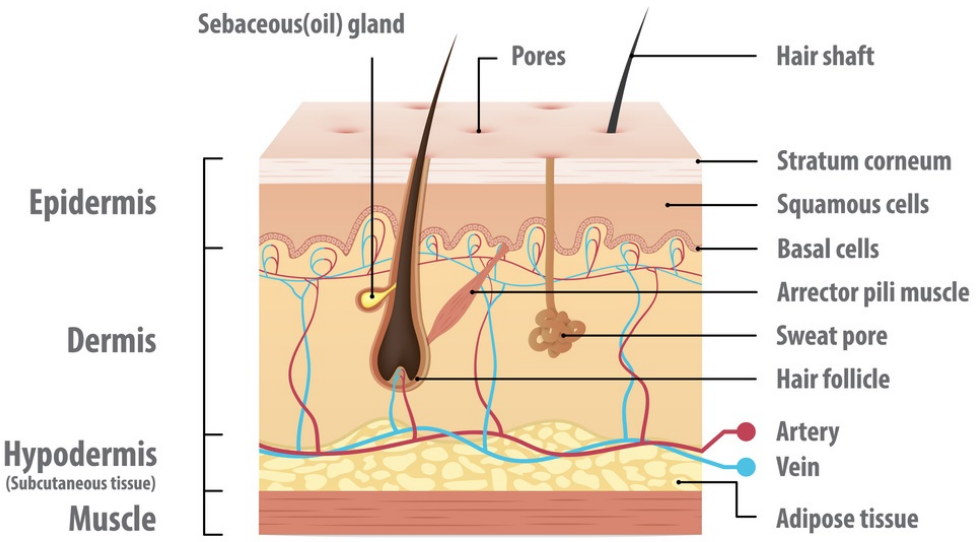

Figure 1.1. Human skin anatomy [3]. The figure demonstrates that the subcutis binds the skin with the underlying muscle and that it is well circulated with blood. The veins become narrower inside the dermis. At the same time the dermis contains the required mechanisms for hair growth and sweat activity control. Last, the epidermis, which mainly consists of keratinocytes and no blood vessels.

its elastic fibres buffer the skin strain during body movements [4]. The papillary sublayer is thinner than the reticular one, it contains the touch receptors as well as a small amount of fat cells and narrow blood vessels. An important function of this sublayer is the protection against bacteria that might have achieved to penetrate the epidermis [4].

Epidermis

The epidermis is the outer layer of the skin, it is mainly composed by keratinocytes, it has no blood vessels, and it is subdivided to four or five layers. The deepest layer of epidermis, the stratum basale, is the only layer that does not consist of keratinocytes. It has a single layer of basal cells that are responsible for providing keratinised cell through the process of mitosis to the overlying sublayers. The Basale layer also contains Merkel cells that provide touch and texture information to the brain [5], as well as the melanocytes that are responsible for the skin pigmentation [4]. Next, the stratum spinosum sublayer consists of eight to 10 layers of keratinocytes and Langerhans cells. The latter play an important role in skin infections, by processing "microbial antigens to become fully functional antigen-presenting cells" [6]. In the stratum granulosum that lies above, the cells become flatter while dying and leaving a residue of keratin and cell membrane. Above this, stratum lucidum can be found

only in sole and palm body sites and it consists of keratinocytes filled with eleidin proteins [7]. Last, the outermost sublayer of human skin, the stratum corneum, exhibits increased cell cornification and it is replaced on its entirely within a period of four to five weeks. It is the target of non-invasive skin research instruments since it plays crucial role in the prevention of microbes invasion and dehydration of the underlying tissue, i.e. the skin barrier.

Stratum Corneum

The thickness of the stratum corneum varies with the anatomic site, normally between $10{-}20\mu m$ [8]. Ya-Xian et al. [9] experimentally demonstrated this by counting the number of stratum corneum cell layers. They found the smallest count for genital skin site (6 ± 2) and the largest cell layers count for the heel site (86 ± 36). In the same work, they reported that there is no significant correlation between the thickness of the stratum corneum and the sex of the subject, but there is a thickness change over age for specific anatomic sites in male subjects. The cell layers of stratum corneum consist of corneocytes originating from the stratum granulosum layer, as summarised in the previous subsection. The corneocytes are held together by the corneodesmosomes, "the main intercellular adhesive structures in the stratum corneum" [10], that gradually degrade to allow worn-out corneocytes to be detached [11]. The degradation process is controlled by lipolytic and proteolytic enzymes [11]. The pathways between corneocytes are filled with free fatty acids, ceramides and cholesterol, which create the epidermal barrier and also have adhesive properties [11, 12].

Rawlings and Matts [13] summarize the three stratum corneum mechanisms that contribute to its holding of water abilities. The intercellular lamellar lipids that provide a tight and semi-permeable barrier, the corneodesmosome-bound and ceramide hydrophobed corneocytes and the intracellular and extracellular hygroscopic materials [13]. They also mention that the water content is less than 10% in the outermost layers of stratum corneum, information that will be useful when measuring its dielectric permittivity. A conversion between dielectric permittivity and water content is presented in Chapter 3. According to the literature [14], the hydration distribution in the stratum corneum is not uniform, with the outer and deeper layers swelling less during overhydration. While the corneocytes swell uniformly, in the intercellular space large and small pools of water which can exceed the size of corneocytes can be found [15].

Skin Texture

The skin, as presented in this chapter, is the largest organ of mammals in terms of surface area and weight and, at the same time, it is the most exposed organ to environmental influences [16]. Micro-topographic structures on the visible part of the skin provide information about dermis and body health as well as effects from environmental influences and living habits, such as extrinsic skin ageing due to UV light, alcohol or smoking [17]. These micro-topographic structures, so called skin micro-relief, are practically a grid of skin closed polygons that it is shaped between the primary and secondary skin lines [18]. Zahouani et al. [19] differentiates between these lines based on their depth, the primary lines covering Langer's lines are deeper than $60\mu m$ and intensify with age. The secondary lines are perpendicular to the first group, shallower than $60\mu m$ and fade with age [19]. According to the literature review by [20], this network contributes to the mechanical stretching ability of the skin as well as the evacuation and retention of sweat and sebum. Furthermore, the roughness of the skin texture is affected by the skin site, the age of the subject and the sun exposure [21, 22].

Skin Appendages

The visible part of hair (Figure 1.2a) is shaped as a three-layered shaft of dead protein filament: the cuticle, cortex and medulla [23]. The cuticle is a thin surrounding layer of roof tiles-like structures with about five degrees inclination from the hair shaft core. The cortex is the thickest layer of the hair, it consists of tightly packed keratin cells and it is responsible for the hair color as well as most of the water holding capabilities. Last, the medulla is a soft unstructured keratin that forms the core in the thicker human hair (e.g., scalp hair) [24]. Harkey [25] reports that the hair shaft thickness in men ranges from $15\mu m$ to $120\mu m$ depending on the anatomic site. In women, [26] measures the average diameter of white scalp hair at $67.68\mu m$ while this of pigmented scalp hair at $57.41\mu m$. While Buffoli et al. [27] states that the average diameter of scalp hair is between 60–$80\mu m$. Also, it is worthwhile to mention the results achieved by Otberg et al. [28], who measure the hair diameter for different anatomic site (Figure 1.3).

Various properties of scalp hair are studied by different scientific fields in order to extract information about the subject's health or the effect of cosmetic products. For example, Wosu et al. [29] found that stress psychiatric symptoms and disorders are more accurately detected by measuring cortisol concentrations from hair instead of blood, urine or saliva samples because the latter are affected by environmental influences and the subject's diet. Kristensen et al. [30] and Hamel et al. [31] confirmed that cortisol concentration in hair is not affected by every day activities (i.e.

dyeing, shampoo and frequent wash). Furthermore, in the field of cosmetic science Barba et al. [32] achieved to assess hair damage based on the sample's water holding capabilities using thermogravimetry while in the field of forensic science Boll et al. [33] managed to determine whether a hair sample is dyed and to identify the brand and colour using AT FT-IR.

The sagittal plane of the nail is illustrated in Figure 1.2b. The nail plate is a curved laminated keratinised structure that embeds its sides in the nail folds in order to enable using the exposed side as a tools, while at the same time it protects the underlying layer that allow it to regenerate [34]. This layer consists of two parts, the nail matrix and the nail bed. The nail matrix is responsible for creating most of the nail plate [34].

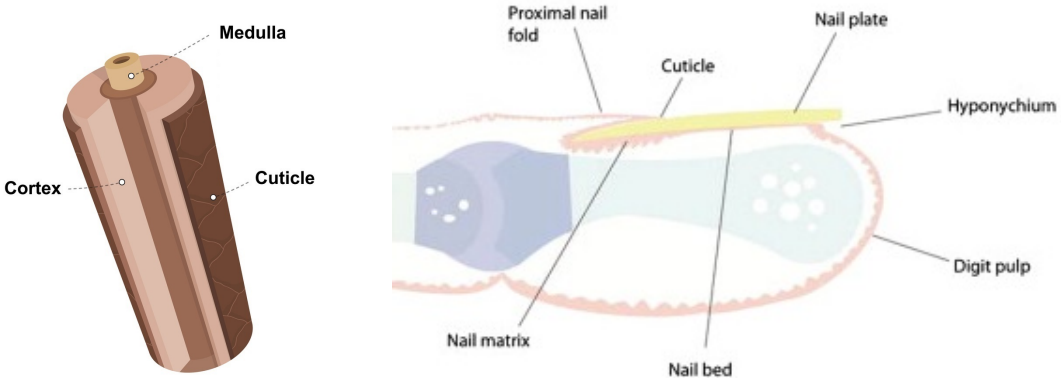

(a) (b)

Figure 1.2. (a) Human scalp hair anatomy [35], representing the three layers of the hair shaft. (b) Nail anatomy [34], demonstrating how the nail plate embeds in the proximal nail fold and how the nail matrix and bed are laying underneath it.

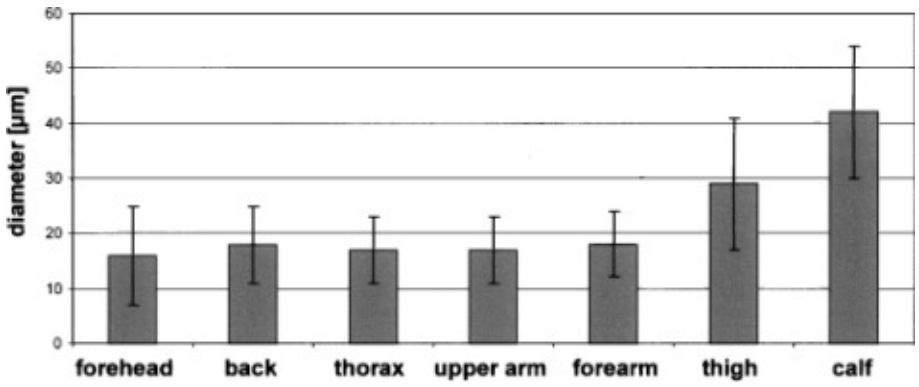

Figure 1.3. Hair measurements achieved by [28] demonstrate the hair shaft thickness variation for different anatomic sites.

1.2 Measurement Principles for Studying Skin

This section introduces a collection of measurement apparatuses for studying a variety of skin properties, not directly related to the capacitive imaging systems that will be the main focus of this work. Most of these technologies are well established and in many cases they outperform capacitive probes in measurement quality and information extraction from the measurand in skin research. This information should provide the minimum required background knowledge in order to identify the gap in skin research laboratory equipment market that capacitive imaging probes have the potential of covering.

Opto-Thermal Transient Emission Radiometry

OTTER, originally developed in the 1980s [36, 37], is a non-contact, non-invasive instrument that uses a modulated light source in order to increase the temperature of the sample surface and read back its blackbody radiation using a fast infrared detector [38]. As it is shown in Figure 1.4, a pulse laser beam is deflected on the sample bed using a mirror. The blackbody radiation from the sample surface temperature is focused on a mercury cadmium telluride detector via an interference filter using an off-axis ellipsoidal mirror. The MCT detector readouts depend on the optical and thermal properties of the sample surface, as well as its thickness and layered structure. By filtering for different detection wavelengths, OTTER can achieve hydration and solvent permeation measurements as well as depth profiling [38].

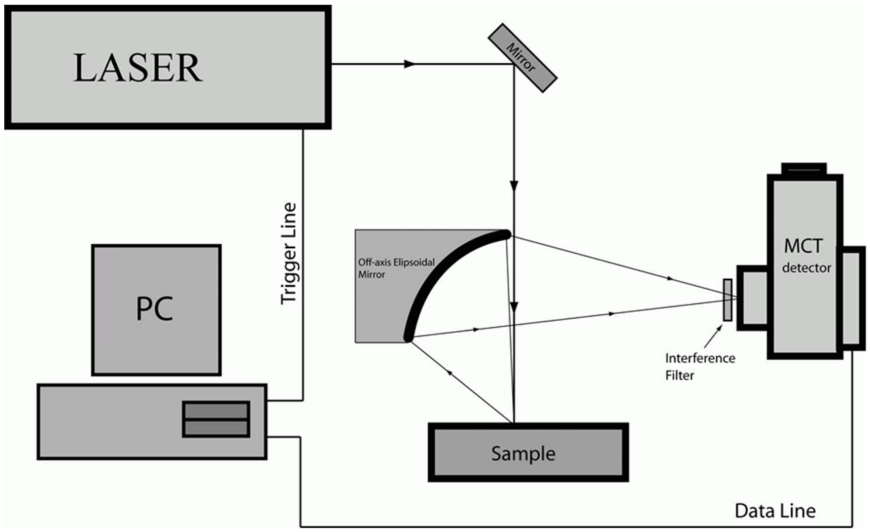

Figure 1.4. Conceptual diagram of OTTER measurement apparatus [38].

Confocal Raman Microspectroscopy

The Raman effect was discovered by Chandrasekhara Venkata Raman in 1928 [39], who was soon after awarded with the Nobel prize for his work [40]. When light hits on a material, a fraction of the light is scattered while the rest is absorbed. According to the Raman effect, a small portion of this scattered light has interacted with molecular vibrations that reduce its frequency and as a result its energy [41]. This energy drift is very characteristic to specific atoms and atom bonds [42], so the Raman spectrum conveys detailed information about the material's molecular composition [43]. Raman spectroscopy has been widely used in biologic studies, but its application on skin measurements was only enabled after the development of Confocal Raman Microscopy [44], which provided control over the measurement depth and volume [43].

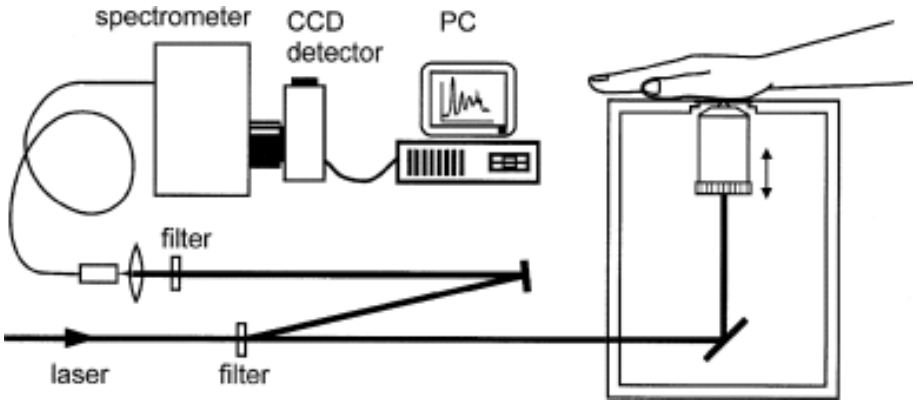

Figure 1.5. Conceptual diagram of Confocal Raman setup for skin measurements [43].

Electrical Hygrometry

This technology focuses on measuring the Transepidermal Water Loss (TEWL) in order to determine the state of the human skin barrier in vivo. An early application of this technology is demonstrated by Baker and Kligman [45], although biophysical instruments had not been a new invention at the time [46]. Prior to this, the skin TEWL was measured only ex-vivo, as described by Mali in [47]. The TEWL measurement technology has gone through multiple evolution stages and now there are four main variations available in the market: open chamber, closed chamber, ventilated closed chamber and condenser chamber [48]. The TEWL, in SI units, is practically the rate of water diffusion per skin surface area over time. To achieve this, the chambers are equipped with temperature and humidity sensors. Multiple advantages of using closed and especially condenser chamber approaches are presented in [49], but these are not of direct interest for this work.

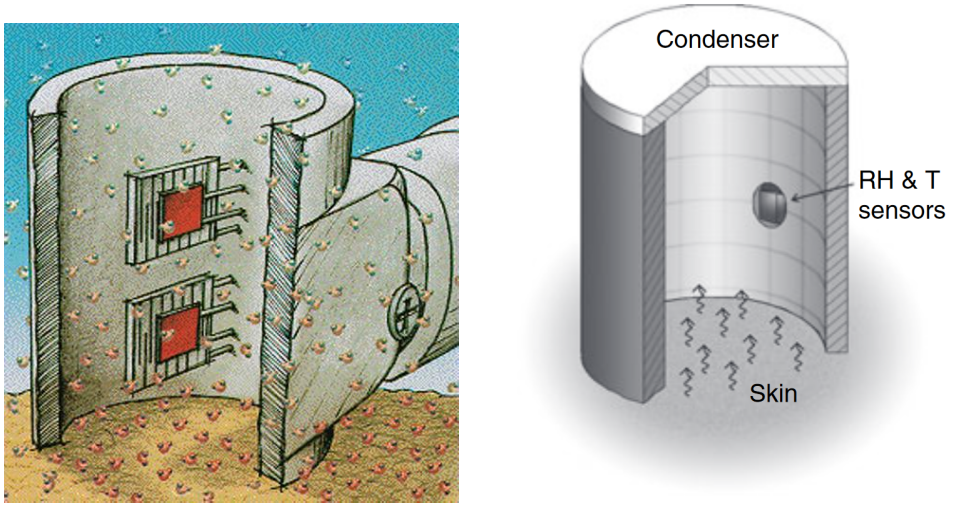

(a) (b)

Figure 1.6. Representation of (a) open chamber apparatus for Tewameter TM300 [50] and (b) condenser chamber for AquaFlux AF200 [49].

Dynamic Vapour Sorption

The DVS is a very accurate technique for measuring sorption of water vapours and organic solvents by a sample [51, 52]. As illustrated in Figure 1.7, the sample is placed on a high resolution gravimeter within a temperature and humidity controlled chamber. The micro-climate temperature is maintained constant during the experiment while the humidity changes with a pre-programmed stepping function every time the sample reaches thermodynamic equilibrium, i.e. the mass of the sample is stable [53]. The change in the mass of the sample in different humidity levels is equal to the water vapour or solvent that has been absorbed or desorbed by the sample. This information is very important in cosmetic and pharmaceutical research, because it determines the water holding capacity of keratinized tissues [23, 53]. The major drawback of this technology is that the measurement can only be in-vitro or ex-vivo.

Dermatoscopy

Dermatoscopy examines the skin surface using high resolution magnifying photographic equipment. Non-polarised dermatoscopes are used to study the superficial skin surface while polarised ones focus on deeper skin layers. Image processing techniques alongside pixel calibration and the use of external oblique light sources have enhanced applications and information extraction from this measurement apparatus in recent years. These include skin micro-relief analysis [54], colorimetry [55] and 3D visual reconstruction [56].

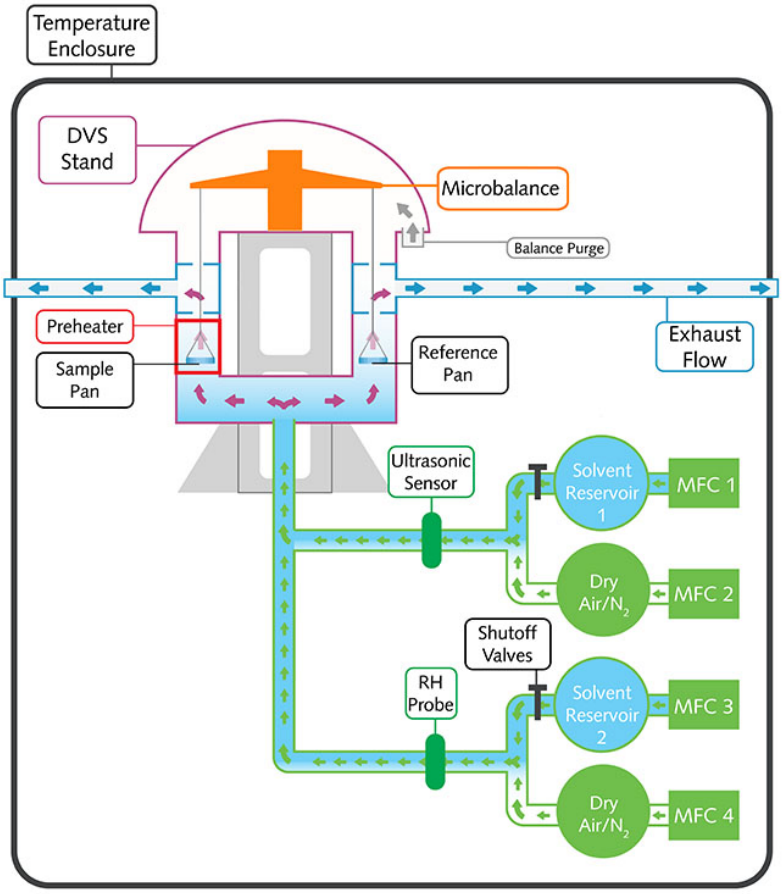

Figure 1.7. Conceptual diagram of Dynamic Vapour Sorption by Surface Measurement Systems Ltd. [52].

Non-invasive Electrical-based

The instruments in this category study the electric properties of the skin by placing the sample between two electrodes. A common capacitor structure (Figure 1.8a) would make in-vivo skin measurements impossible, so coplanar structures (Figure 1.8b) are employed in skin research to take advantage of the fringing field effect and study the samples in-vivo.

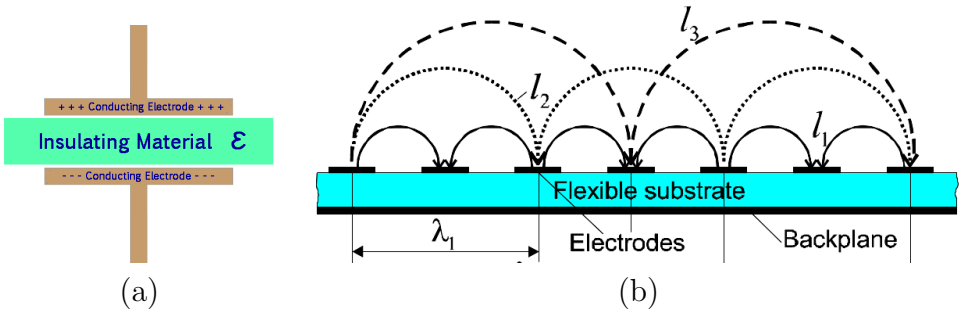

Figure 1.8. (a) The ideal parallel plate capacitor and (b) the coplanar electrode structure [57].

The readouts of such sensory system (Figure 1.8b), depend on a small portion of the electric field. Thus the sensor design becomes crucial. Table 1.1 outlines the sensor design aspects and how these affect the measurement sensitivity and penetration depth.

Table 1.1. Critical design aspects of coplanar capacitors [57] [58].

Design aspect	Description	Effect
Spatial wavelength	The distance between electrodes of the same type (λ_1 in Figure 1.8b).	Increasing spatial wavelength increases the penetration depth.
Electrode area	Width of electrodes	Increasing electrode area improves measurement sensitivity.
Guard electrodes	A group of grounded electrodes (i.e. shield electrodes and backplane)	Vary with design, see following rows.
Shield electrode	Grounded electrodes between driving and sensing electrodes	Shield electrodes increase penetration depth at cost of reduced signal strength.
Shield electrode width	-	Increasing width increases penetration depth and decreases signal strength.
Substrate thickness	(see Figure 1.8b).	Increasing the substrate thickness increases the signal strength and decreases the penetration depth.

Protective layer	A layer of dielectric material that protects the electrodes from direct contact with the sample. It stops galvanic contact and formulation of Debye layer.	Increasing its thickness decreases the penetration depth. Its dielectric permittivity, in comparison with this of the sample, can also affect the penetration depth.

Capacitance, Conductance and Skin Hydration

Capacitance and conductance describe material properties. The capacitance represents the amount of charge that can be stored in a material while the conductance represents the ease of current flow through a material. If a material is purely insulating by having infinite resistance (conductance $\sigma = 0$), its capacitance depends on its dielectric permittivity value (ε) and its volume. If a material is conducting, i.e. has finite resistance, then current flows and part of the electric energy is converted into heat. The human skin as a material has both of the above electric properties. This combination results to an electrical material property called impedance, a complex number Z where the modulus accounts for the resistance and the imaginary part accounts for the reactance of the material (Equation 1.1) [59]. Reactance depends on frequency and generally includes capacitance and inductance contributions. The latter is taken negligible in the present account.

$$\begin{gathered} \text{Electrical impedance } Z = \frac{V}{I} \\ \text{Resistance } |Z| = \mathrm{Re}\{Z\} = \frac{|V|}{|I|} \\ \text{Reactance } \angle Z = \mathrm{Im}\{Z\} = \angle V - \angle I \\ \text{where } V \text{ and } I \text{ the input voltage and current} \end{gathered} \tag{1.1}$$

The outermost layer of the skin, target of most non-invasive hydration instruments, consists of dead keratinocytes and it is expected to have low conductivity when it is properly acclimatised. This means that the capacitive part of the stratum corneum will dominate impedance measurements at lower frequencies [60]. Deeper skin layers are richer in water content with high conductivity, and so this will dominate the impedance readouts. Of course, the above mentioned are frequency dependent. Experimental and theoretical studies have shown that skin impedance readouts are dominated by stratum corneum capacitance at measurement frequencies below $10\mathrm{kHz}$ [61], while the latter is contributing 50% at $10\mathrm{kHz}$ [62] and only 10% at $100\mathrm{kHz}$ [63]. Figure 1.9 shows how the dielectric permittivity and resistivity of viable skin and stratum corneum change as a function of measurement frequency.

At this point, it is important to mention that the presented information applies only when the skin is properly acclimatised and that the effect of deeper skin layers is itself a function of stratum corneum thickness, so it is expected to vary between body sites. These have been experimentally proven by [64] in frequency ranges between 1MHz and 20GHz.

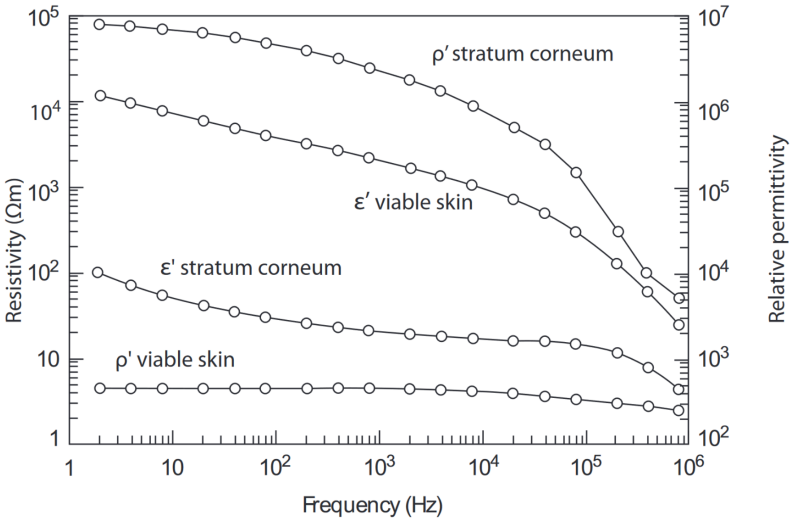

Figure 1.9. Resistivity (ρ') and dielectric permittivity (ε') values of stratum corneum and viable skin as a function of the applied signal frequency [65]. It is observed that the resistivity of the stratum corneum is high at lower frequencies, which means that it will not impact impedance measurements as much. In contrast, the resistivity of the viable skin is low at any frequency range, which means that it will have high impact in impedance measurements.

Having said that, criteria for the identification of non-invasive hydration sensor suitability in skin research are established to be the penetration depth of the electric field and the measurements frequency. Skin hydration instruments in the market target to measure either capacitance or conductance, with a few exception targeting impedance measurements, but either way the criteria remain the same.

1.3 Non-invasive Electrical-based Instruments for Skin Hydration

Corneometer CM825

The Corneometer is manufactured by Courage + Khazaka electronic GmbH [66], Köln Germany, and it is the most widely used instrument for measuring skin hydration over the last 30 years. According to the manufacturer's website, Corneometer CM825 measures skin moisture in 'corneometery' units (arbitrary), its penetration depth ranges within $10-20\mu m$, the measurements are triggered within one second

to avoid occlusion and the results are not affected by chemical substances, salts or residues of topically applied products. The measurement frequency is reported between $0.9 - 1.2\text{MHz}$ and the spring-loaded measurement head ensures constant pressure of $1.0\text{N} \pm 10\%$.

The sensing surface of Corneometer CM825 is $7\text{x}7\text{mm}$ and it is covered with a $20\mu\text{m}$ thick layer of glass. It uses an inter-digital electrode geometry, with $50\mu\text{m}$ electrode width and $75\mu\text{m}$ spacing between electrodes [67], which is equal to $250\mu\text{m}$ spatial wavelength.

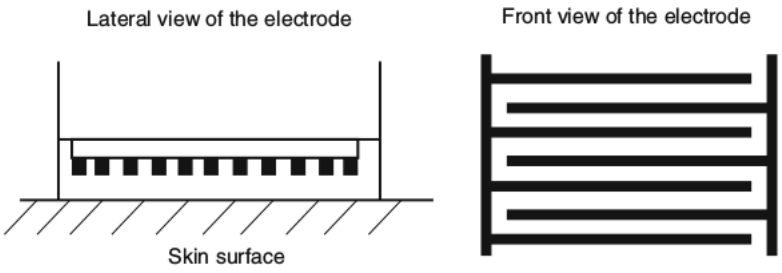

Figure 1.10. Representation of CM825 sensor [67].

Cortex

The hydration probe by Cortex Technology is sold as a skin research instrument for conductance measurements, which according to Cortex Technology website "is known to measure the water binding capacity of the stratum corneum" [68]. It is able to measure conductivity from $0\mu\text{S}$ to $9999\mu\text{S}$ with $1\mu\text{S}$ resolution at constant frequency and there are no claims as of its measurement depth. Two versions of this probe are available, one with flat and one with pin electrodes to cope with occlusion and to allow scalp measurements. In this work, only the probe with the flat electrodes is examined. Also, given the manufacturer refers to this probe as "the hydration probe" of DermaLab Combo, it will be referenced from now on as Cortex.

The sensor of the Cortex probe can be seen in Figure 1.11, it consists of tree concentric annular rings and it has no protective layer to avoid galvanic contact. Using a caliper, the sensors diameter was measured at 13mm while the inner and outer diameter of each ring are presented in Table 1.2.

Moisture-Checker

The MoistureChecker is manufactured by Scalar (Figure 1.12). It is a lower price instrument that it is claimed to be ideal for skin measurements, without specifying any scientific advantages. It presents the results in percentage of arbitrary units on an LCD screen. The spatial resolution of its interdigital sensor was measured at

Figure 1.11. Cortex flat hydration probe sensing surface [68]

Table 1.2. Measured Cortex electrodes' outer and inner diameters.

Electrode	Outer ⊘ mm	Inner ⊘ mm
Outer ground	12.7	8.6
Driving	7.8	3.9
Inner ground	3.1	0.75

850µm while the thickness of its electrodes are 250µm and the gap between them is 175µm. The sensing surface is covered by a thin coat to prevent galvanic contact with the sample but no information as of its thickness was found.

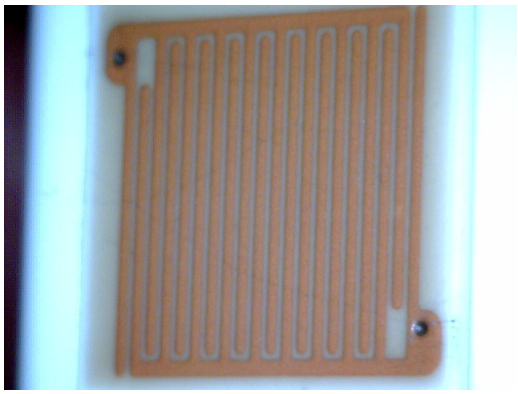

Figure 1.12. The MoistureChecker sensor.

Epsilon E100

The manufacturer of Epsilon E100 [69], Biox Systems Ltd., presents the instrument as a capacitive imaging system. They claim that it measures dielectric permittivity which ranges from 1 for air to 80 for water, it has linear and calibrated response, it provides readouts for the full scale without saturation (Figure 1.13b) and that its penetration depth is less than 5µm. That instrument provides numerical results as well as false colored dielectric permittivity images of the sensor surface. The overall measuring surface is 12.8×15mm and it is filled with an array of thousands of sensors, where each sensor/pixel scales 50µm (Figure 1.13a). A 2µm coat covers the electrodes, acting as a protective layer [70].

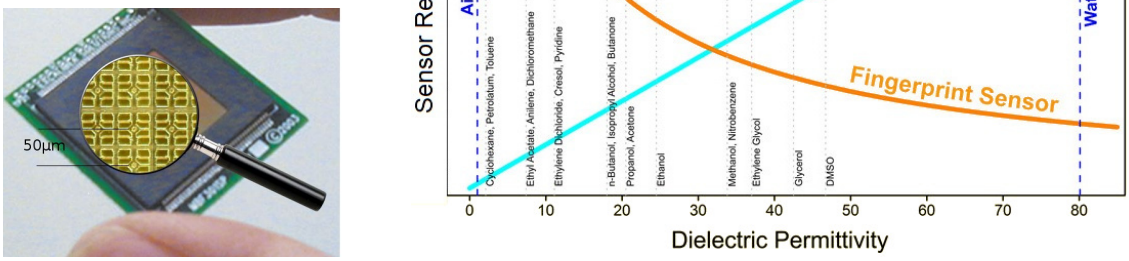

(a) (b)

Figure 1.13. (a) The Epsilon E100 sensor in magnification and (b) the sensor response before and after calibration to dielectric response [70].

1.4 Research Aim and Objectives of this Thesis

The literature review in skin research instruments reveals various measurement principles to examine different skin properties. The laser based instruments are capable of profiling hydration across multiple skin layers in vivo, but they are far from affordable and portable, and they examine only a small skin region at a time. The instruments that use hygrometric measurement principle are portable and could be found in affordable prices but they focus on measuring water diffusion. Similarly, DVS can measure water holding capability only in vitro or ex vivo, while dermatoscopes focus on visual inspection of the sample. Also, availability of electrical based hydration probes in the market is demonstrated, but their functionality is limited in providing a single numeric output, in some cases in arbitrary units. The research aim of this work is to provide solid evidence that capacitive imaging systems could find adequate applications as the above mentioned laboratory equipment while maintaining the portability and affordability of the electrical based skin hydration probes. In order to achieve this, the following research objectives are set.

The first objective towards this research aim is to assembly the physics background that clarifies the qualitative aspects of electrical-based measurement apparatuses in skin research. Based on the literature review on human skin, the criteria for the identification of non-invasive electrical based sensors suitability in skin hydration research are the penetration depth of the electric field and the measurement frequency (see Figure 1.9). Since the measurement depth should not be exceeding the thickness of the stratum corneum layer and the measurement frequency should be below 100kHz to reduce the effect of skin conductance in the case of capacitive measurements. Using this information, and by studying the electromechanical aspects of existing single sensor capacitive and resistive probes and simulating their

performance based on physical principles will indicate what to expect from this kind of equipment.

Second, the advantages of capacitive imaging arrays in skin research have to be investigated and further developed. Nowadays, this technology is mainly used for the visualisation of the skin hydration map in order to confirm absence of unwanted artifacts and successful acclimatisation of the target area before conducting a measurement with different laboratory equipment. This could change by introducing pixel array equalisation filters and pixel readouts calibration in SI units, i.e. dielectric permittivity. The performance of the suggested processes should be evaluated experimentally, under different environment conditions and by conducting in-vivo hydration experiments side-by-side with established laboratory equipment. Next, the capacitive imaging system applications have to be expanded by translating readouts to skin hydration levels, and by taking advantage of traditional image processing techniques and features of the measurement apparatus, such as occlusion and video recordings. These should demonstrate that the use of such technology is not restricted to skin visualisation and hydration measurements.

Finally, the image resolution limitations of capacitive imaging probes for skin research should be challenged via adaptation and application of advanced image processing algorithms. Apart from creating new system applications in skin research, this also targets to motivate and increase user confidence in challenging new data interpretation approaches.

Chapter 2

Electro-Mechanical Analysis of Capacitive and Conductive Systems in Skin Research

In this chapter, skin research instruments that use capacitive and resistive measurement principles are evaluated from an engineer's point of view. For examining the measurement depth of these instruments, electrostatic models are developed for different electrode geometries, and they are evaluated against different models and experimental results from the literature. The above, supported by an electromechanical analysis of the instruments and the published literature, enables the identification of the material properties that various skin hydration instruments in the market measure. Based on the findings, conclusions are drawn for the suitability of Epsilon E100 capacitive imaging sensor in skin research.

2.1 Coplanar Electrodes and Penetration Depth

In the skin research market, interdigital and annular electrode geometries are most commonly used. So, Maxwell-based electrostatic models as well as mathematical models from the literature for these geometries were studied. The interdigital geometry is probably preferred because such a printed circuit is cost efficient while it allows thin trails and minimum gap between them. Unfortunately, the accurate electrostatic modelling of this geometry is difficult because the electric potential on the electrode surface is mathematically undefined and the effect of sharp edges adds to the complexity. Chen Tianming [71] has experimentally proven that the models of interdigital geometries have higher error in comparison to other geometries. The annular ring geometry tends to appear in sensors with greater wavelength and requires vias on a multiplayer printed circuit board in order to minimize cross-talk between the driving and sensing tracks upon signal routing. In contrast to the interdigital electrodes, the mathematical models of annular disks are more simple and accurate.

Electrostatic-based Models

A property of electrostatics is that Maxwell's equations are linear, so an arbitrary distribution of charges can be expressed by the addition of the relevant contributions. This means that we can express the electric field and electrical potential as follows:

$$\overrightarrow{E} = \frac{\overrightarrow{F}}{q} = \sum_i k_e \frac{Q_i}{{r_i}^2} \hat{r}_i \tag{2.1}$$

and

$$\Phi = \sum_i k_e \frac{Q_i}{r_i} \tag{2.2}$$

where:

E = electric field
F = electrostatic force
q = Point positive charge
$k_e = 1/4\pi\varepsilon_0$
ε_0 = Dielectric permittivity of vacuum
Q = Charge
r = Distance from point charge
Φ = the electric potential

When a continuous distribution of charges exists, Equations 2.1 and 2.2 become integrals. In case of the interdigital electrode, when there is a uniform distribution of charges along the x-axis, one may substitute Q_i by σdx; where σ is the surface charge density. For the charge distribution residing on a strip (x_1, x_2), the electrical potential and the field intensity at an arbitrary point (x, y) is given by the expression in Equation 2.3. The expanded solution can be found in Appendix A.1.

$$\Phi(x, y) = \frac{\sigma}{4\pi\varepsilon_0}\left(\sinh^{-1}\frac{x_2 - x}{|y|} - \sinh^{-1}\frac{x_1 - x}{|y|}\right) \tag{2.3}$$

Equivalently, [72] calculates the electric potential at point perpendicular to the centre of a disk electrode as in Equation 2.4 and of an annulus as in Equation 2.5; where σ the surface charge density and R the radius.

$$\Phi(z) = \frac{\sigma}{2\varepsilon_0}\left[\sqrt{R^2 + z^2} - |z|\right] \tag{2.4}$$

$$\Phi(z) = \frac{\sigma}{2\varepsilon_0}\left[\sqrt{R_{outer}^2 + z^2} - \sqrt{R_{inner}^2 + z^2}\right] \tag{2.5}$$

Then, the electric potential at any given point can be calculate by the sum of the electric potential for all sensor electrodes (M) to that point, such as in Equation 2.6, using the corresponding geometry equation (Equation 2.3-2.5).

$$\Phi(x, y, z) = \sum_{m=1}^{M} \Phi_m(x, y, z) \tag{2.6}$$

Treating the sensor and the sample dielectric material as a closed system means that the total magnitude of positive and negative charges on the corresponding electrodes are equal (Equation 2.7), so the surface charge density of each electrode can be calculated by Equation 2.6 when the target point is defined on an electrode surface; where the electric potential is known. Equation 2.8 explains that, when the dielectric permittivity of the sample between the electrodes changes, either the surface charge density or the voltage has to change accordingly. Assuming that the surface charge density on each electrode is constant, the voltage level will drift to counter-balance the change in capacitance. Using this method, the penetration depth is defined as the perpendicular displacement from the sensor surface for which Equation 2.6 output drops by 97%, this threshold is called $\gamma 3\%$. Furthermore, calculating the total positive charge of the system, its capacitance can be calculated by Equation 2.8.

$$Q_+ + Q_- = 0 \implies \sum_{p=1}^{P} \sigma_p S_p = -\sum_{n=1}^{N} \sigma_n S_n \tag{2.7}$$

$$C = Q/V \tag{2.8}$$

Finally, the electric field can be obtained by Equation 2.9.

$$\begin{aligned} \vec{E} = -\nabla\Phi \implies \vec{E} &= -\left(\frac{\partial\Phi}{\partial x} + \frac{\partial\Phi}{\partial y}\right) \\ E_y &= -\frac{\partial\Phi}{\partial y} \\ E_x &= -\frac{\partial\Phi}{\partial x} \end{aligned} \tag{2.9}$$

The above logic was imported in Python for the solution of interdigital (Appendix A.2) and concentric rings (Appendix A.2) electrode geometries. These are utilised later in this chapter in order to evaluate the measurement depth of skin hydration instruments in the field. Also, it has to be mentioned that calculating the surface charge density using Equation 2.7 might be challenging in complicated systems, but the instruments which are studied in this work either exhibit geometrical symmetry or have small number of electrodes.

Model Evaluation in Measurement Depth Approximation

The Maxwell-based model for interdigital sensor geometries in Equation 2.3 was evaluated against the results reported by Hanno Hammer in [73], who set up assumptions for a simple Dirichlet problem and determined boundary condition of an interdigital sensor targeting to calculate elevating forces. He derived to an analytical model that calculates electric potential as in Equation 2.10. The comparative potential and electric field results (Figure 2.1b-d) were based on electrode geometry with $2\mu m$ electrode width, $2\mu m$ gap between the electrodes and for a line segment displaced by $0.1\mu m$ parallel to the middle driving electrode, ranging from and to the middle of the neighbouring electrode gaps (Figure 2.1a).

$$\Phi(x,y) = \sum_{k=0}^{\infty} \left[\frac{4\Phi_0}{\pi^2(2k+1)^2} \frac{w+d}{d} \cos\left[(2k+1)\frac{\pi}{2}\frac{w}{w+d}\right] \cos\left[(2k+1)\frac{\pi x}{w+d}\right] \exp\left[-(2k+1)\frac{\pi y}{w+d}\right] \right] \tag{2.10}$$

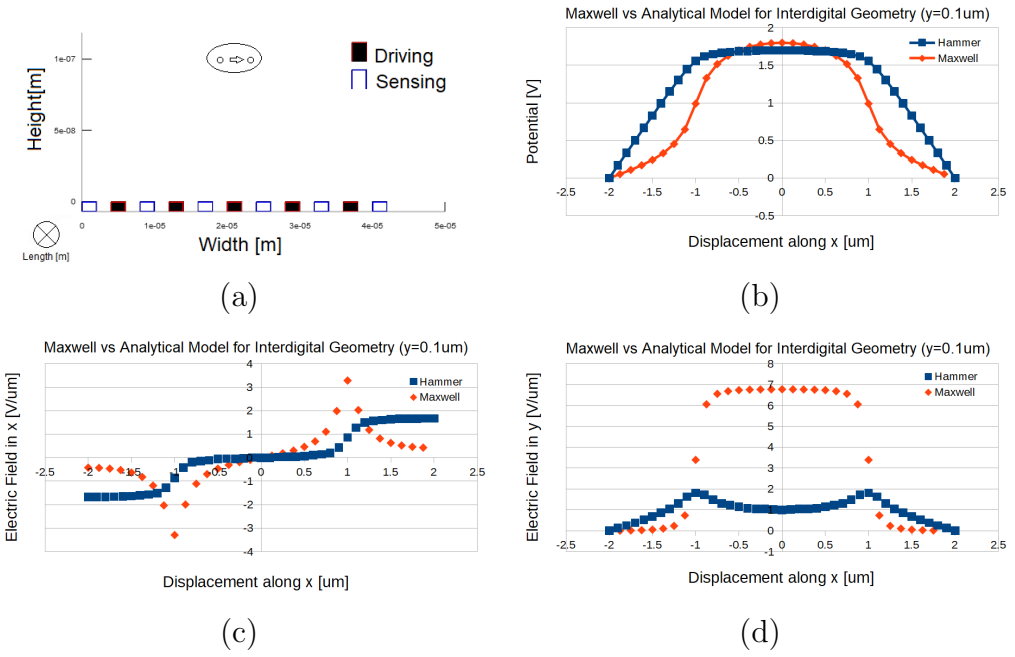

(a) (b) (c) (d)

Figure 2.1. Comparison of electric field and potential energy for interdigital electrode geometry along a line segment perpendicular to the electrodes' length between the analytic model by [73] in Appendix A.3 and the electrostatic model in Appendix A.2. (a) The representation of the electrodes and the line segment, (b) the calculated potential energy, (c) the electric field along x and (d) the electric field along y axis.

The above results first confirm that the analytic model by [73] was imported correctly in Octave [74], since they match with the published ones. Then, it was observed that the potential energy along x-axis for a constant height y correlates

well between the two models. In contrast, there is a significant error in the comparison of the electric field calculations, which probably derives from the fact that the Maxwell-based model does not account for the height of the electrodes while [73] does. Having a performance reference for these models as well as the freedom to extract different model aspects, enabled the modification of the line segment position and orientation in order to study the measurement depth of the electric field. For this purpose, the beginning of the line segment was set on the surface of the middle driving electrode and it was extending perpendicular to the sensor surface for $20\mu m$ (Figure 2.2a). The penetration depth of the electric field was defined at the point which the potential energy reaches the $\gamma 3\%$ threshold of its maximum value ($1.8V$). The comparative results in Figure 2.2b show a large error between the two models, thus the electrostatic model will have to be compared against experimental results to confirm its accuracy (i.e. confirm that there is no mistake in the algorithm implementation).

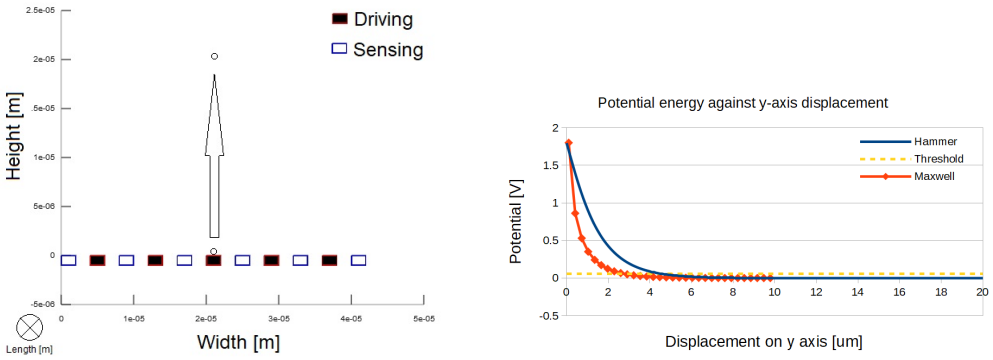

(a) (b)

Figure 2.2. Comparison of measurement depth estimation between the electrostatic and the analytic model by [73]. The results show a large measurement depth error between the two models, thus the electrostatic model will have to be compared against experimental results to confirm its accuracy.

Clarys P. et al [75] and Fluhr et al. [76] have experimentally measured the measurement depth of Corneometer CM825 by placing varying number of polyurethane plastic foil sheets ($15\mu m$ thickness each) between the sensing surface and a C-K calibration filter pad saturated with ultrapure destilled water. The dielectric permittivity of polyurethane film at 1kHz measurement frequency is expected to be 4.09 [77]. Based on this information the electrostatic measurement depth simulation is executed and the result is compared against the experimental results achieved by [75, 76] in Figure 2.3. Note, that the y axis displacement is at $20\mu m$ representing the end of the glass protective layer. Also, the output of the simulation has been fitted, at $20\mu m$ displacement, to 'corneometer units' for direct comparison. The results confirms that the electrostatic simulation is more accurate than the Dirichlet solution approach presented in Figure 2.2 for the measurement depth estimation.

There is still an error, in the opposite direction of the Dirichlet solution approach, and the experimental results between the two publications do not firmly agree. Since Clarys P. et al [75] detect output variation for up to two sheets of plastic foil, while Fluhr et al. [76] report no output variation after one plastic foil sheet. So, the reader should be aware that the provided electrostatic model might be over-estimating the measurement depth, since ideal conditions are assumed.

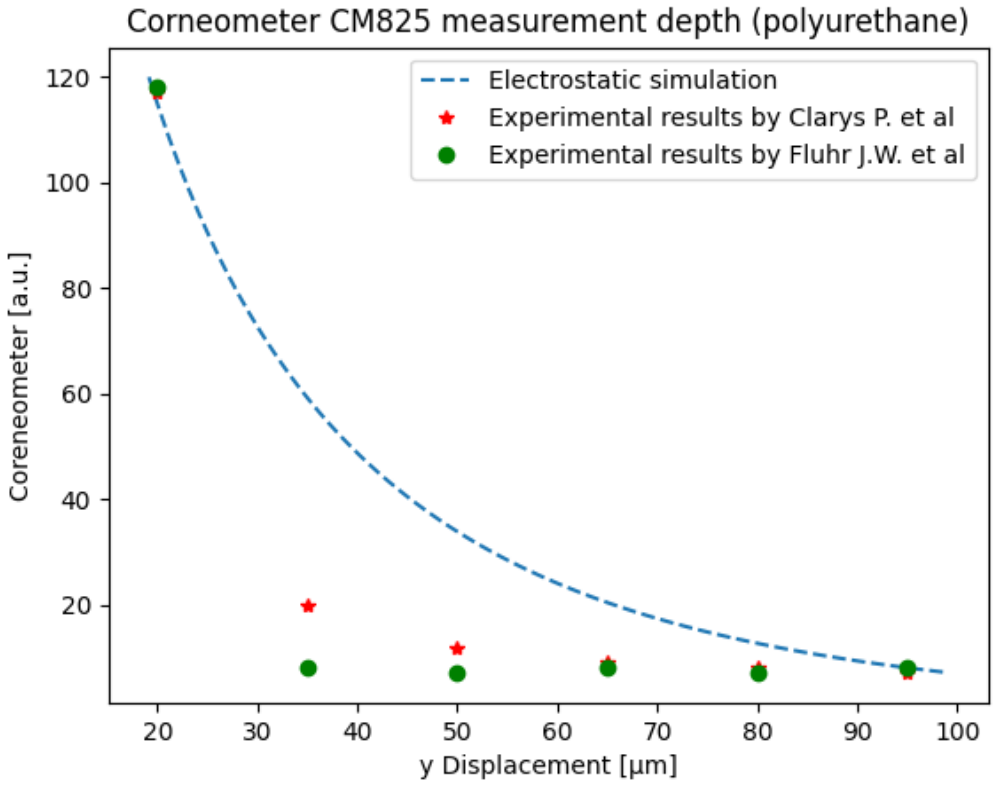

Figure 2.3. Corneometer CM825 measurement depth comparative results between the electrostatic model and experimental measurements reported by Clarys et al [75] and Fluhr et al. [76] using polyurethane films of 15μm thickness each. Note that the y axis is displaced by 20μm, the thickness of the protective layer.

2.2 Electro-mechanical Assessment of Skin Hydration Probes

The skin hydration probes in the market can be categorised based on their price, the material property they measure, the number and size of their electrodes and the thickness of their protective layer. The market price is not a direct criterion of the measurement quality, but it might be implying the target audience. The protective layer is an important factor because it affects the penetration depth of the electric field into the tissue and the measurement sensitivity. Last, the number

of sensing elements can improve the reliability and expand the applications of the instrument using advanced signal and imaging processing algorithms (Chapter 3-4) but technology miniaturisation makes the system more vulnerable to electromagnetic noise or physical damage. Based on these characteristics, the following instruments were selected for further investigation as the most representative in the market:

1. The Corneometer CM825 [66] by Courage + Khazaka electronic GmbH (Cologne, Germany), the most commonly used single-sensor skin hydration probe over the last 25 years.

2. The hydration probe of DermaLab [68] by Cortex Technology (Hadsund, Denmark), representative of high end single-sensor probes without protective layer.

3. The MoistureChecker MY-808S [78] by Scalar (Tokyo, Japan), representative of low cost single-sensor probes.

4. The Epsilon E100 [1] by Biox Systems Ltd. (London, UK), an advanced capacitive imaging system for skin hydration measurements.

Corneometer CM825

One of the manufacturer claims is that the sampling frequency of CM825 is between $0.9 - 1.2\text{MHz}$. The sensor surface has one exposed pad for each electrode on the sensor measurement head, so by connecting the oscilloscope between these pads frequency variations were detected when the sensor was in contact with different materials. Figure 2.4 shows the sensor response for air and water samples where frequency varies from 1.1 to 0.9MHz correspondingly, confirming the claim of the manufacturer. Based on the analysis by [65] in Figure 1.9, if the electric field of the Corneometer reaches viable tissues this will dominate the results at sampling frequencies between 0.9 and 1.1MHz. If the electric field does not reach viable tissue the measurements will be heavily influenced by the high conductance of stratum corneum in such high frequencies.

The manufacturer claims that the measurement depth is between $10 - 20\mu\text{m}$, ideal for skin hydration measurements. Experimental results by [75] and [76] find the measurement depth of Corneometer CM825 $50 - 65\mu\text{m}$ and $35 - 50\mu\text{m}$ correspondingly, by adding $15\mu\text{m}$ thin plastic foil sheets between the sensing surface and the sample and measuring the drift in the readouts. These plastic foil sheets have lower dielectric permittivity than the skin, so it is expected to be over-estimating the measurement depth. According to [67], polyurethane film were used with expected dielectric permittivity of 4.09 [77], while the dielectric permittivity of the stratum corneum is expected to be closer to 7 [13, 79]. In this work, in order to evaluate

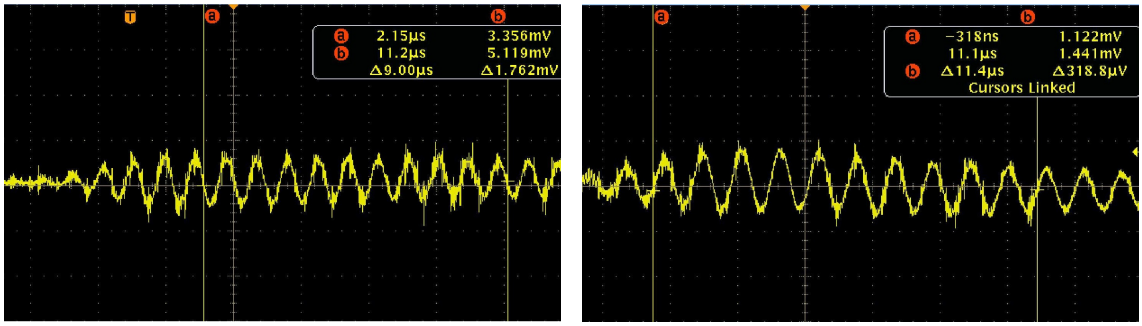

(a) (b)

Figure 2.4. Corneometer CM825 electrodes' response measured with the oscilloscope when the sensor is brought in contact with (a) air and (b) water. In each case, ten charge/discharge cycles are captured and the time elapsed is used in order to calculate the average sampling frequency. For the air sample (a), we note that the time elapsed for ten periods is 9µs, which means that the average sampling period is 0.9µs or 1.1MHz. For the water sample (b), we note that the time elapsed for ten periods is 11.4µs, which means that the average sampling period is 1.14µs or 0.9MHz. The Tektronix TDS2012 oscilloscope model was used, configured at 500MS/s, 2µs per time division and 20mV per voltage division.

the measurement depth of Coreneometer CM825 the information on the sensor geometric characteristics was used in combination with Equation 2.3. The simulation, which defined six sensing and five driving rectangular electrode rows, calculated the electric potential on a line segment from the centre and perpendicular to the sensing surface for 60µm displacement. The simulation was repeated for representative dielectric permittivity value samples without taking into account the 20µm protective layer. The results in Figure 2.5 show that the manufacturer's claim on the measurement depth will only be valid for samples with dielectric permittivity below 4, and not for the normal stratum corneum hydration measurements. For samples with dielectric permittivity 7, more representative of the skin surface [13, 79], the measurement depth will be below 2µm. This ensures that no viable tissue will be reached, but at the same time it risks superficial skin measurements and reduced sensitivity.

The manufacturer of Corneometer CM825 also claims that the readouts are not affected by chemical substances, salts or residues of topically applied products. Evidence against this claim might lie with the user calibration process kit available by the manufacturer. Clarys et al. [75], while conducting side-by-side in-vivo and in-vitro measurements between Corneometer CM825 and Skicon (conductance meter), reported that the calibration solution of CM825 has high conductance, i.e. 3026µS when ordinary distilled water has conductivity of 796µS. Also, the presented in-vitro results in the same publication show a clear effect of conductance in Corneometer CM825 readouts, with measurement overshoots when the solution is conductive (see 1-Butanol, 1-Propanol, Ethanol, Methanol and Ethanol 50% in Figure 2.6). Accord-

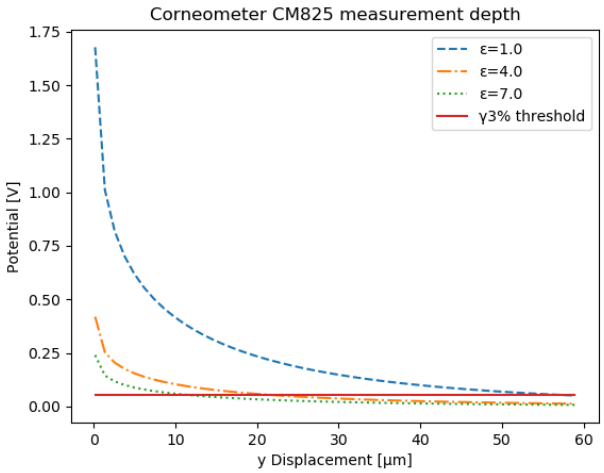

Figure 2.5. Simulation results on examination of Corneometer CM825 electric field penetration depth, without accounting for the protective layer.

ing to Equation 1.1, the readouts of a capacitive measurement apparatus, such as Corneometer CM825 and Epsilon E100, are bounded to be affected by the conductance of the sample. An impedance measurement method should be used in order to differentiate between the sample's capacitance and conductance.

TABLE 2. Capacitance and conductance measurements on C-K calibration filter pads saturated with liquids of different dielectric constants. Mean value and SD of 20 measurements

Solvent	Dielectric constant	Corneometer (a.u.)	Skicon (μS)
Mineral oil	2–3	11 ± 2	0
2-Ethyl-1-hexanol	10.3	20*	–
Cyclohexanol	15.0	33.1± 0.5	8
1-Butanol	17.8	58 ± 3	31 ± 2
2-Propanol	18.9	41*	–
1-Propanol	21.8	63 ± 6	69 ± 4
Ethanol	24.9	76 ± 6	133 ± 8
Ethanol 90%	30.4	60*	–
Methanol	32.6	85 ± 3	235 ± 32
Ethanol 50%	52.5	99 ± 5	420 ± 50
Ethanol 50%	52.5	83*	–
Ethanol 66%	61.7	102 ± 5	–
Water	80.2	118 ± 2	600 ± 98
Correlation *r* (*P*)		0.922 ($P < 0.01$)	0.989 ($P < 0.01$)

Figure 2.6. In-vitro CM825 and Skicon probes side by side experimental results as presented by [75].

Using again the Tektronix TDS2012 oscilloscope model, a square waveform was detected with period proportional to the displayed numeric readouts on the cable that connects the probe with the base unit. It can be assumed that the base unit converts the pulse signal frequency to 'corneometery' units based on some sort of calibration algorithm before displaying them to the user. The simplicity of the in-

terface between the probe and the base unit might imply that a timer, such as the LM555, or a custom-designed impedance analysis Integrated Circuit (IC), is used to calculate the capacitance of the sample. A mainstream impedance analysis IC would be expected to have at least one embedded serial bus for configuration and possibly more complex signal output interface in order to differentiate between dielectric permittivity and dielectric loss. The use of timer IC component for measuring capacitance is not an uncommon or inaccurate practice, e.g. Xiang Gao et al. [80] have recently used it in combination with a fringing sensor to prototype their suggested design that protects against unlawful component removal from circuit boards. The mechanical aspects of Corneometer's manufacturer claims are confirmed, but not the measurement depth and immunity to conductance.

Cortex

Maybe the strongest claim made by the manufacturer about the Cortex hydration probe, is the constant sampling frequency at 100kHz. This is important because, as it was shown in Chapter 1, 90% of the readouts will be affected by the stratum corneum conductance at this frequency [63]. In order to confirm the claim, an oscilloscope probe was placed between the ground and the output signal (see Figure 2.7a), which informed that the measurement frequency is constant at 100kHz and that the peak voltage output is directly proportional to the instrument's readout values. This implies that a circuit similar to Figure 2.7a might be used alongside high resolution analogue to digital converters and noise reduction techniques. In order to investigate the conductance measurements accuracy, resistors with known name values and margins were placed between the driving and the sensing electrodes of the sensor (Z_s). The results of this experiments in Figure 2.7b confirmed the manufacturer's claim on conductive measurements resolution.

Next, the instrument's penetration depth was examined using the electrostatic-based simulation (Appendix A.2). That simulation defined one driving and two sensing concentric annular electrodes with the geometrical characteristics reported in Table 1.2. The electric potential was calculated on a line segment from the centre of the sensor (above sensing electrode) and perpendicular to the sensor surface. The results are presented in Figure 2.8 for representative dielectric permittivity samples. The measurement depth was found to be in range of millimeters, and unsuitable for stratum corneum hydration measurements. Nevertheless, this does not contradict the manufacturer's claims since it was found to have constant sampling frequency and measuring conductance with 1μS resolution.

While the instrument measures conductance very accurately based on a voltage divider circuit, the readouts will cease to be linear once Z_s becomes a complex component, such as the human skin. Assuming parallel RC circuit for modelling

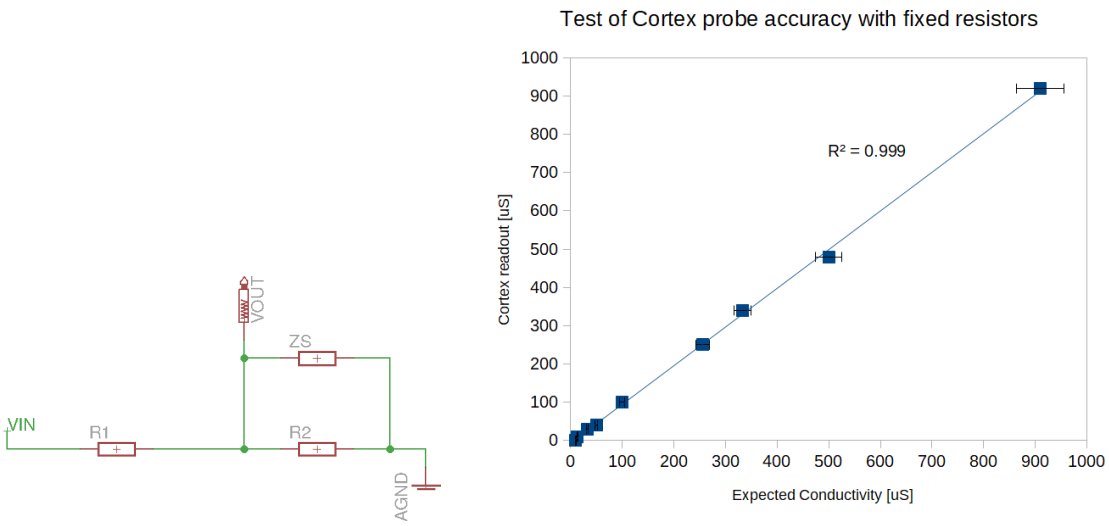

(a) (b)

Figure 2.7. (a) A hypothetical core measurement circuit for a conductivity meter, where R1 and R2 voltage divider with fixed resistors and Z_s the complex resistance of the sample that is brought in contact with the sensors surface. (b) Experimental measurements to determine Cortex probe accuracy using biased external resistors. The Cortex probe readouts are within the expected conductance, taking into account the external tolerance of 5%. The high correlation between readouts and expected results confirms the claims of the manufacturer.

stratum corneum ($Z_s = Z_{Rs}||Z_{Cs}$), when conductance is low, the capacitive part of Z_s will affect linearity because of incomplete capacitor charge/discharge cycles (sampling frequency dependent). In order to quantify what 'low' conductance means and whether it can affect the instrument's readouts in skin measurements, the system capacitance has to be calculated. Based on Equation 2.7, the surface charge density relation between the driving electrode with surface area S_2 and the sensing electrodes with surface area S_1 and S_3 can be expressed as follows:

$$\sigma_+ S_2 = \sigma_- S_1 + \sigma_- S_3 \implies \sigma_+ = \frac{\sigma_-(S_1 + S_3)}{S_2} \tag{2.11}$$

where:

σ = surface charge density
S = electrode surface area

Then, knowing that at the centre of the sensor (x=y=z=0) the sensing electrode has electrical potential of $-V_{IN_{peak}}$ from the oscilloscope measurements, the solution of Equation 2.6 can provide the charge density on the sensing electrodes:

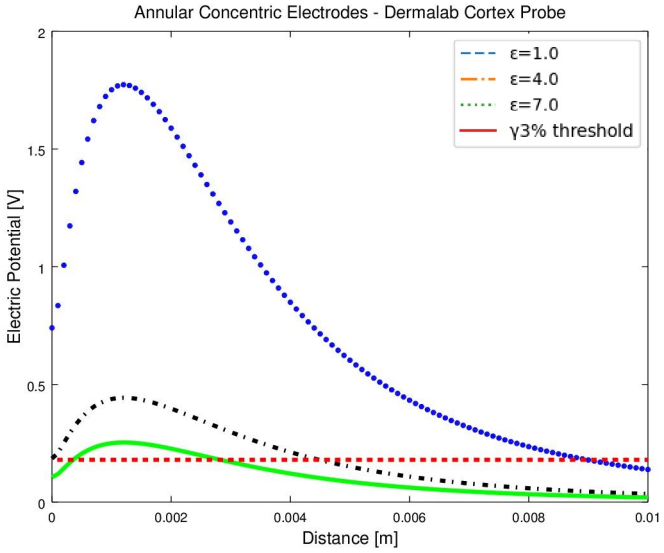

Figure 2.8. Electric potential in respect to distance from the electrodes and $\gamma 3\%$ penetration depth threshold for the Cortex.

$$\Phi(0,0,0) = \frac{\sigma_+}{2\varepsilon_0}(R_{2out} - R_{2in}) - \frac{\sigma_-}{2\varepsilon_0}(R_{1out} - R_{1in}) - \frac{\sigma_-}{2\varepsilon_0}(R_{3out} - R_{3in}) \implies$$
$$\sigma_- = \frac{\Phi(0,0,0)}{\frac{(S_1+S_3)(R_{2out}-R_{2in})}{2\varepsilon_0 S_2} - \frac{R_{1out}-R_{1in}}{2\varepsilon_0} - \frac{R_{3out}-R_{3in}}{2\varepsilon_0}} \tag{2.12}$$

where R_{xout}, R_{xin} the outer and inner electrode radius in meters.

Replacing the constants of the Cortex probe mechanical and electrical characteristics (Appendix A.5), the surface charge density on the sensing electrodes was found at $-1.28e-8[Cm^{-2}]$ while on the positive electrode at $2.72e-8[Cm^{-2}]$. The closed system positive charge is then calculated by $\sigma_+ S_2$ at $3.89e-12[C]$ and the minimum system capacitance in vacuum by Equation 2.8 at $5.0695e-12[F]$. The same problem was solved using the dielectric permittivity of pure water at 20^oC to define that the maximum possible system capacitance is $2.4e-10[F]$.

Now, Equation 2.13 can be solved for various combinations of conductive and capacitive Z_s components within the calculated minimum and maximum ranges in order to determine whether the Cortex might have linear scale when measuring actual human skin. To increase linearity $Z_1 << Z_2$ was assumed, i.e. $Z_1 = 0.1KOhm$ and $Z_2 = 100MOhm$.

$$V_{OUTpeak} = V_{INpeak} - \frac{V_{INpeak} Z_1}{Z_1 + Z_s || Z_2} \tag{2.13}$$

The result of this simulation, as they were produced by the Octave script in Appendix A.4, are presented in Figure 2.9. These confirm that while capacitance increases and conductance decreases the instrument's output ceases to be linear. More

specifically, the system stops being linear when the conductance is below $3e-4[S]$ or above $3.3[kOhm]$. In the beginning of this chapter, Figure 1.9 shows that stratum corneum resistivity at 100KHz is about $1[kOhm]$ while this of viable tissue is less. Based on this information, and keeping in mind that the used circuit in this simulation was purely based on speculations, the instrument should actually have linear conductive response when measuring human skin samples.

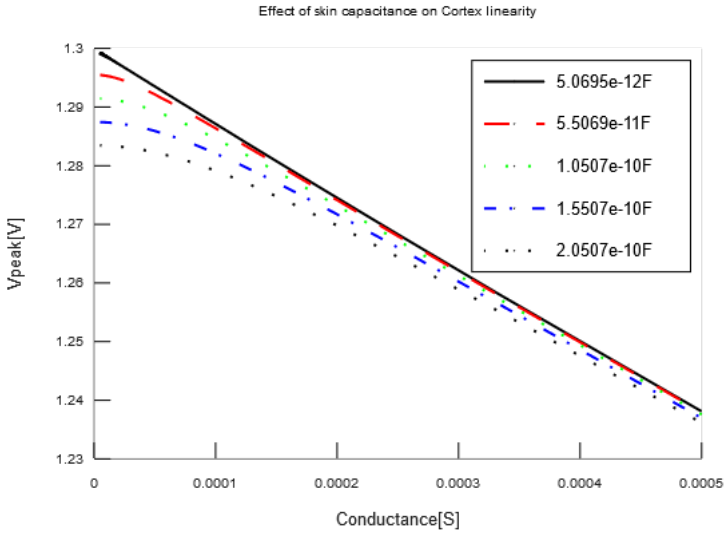

Figure 2.9. Simulation results of Cortex measurement principle circuit in order to examine linearity of its conductivity scale when measuring actual skin samples.

Moisture-Checker

While the manufacturer of MoistureChecker makes no claims about the sampling frequency, this will be measured again to compare with previous instruments. The Tektronix TDS2012 oscilloscope probe was connected at the vias of each electrode, as they can be seen in top left and bottom right corners of Figure 1.12, and variable sampling frequency was detected. Measurements on different body sites and material triggered different sampling frequencies ranging from 48kHz for water to 751kHz for volar forearm (Table 2.1). This implies a biased error in impedance measurements. Next, the penetration depth of the sensor was examined using again the electrostatic-based simulation (Appendix A.2). The depth was calculated at $36\mu m$ for a sample with dielectric permittivity 7 while it reached $70\mu m$ for dielectric permittivity 4 (Figure 2.10). This means that, if the protective layer is between $20-30\mu m$ and the sample skin hydration is above 10%, the readouts will not be affected by deeper skin layers. Due to the high sampling frequency variations, the instrument was not be investigated further.

Table 2.1. MoistureChecker sampling frequency as measured between the electrodes and when the sensor was brought in contact with different body sites.

Sample	**Frequency [kHz]**
No Sample	106
Thumb	694
Palm	714
Volar Forearm	751
Face	683
Nail	118
Hair	113
Water	48

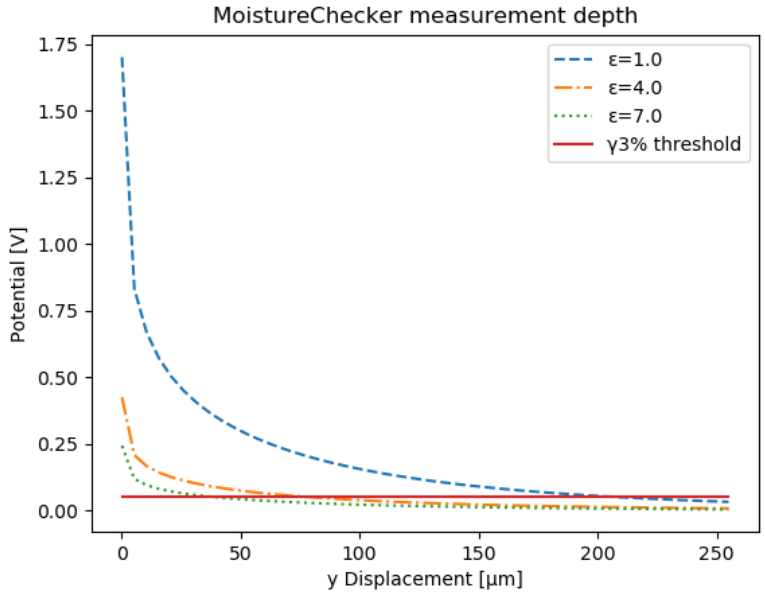

Figure 2.10. Electric potential in respect to distance from the electrodes and $\gamma 3\%$ penetration depth threshold for the MoistureChecker.

Epsilon E100

The sensing surface of the Epsilon E100 is embedded in an integrated circuit and the signals involved in the capacitive measurements are not exposed for direct analysis. The integrated circuit outputs the greyscale data directly in digital format via an internal USB bus, which is parsed by a general purpose computer alongside the calibration of the instrument that lives in an internal storage device. The sensing integrated circuit is a fingerprint sensor, so it is assumed that there is no sampling frequency but the pixels are taken through a single charge-discharged cycle to calculate the capacitance of the sample. Given there is no evidence with regards to

the actual measurement principle, the manufacturer's claim about the linear dielectric response was examined via solvent measurements. More specifically, insulating material with known dielectric permittivity value were placed on the sensor surface and the instrument's readouts were plotted against the expected values. The results in Figure 2.11 indicate that the sensor does not actually have linear dielectric response. This can also be concluded from experimental results achieved by [81] where Epsilon E100 shows good in-vitro correlation ($R = 0.97$) with Corneometer CM825, which has no linear response to dielectric permittivity. This error is investigated further in Chapter 3.

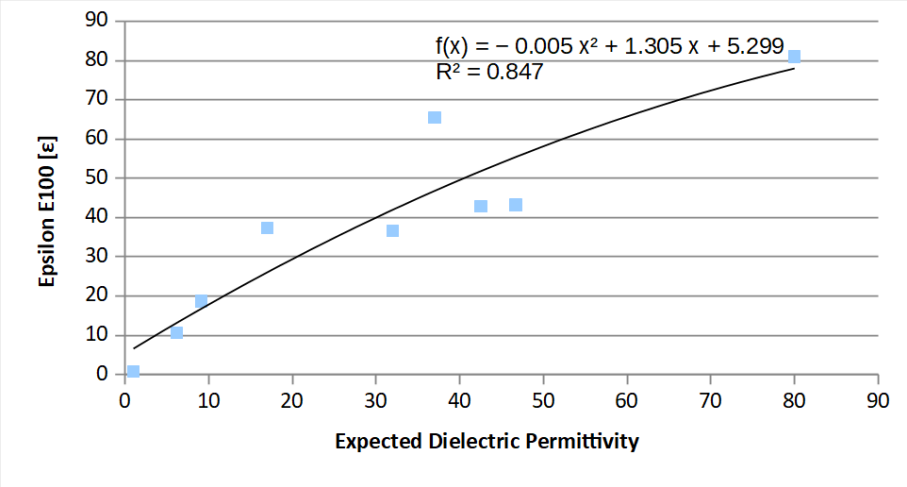

Figure 2.11. Correlation between Epsilon E100 readouts and solvent name value dielectric permittivity. The used insulating material and their expected dielectric permittivity are: Decanal(6.2), Heptanol (9.1), Butanol (17.8), PG (32), Ethylene Glycol (37), Glycerol (42.5), DMSO (47.2), Water (80.1) and air (1.0)

In order to investigate the measurement depth of Epsilon E100, the electrostatic model for annular electrodes (Appendix A.2) was used. Without taking into account the $2.0\mu m$ protective layer, the total penetration depth was calculated $29.5\mu m$ in vacuum, $13.2\mu m$ in silicon dioxide and $8.6\mu m$ when the sample has dielectric permittivity 7 (Figure 2.12). This means that the instrument has very good penetration depth for skin measurements and it is not expected to exceed $20\mu m$ even when the skin is dehydrated.

2.3 Summary

In this chapter, electrostatic models for estimating the measurement depth of electrical-based skin hydration probes were developed and evaluated against different models as well as against experimental results from the literature. This alongside the information about the resistance and capacitance of stratum corneum and viable tissue as functions of measurement frequency, were used as criteria to determine the suitabil-

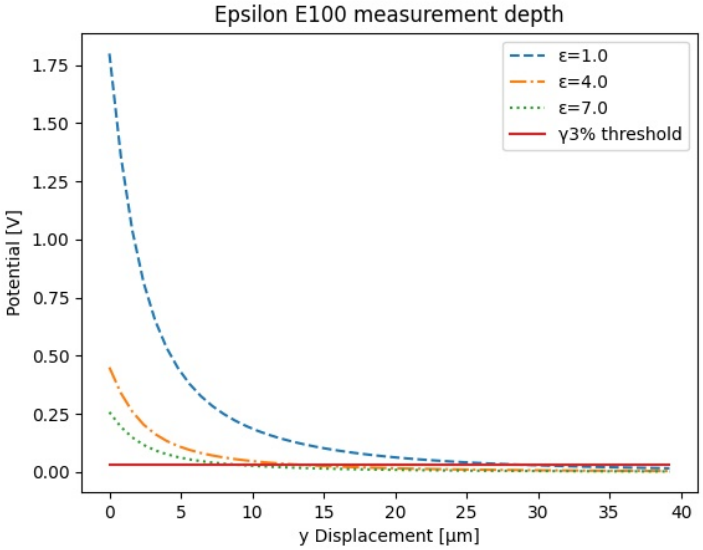

Figure 2.12. Electric potential in respect to distance from the electrodes and $\gamma 3\%$ penetration depth threshold for the Epsilon E100.

ity of electrical based hydration probes in the skin research market. More specifically, it was determined that an ideal skin hydration instrument should be using constant measurement frequency below 100kHz and that its electric field penetration depth should not be reaching viable tissue. The pre-stated information enabled the investigation of existing skin hydration instruments in the market (Table 2.2) in order to manifest the expectations of the scientific community and to examine the suitability of Epsilon E100 in such applications.

Instrument	Principle	Electrode geometry	Protective layer	Measurement depth [μm]	Frequency [MHz]
Corneometer CM825	Capacitive	I	Glass 20μm	< 2	0.9-1.1
Cortex	Conductive	A	None	> 4500	0.1
Moisture-Checker	Capacitive	I	Yes	75	0.048 – 0.76
Epsilon E100	Capacitive	A	SiO2 2μm	15	DC Cycle

Table 2.2. Summary of instrument assessment. Where the penetration depth is for insulating material with $\varepsilon = 4$, whilst A and I stand for annular and interdigital electrode geometries correspondingly.

Based on these findings, it is concluded that lower price probes might provide very arbitrary readouts, given both the penetration depth is very high and the sampling frequency is not constant. The Cortex conductivity meter has shown great measurement resolution and frequency suitability for skin measurements. Unfortunately, the correlation between stratum corneum hydration and conductivity is

not clearly defined in the literature and the measurement depth over-exceeds the maximum expectations. Having those categories deducted from the list, leaves a direct comparison between Corneometer CM825 and Epsilon E100. Regarding the measurement frequency, the CM825 has been confirmed to be using non-suitable and variable frequency dependant on the dielectric permittivity value of the sample. This frequency variations could introduce a biased error but the range should not be catastrophic for the skin hydration measurements as long as viable tissue is not reached. The Epsilon E100 is assumed to be using direct current charge/discharge cycles based on the fingerprint integrated circuit datasheet description but this cannot be confirmed at hardware level.

According to the literature review in Chapter 1, the normal stratum corneum thickness is between $10-20\mu m$, so both of these instruments have acceptable measurement depth for stratum corneum hydration measurements with the E100 having higher chances to reach viable tissue that will twist the results. Although the E100 technology is miniaturised in comparison to CM825, the latter uses an over-exaggerated thick protective layer to counter-balance the measurement depth of the bulky electrode geometry. This technique masquerades the measurement depth of CM825 as ideal for skin measurements, but at the same time it significantly reduces the measurement sensitivity because only a small portion of the electric field is actually interacting with the sample. Figure 2.13 compares the portion of the electric field that interacts with the sample between E100 and CM825 sensor design. Note, Figure 2.13 attempts to demonstrate the difference in measurement sensitivity and not the measurement depth, the latter has been estimated in Figure 2.5 and Figure 2.12 correspondingly.

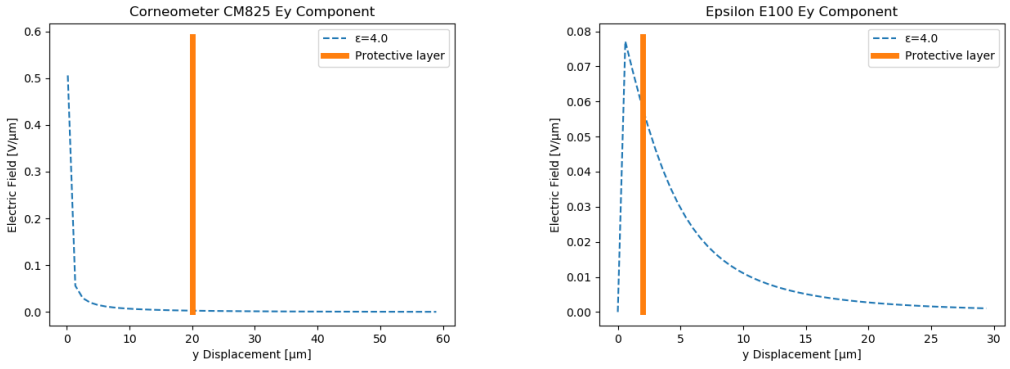

(a) (b)

Figure 2.13. (a) Corneometer CM825 and (b) Epsilon E100 electric field strength against the perpendicular displacement from the centre of the sensor surface. The end of the protective layers is marked with a solid vertical line, and the dielectric permittivity of the glass and the SiO2 is assumed to be equal to this of the sample ($\varepsilon = 4$). This comparison demonstrates the expected advantage of Epsilon E100 in measurement sensitivity.

Until now, Epsilon E100 has shown to be meeting all the design aspects for

becoming an accurate skin hydration probe, apart from a visualisation instrument. An identified caveat is the actual dielectric response of the instrument, which is claimed to be linear by the manufacturer. This, alongside advantages of using a capacitive array instead of a single sensor probe are explored in Chapter 3.

Chapter 3

Advantageous Properties of Capacitive Imaging Arrays in Skin Research

This chapter focuses on the advantages of capacitive imaging systems over single sensor competitor instruments in the field of skin research. Methods are proposed for improving the calibration of capacitive instruments and for expanding their possible applications in pharmaceutical and cosmetic research via image analysis and data processing techniques. Then, a series of experiments are conducted in order to (a) establish the performance of the selected capacitive array Epsilon E100, (b) evaluate the proposed methods and (c) demonstrate advantages based on in-vitro, in-vivo and ex-vivo applications. It has to be addressed early in this chapter that the purity and suppliers of the solvents used throughout this work are not recorded. At the same time, the same solvents were used side-by-side with different measurement apparatuses, and measurement repetitions, reducing the chances that outlier readouts are caused by solvent impurities.

3.1 Data Visualisation

Hardware-wise, the hydration imaging systems in the skin research market are fingerprint sensors originally designed for biometric security procedures. This technology was first used in skin research by Giron Franck, Leveque Jean-Luc and Querleux Bernard and the application is patented by L'Oréal [83]. Various manufacturers of scientific equipment have since acquired rights on this patent and sell non-calibrated capacitive systems for the observation of near surface skin hydration distribution and textural properties via greyscale images. A good example of such products is the MoistureMap MM100 sold by Courage-Khazaka [84], where frame visualisation alongside textural analysis algorithms become possible using software only solutions.

These greyscale images are vital during experimental studies for qualitative control of the samples because skin artefacts and lesions, such as hair, sweat glands'

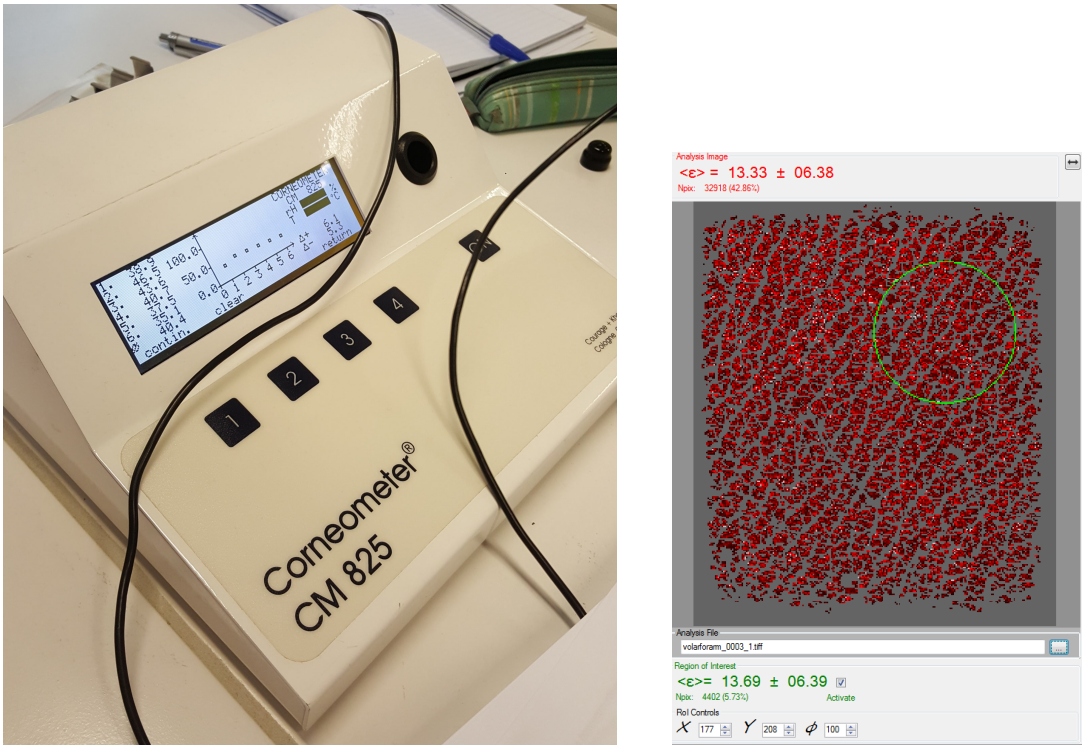

Figure 3.1. Left, the base unit of Corneometer CM825 single sensor hydration probe [82]. The measurement results are displayed in a list and a scatter chart of arbitrary units. The room temperature and humidity are also displayed. Right, an example of capacitive imaging array Epsilon E100 readout from upper volar forearm skin. The red colour in the image represents the skin contact with the sensor surface. The values on the top represent the average dielectric permittivity of the skin across the whole array, while the readouts on the bottom represent the average dielectric permittivity readouts within the selected region of interest (circle at top right corner).

activity, moles, psoriasis, acne etc., can be visually observed on the subject's skin surface. This technique provides a direct visual feedback to determine the suitability of the recorded samples and the selected skin sites after the conduction of an experiment, so the successful acclimatisation process or pitfalls in the experimental protocol can be uncovered, to increase the accuracy and reproducibility of the results. At the same time, samples should be excluded by visual inspection with due caution to ensure that a subjective error is not introduced. Figure 3.2 shows how hair, sweat glands' activity as well as psoriatic and acne lesions are depicted on the greyscale capacitive images. In these images, brighter pixels denote lower capacitance while darker pixels higher capacitance. In Figure 3.2a small hair are visible in bright thick string-shaped lines. Hair has low dielectric permittivity because it mainly consists of dead and keratinized cells [2]. Next, in Figure 3.2b sweat glands' activity can be observed in very dark, high conductance, spots. The underlying pixels of the capacitive array are practically saturated by the high salt concentration in the sweat which results in ionic currents. Finally, the psoriatic and acne lesions have been identified by Xhauflaire-Uhoda in [85] and [86] to be having lower capacitance

than normal skin.

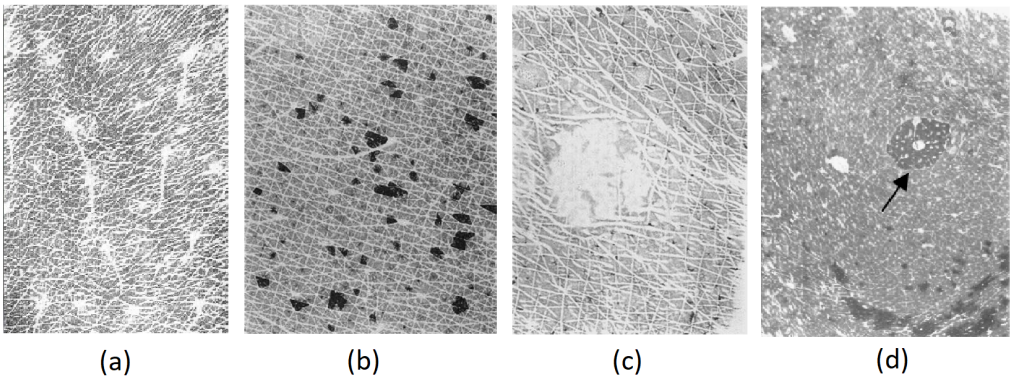

Figure 3.2. Greyscale capacitive images of (a) hair [84], (b) sweat glands' activity [87], (c) psoriatic lesion [85] and (d) acne lesion [86]. These images have been collected from the literature and to the best of my knowledge they are not calibrated. The arrow in image (d) points to an acne lesion.

Whilst this information is very useful for ensuring that the samples are suitable for a study and that the acclimatisation protocols have been carried out properly, it does not meet the full potential of this measurement apparatus. In the next section, the pixel readouts of the greyscale images will be calibrated to linear dielectric response in order to further unfold new applications of such systems in the pharmaceutical and cosmetic industries.

3.2 Greyscale Image to Dielectric Permittivity Map

In order to utilise the capacitive image readouts in further scientific data analysis and in conjunction with different scientific equipment as well as with previous studies, the greyscale pixel values (0 to 255) should be converted into S.I. units that characterise the properties of the sample. With this in mind, Biox Systems Ltd. [1] has first calibrated a biometrics fingerprint sensor to provide both numeric and visual results in dielectric permittivity units - an insulating material property instead of capacitance which is a system property. An in-vitro experiment was conducted in order to demonstrate the difference between measuring system capacitance and dielectric permittivity. Air, deionised water, and solvents with known dielectric permittivity name-values were placed on the sensor surface and the averaged pixel readouts were monitored with and without the calibration unit activated. The room temperature was maintained at $21^{o}\mathsf{C}$ and the relative humidity was between $35-55\%\mathsf{RH}$. The samples and the expected dielectric permittivity readouts are: air (1.0), Decanal (6.2), Heptanol (9.1), PG (32.0), Ethylene Glycol (37.0), Glycerol (42.5) and deionised water (80.1). The achieved results are illustrated in Figure 3.3.

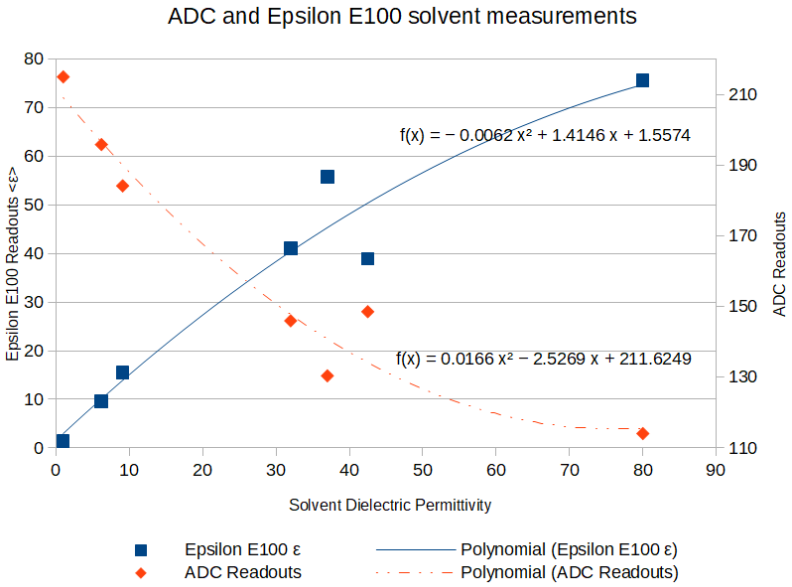

Figure 3.3. In-vitro solvent measurements with Epsilon E100 to demonstrate the difference between measuring system capacitance and measuring the sample's dielectric permittivity. On x-axis, the name dielectric permittivity value of the samples. On the left y-axis, the Epsilon E100 readouts for each solvent in ε units. On the right y-axis, the output of the analogue to digital converter in greyscale (0-255). The second order fitting curves demonstrate the effect of Biox System Ltd calibration in system output linearisation.

The experimental results demonstrate how deceiving the system capacitance (or greyscale readouts) can be when solvents or skin hydration are measured. This is because the system capacitance is not linear to the sample's dielectric permittivity. This is confirmed by the second order gains of the experimental results, which changes from 0.0166 when the sensor is not calibrated for linear dielectric response to 0.0062 when the sensor is calibrated. This calibration method will be presented in the following subsections of this chapter.

A Capacitive Pixel Readout

In Chapter 1, it has been demonstrated how an individual pixel of a capacitive imaging array can be treated as an open-plane capacitor. So, a greyscale capacitive image is practically a matrix of the analogue to digital convertors' output for each capacitor-pixel in the fingerprint sensor array. An adulterated circuit of each pixel is shown in Figure 3.4a, where capacitor C_{pixel} represents the open-plane pixel, V_{charge} the pulse power supply that charges and discharges the pixel periodically and $R_{control}$ the resistor that controls the current flow. Assuming zero initial potential difference across the pixel electrodes when the supply transits from low to high level, the ideal pixel capacitor will take $3C_{pixel}R_{control}$ to charge Figure 3.4b. In opposite manner, assuming fully charged capacitor when the power source transits from high to low level, the pixel will need $3C_{pixel}R_{control}$ seconds to discharge Figure 3.4c.

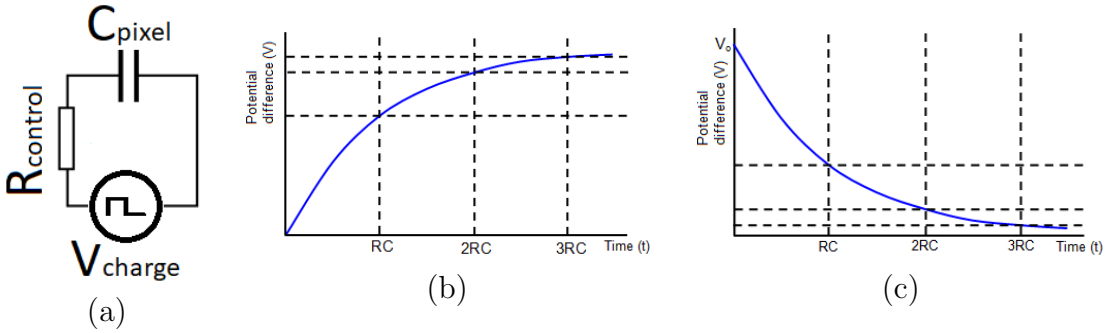

(a) (b) (c)

Figure 3.4. Simplified pixel circuit alongside ideal charge and discharge curves [88]. These help to demonstrate how system capacitance can be calculated when voltage drop and current flow levels are known.

The fingerprint biometric sensors capture capacitive images by fully charging all their pixels and letting them discharge through a current control resistor for a short and known amount of time, called discharge time and ranging between 0 and $3RC$. Then, the potential difference across each pixel is measured using a analogue to digital converter. The conversion from voltage levels to digital values is achieved by Equation 3.1. This digital value practically represents the greyscale tone of the pixel in the un-processed capacitive image.

$$V(t) = \frac{gV_{ref}}{2^N} \implies g = \frac{2^N V(t)}{V_{ref}} \tag{3.1}$$

where:

g = The ADC digital output
$V(t)$ = The voltage level at the moment of sampling
t = The discharge time
V_{ref} = The ADC reference voltage level
N = The ADC resolution in bits

This means that, assuming given pixel geometry and constant discharge time and current, for insulating materials with higher dielectric permittivity the analogue to digital convert will give a lower reading because the capacitor will discharge slower (Figure 3.4b). This comes in agreement with the experimental measurements presented in the previous subsection (Figure 3.3). For the output without calibration, the readings decrease when the sample dielectric permittivity increases, while the calibrated output to dielectric response follows the opposite trend.

Equalisation of Array Digital Response

As demonstrated in the previous subsection, the reading of each pixel depends on multiple electronic components. Unfortunately, in the real world each of these com-

ponents has a slight offset from its name-value tolerance which means that almost every pixel in the capacitive array will provide a different readout for the same insulating sample. Even in the watered-down version of the pixel circuit in Figure 3.4a, an offset in the named value of $R_{control}$ will significantly drift the charge and discharge timings between pixels, which will result to errors in capacitance measurements. Furthermore, there is no guarantee that all pixels will be fully charged, or that a pixel will not leak current before it is sampled or that the analogue to digital converters will meet identical performance.

In order to examine the error that non-ideal electronic components introduce to the capacitive array for dielectric permittivity measurements, the digital pixel readouts for de-ionised water and air samples are recorded for a percentage of pixels in the centre of the sensing surface (i.e. 30000 out of 76800 pixels). The results presented in Figure 3.5 show that water sample digital readouts range from 80 to 130 for different pixels, while the digital readouts for air samples range from 160 to 250. This might be interpreted to an average ±23% error (assuming range from 80 to 250) or standard deviation of ±12.57 and ±5.82 for air and water correspondingly.

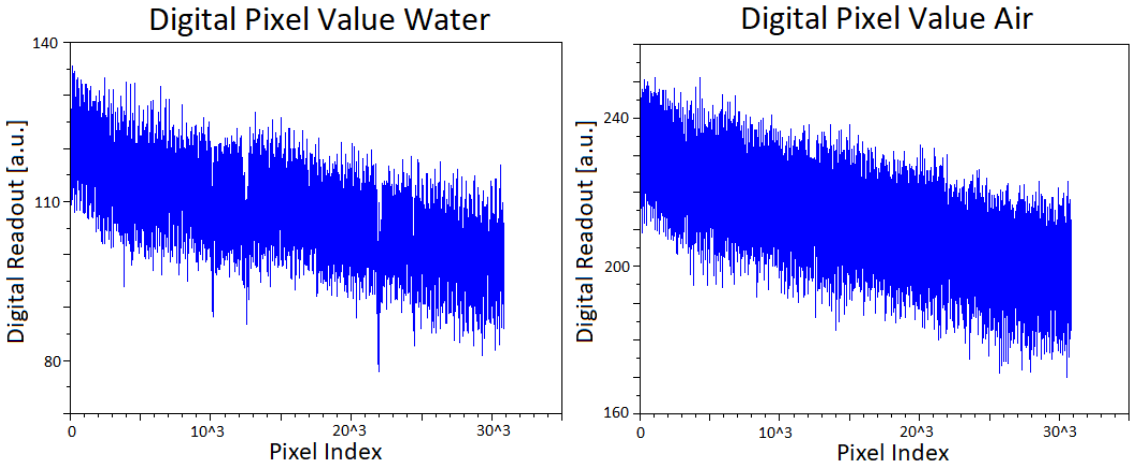

Figure 3.5. Digital pixel response for deionised water and air samples before sensor calibration. This demonstrates the error that is introduced by offsets in the name-values of electronic components in the biometrics fingerprint sensor. Knowing each pixel readout for two points, i.e. water and air samples, as well as the expected readout for these two points, a linear fit can be applied on the each pixel to linearise its response.

In order to correct for these errors, the average digital values for air and deionised water across the array are assumed the most reliable readings. Then, each pixel readout can be corrected with a linear fit by calculating its gain and offset values. For the given set of pixels in Figure 3.5 the calculated slopes and offsets are presented in Figure 3.6 below. The actual performance of array digital response equalisation in dielectric permittivity measurements is demonstrated via experimental work in following subsections of this chapter.

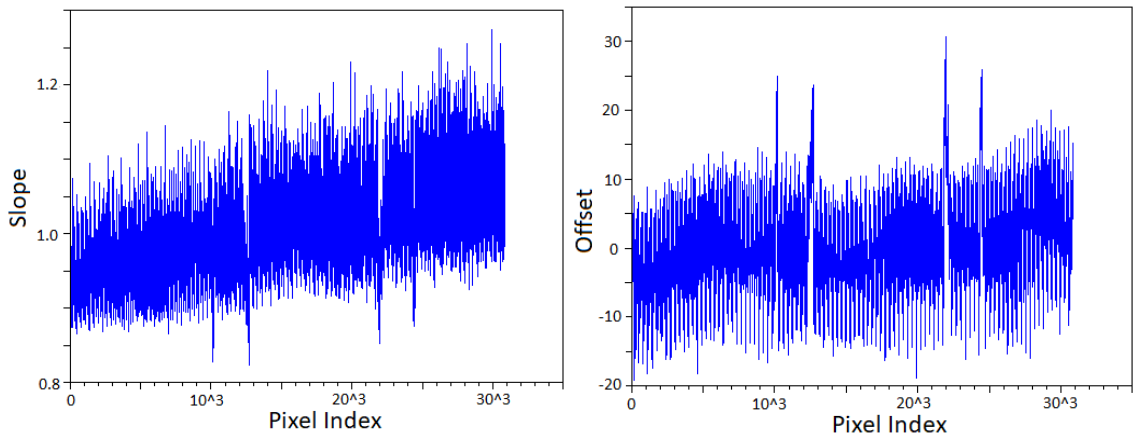

Figure 3.6. Pixel slope and gain that need to be applied on the pixel readings in order to equalise response among the selected pixels of Figure 3.5

Linear Dielectric Response

Assuming that after equalisation all pixels in the array have homogenous response, and that the discharge current and time are known, the digital pixel readings can be converted to voltage levels using Equation 3.1 and one can deduct to the sample's dielectric permittivity using Equation 3.2 and Equation 3.3.

$$V_{pixel}(t) = V_s e^{\frac{-t}{R_{control} C_{pixel}}} \implies$$
$$C_{pixel} = -\frac{t}{R_{control} \ln\left(\frac{V_{pixel}}{V_s}\right)} \tag{3.2}$$

and

$$C_{pixel} = \frac{k \epsilon_0 d}{A} \implies k = \frac{CA}{\epsilon_0 d} \tag{3.3}$$

where:

t = The discharge time
$V_{pixel}(t)$ = The pixel voltage difference
V_s = The power supply voltage
$R_{control}$ = The resistor that controls discharge current
C_{pixel} = The pixel capacitance
k = The dielectric permittivity of the insulating material
ϵ_0 = The dielectric permittivity of vacuum
A, d = parallel plate surface area and distance

Of course, this is an ideal model that does not cover open plate capacitor pixels or the protective layer covering the sensor surface and introducing a double-layered capacitor model. It simply demonstrates the calibration principles without disclosing calibration models of Epsilon E100 provided by Biox Systems Ltd in confidentiality.

3.3 Hydration Percentage Calculation

Establishing numeric readings in dielectric permittivity units opens the path into further conversion and more direct interpretation of experimental results. An important quantity in pharmaceutical industry is the water content or hydration percentage of the sample. Research in the field has shown that water content in human hair and nails could characterise keratin tissue damage from cosmetic and environmental influences. More specifically, Barba C. et al [32] introduced chemical damage in human hair and nail samples and detected increment in $\alpha-\mathtt{relaxation}$ and $\beta-\mathtt{relaxation}$ correspondingly using thermogravimetric analysis, where α and $\beta-\mathtt{relaxation}$ correspond to the external and internal water content of the sample. They concluded that hair treatments, e.g. bleaching and straightening, affect the external water holding capabilities of hair while chemical treatment of nails affect the internal water holding capabilities. Furthermore, Jablecka et al [89] found evidence that $\beta-\mathtt{relaxation}$ in nail samples is higher for diabetic subjects with lower dielectric permittivity values, assuming constant temperature and sampling frequency. In their study, an inductance capacitance and resistance (LCR) bridge by HIOKI was used to measure complex dielectric permittivity and the results indicate that such technology could be used for disease characterisation. There is also previously published work from our LSBU research group [90] that demonstrates how skin water content could characterise irritation, damage and solvent or drugs delivery by measuring permeation.

In order to calculate the water content of a sample recorded by a calibrated capacitive array, it is assumed that the dielectric permittivity of tissue is linearly dependent to this of the dry tissue and pure water. Then, the water content percentage can be estimated using Equation 3.4 [91].

$$\begin{aligned} \epsilon_m &= \epsilon_{dry}(1-\frac{H}{100})+\epsilon_{water}(\frac{H}{100}) \\ H[\%] &= \frac{\epsilon_m-\epsilon_{dry}}{\epsilon_{water}-\epsilon_{dry}}100 \end{aligned} \tag{3.4}$$

where:

ϵ_m = The tissue dielectric permittivity
ϵ_{dry} = The dry sample dielectric permittivity
ϵ_{water} = The pure water dielectric permittivity
H = The water content

3.4 Feature Isolation with Range Threshold

Based on the literature review, the hydration map of the stratum corneum is very inhomogeneous. It is not only the skin hydration levels that change between sites [92] and the non-uniform hydration distribution in the same skin area [14, 15], but also the skin texture that changes with the anatomic site, age and living habits [17, 21, 22]. Furthermore, artefacts like scars, tattoos, hair, sweat glands and lesions can affect capacitive measurements [84, 85, 86, 87]. In section Section 3.1 the advantage of visually inspecting such textural features in skin research was demonstrated, but the capacitive image can be further processed to achieve accurate measurements even when such irregularities exist within the sampled skin area. Such capability can decrease the error in experimental results, increase the number of skin areas that can be examined and increase the number of recorded samples that fit the protocol of the experiment.

In order to achieve accurate hydration measurements independent of human skin textural characteristics between skin sites and individual subjects, a range threshold model is applied on the dielectric permittivity map pixels [93]. The pixels in the skin capacitive image are practically separated into three groups ϵ_{under}, ϵ_{target} and ϵ_{above}. The filtered image is reconstructed only from the pixels that are within the ϵ_{target} group that allows to efficiently isolate skin, or any other artefact of interest, even when texture is highly inhomogeneous. The example in Figure 3.7 demonstrates the range threshold performance in middle dorsal forearm. The snapshot on the left, recorded using Epsilon E100, denotes lower dielectric sample permittivity with darker colors while higher permittivity with brighter colors, ranging from 1.0 to 80.1. The skin area is visible with green color pixels and it is covered with multiple body hair in darker pixels. The average dielectric permittivity across the array is measured to 2.82, which is not representative of the skin hydration because it includes a lot of pixels that are in contact with the hair or in bad contact with the skin (i.e. skin furrow and sensor bezel bad contact). After the application of range threshold, Figure 3.7 right, the hair and bad contact pixels are excluded from the equation. This gives a higher dielectric permittivity and standard deviation readouts, more representative of the actual skin hydration. Since the noise from bad contact is removed, the achieved hydration results can be compared between subjects independent of the hair density in their dorsal forearm.

A more challenging situation that demonstrates the advantages of the range threshold in skin hydration images is illustrated in Figure 3.8 below. In this case, the original snapshot is taken from the thenar eminence skin area, where the stratum corneum is thicker [94] and drier, with wide furrow lines and active sweat glands. The dielectric permittivity of that frame, as would be also recorded by a single sensor

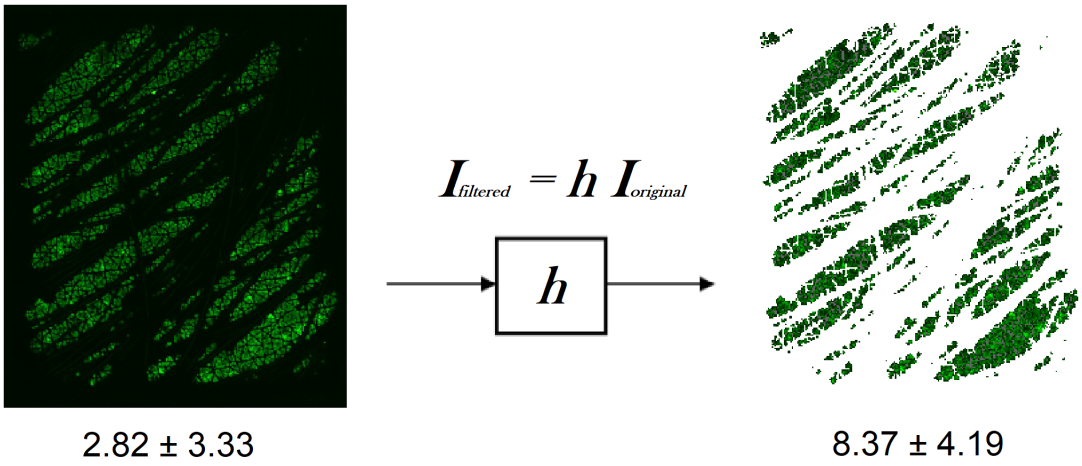

Figure 3.7. Visual illustration of range filtering application on dielectric permittivity images. Left, the original dielectric map, as recorded with Epsilon E100, from the skin area of middle dorsal forearm. Right, the filtered frame. The average dielectric permittivity across the frame changes from 2.82 ± 3.33 to 8.37 ± 4.19 when the filter changes from [0-85] to [3-85]. Also, note that the coefficient of variation between the two frames has changed from 118% to 50%.

probe, is not representative of the skin hydration because it averages bad contact (dark pixels) and saturated pixels from sweat activity (bright spots). In the filtered frame, Figure 3.8 right, the bad contact and sweat activity pixels are excluded from the calculation giving dielectric permittivity readouts and standard deviation that are more representative of the skin.

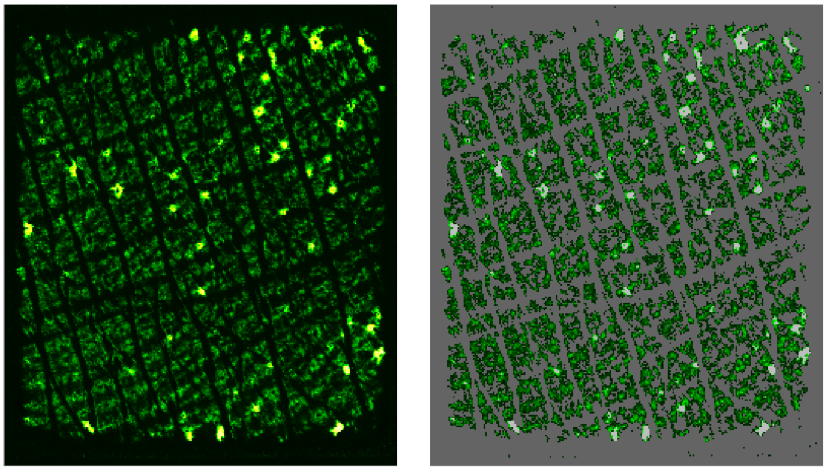

Figure 3.8. Illustration of range filtering application on dielectric permittivity images from thenar eminence site. (a) The original dielectric permittivity map with multiple bad contact areas and sweat gland spots. (b) The filtered frame. The average dielectric permittivity across the frame changes from 4.68 ± 6.75 to 8.35 ± 4.82 when the filter range changes from [0-85] to [3.3-29.4].

3.5 Region of Interest and Image Repositioning

Depending on the nature of the experiment, the ability to capture the exact same skin site plays an important role in setting up experimental protocols and in increasing the reliability of the recorded samples. Examples of such studies could be the drug delivery evaluation through skin or the efficiency of cosmetic products that target only specific lesions on the subjects' skin surface. In this section, a new tool is introduced to enhance the applications of capacitive imaging arrays in cases where measuring the effect of skin products in the very specific skin regions (Region of Interest - RoI) is required by the scientific protocols.

The simplest way to isolate an area of the image is to crop it and calculate the average dielectric permittivity and standard deviation within that RoI. The advantages of this concept are inverse proportional to its simplicity, and they are demonstrated with an ex-vivo solvent permeation experiment in Figure 3.9. More specifically, the experiment studies how Ethanol permeates a piece of pig skin sample. The sample was first acclimatised in $20°\mathsf{C}$ and $35-55\%\mathsf{RH}$ for 20 minutes before it was placed on Epsilon E100 with the deeper skin layers in contact with the sensing surface. Then, a small amount of Ethanol was dropped on the top of the skin and Epsilon E100 software was left to be capturing dielectric permittivity frames at 5FPS. An example frame from this video can be seen in Figure 3.9a. Figure 3.9b demonstrates the effect of RoI application in the achieved results. The top chart takes in account all the pixels inside each frame in order to calculate the average dielectric permittivity. This includes pixels that are not in contact with the skin sample (dark pixels) and its gradient changes suddenly after 1000 frames whilst the solvent spreads inside the skin sample. The bottom chart takes in account only the pixels inside the RoI, the area of solvent application, which results to a smoother curve because it is not affected by the spreading of the solvent in neighbouring skin areas.

In the above example, a RoI is enough to produce the desirable results because the sample's position does not change against the sensor surface during the experiment. It has to be mentioned, that the capacitive sensors are not normally placed under the skin and it would be interesting to place the probe on both sides of the sample to simultaneously monitor surface loss and diffusion into deeper tissue, but the specific experiment targets only to demonstrate the functionality of the region of interest tool. In in-vivo measurements, the samples are usually single snapshots to avoid occlusion and they are recorded over longer time intervals, e.g. days. The solution to this problem is given by the application of an image relocation algorithm that is able to detect the exact same RoI in multiple frames, even when the probe is not perfectly centred on the skin site and without requiring further human in-

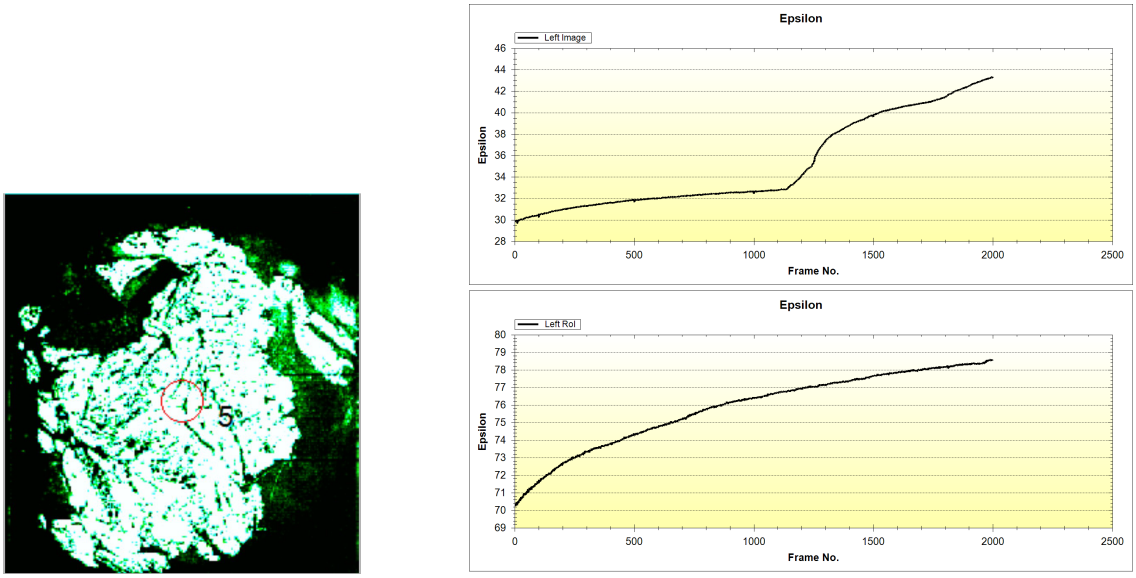

(a) (b)

Figure 3.9. (a) A frame of the recoded video during Ethanol permeation in pig skin sample experiement. The skin sample is depicted with green colour, dark colour pixels are not in contact with the sample, and the red circle in the centre of the sample is the selected RoI. (b) Top, the average dielectric permittivity readouts of the whole image for each recorded frame. (b) Bottom, the same quantity but only for the pixels within the circular RoI.

tervention. The latter is important not only for the reliability of the results, but it also impacts the cost of the experiment by reducing the required human-hours. In order to relocate a selected RoI in a new frames, both are first normalised using Figure 3.5 [90]. Then, the cross-correlation of the normalised matrices is calculated for different coordinates (Equation 3.6 [90]). The pair of coordinates that gives the best correlation, and it is above a reasonable threshold, is assumed the best repositioning fit of the selected RoI in the new frame.

$$I_N = \frac{I - min}{max - min} x255 \tag{3.5}$$

and:

$$Corr_{i,j} = \sum_i \left(\frac{\sum_j (R_N(j) - RM) x (T_N(j-i) - TM)}{\sqrt{\sum_j (R_N(j) - RM)^2} x \sqrt{\sum_j (T_N(j-1) - TM)^2}} \right) \tag{3.6}$$

where:

I	= The hydration map matrix, RoI or frame
min, max	= The minimum and maximum pixel readout in I
$Corr$	= The cross-correlation
i, j	= Pixel coordinates
R_N, T_N	= The normalised region of interest and frame matrices
RM, TM	= The mean of R_N and T_N correspondingly

An example application of RoI repositioning algorithm is presented in Figure 3.10. A dielectric permittivity image on the middle volar forearm was captured, after proper acclimatisation, and a RoI was selected (Normal Skin frame). Then, a droplet of Glycerol was placed on the exact same skin area, and subsequent hydration images were being captured every 10 minutes. The results show that even when the hydration levels in the skin area have been altered and the probe is not well centred, the suggested image repositioning algorithm can detect the same RoI.

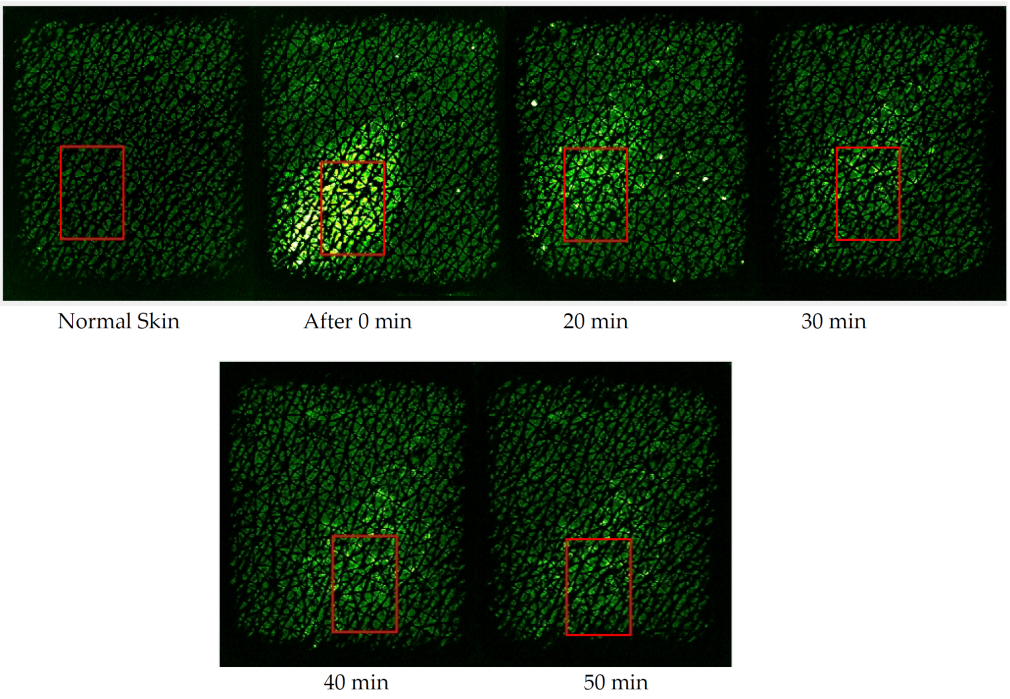

Figure 3.10. Example of reposition algorithm application on in-vivo solvent permeation. The algorithm was applied in dielectric permittivity frames recorded before and every 10 minutes after the application of a Glycerol droplet. The algorithm was able to detect the exact same RoI across all the measurements. [90]

3.6 Experimental Results

Array Calibration Performance

The advantages of capacitive arrays against single sensor probes for skin hydration measurements have been pointed out in this chapter and they will be supported by experimental results in the following subsections. Before doing so, it is important to understand and quantify the measurement performance of the involved scientific equipment (Epsilon E100) as well as the suggested calibration algorithms. For this purpose, an in-vitro solvent measurement experiment was conducted in order to compare the dielectric response linearity of Epsilon E100 with this of Corneometer CM825 - the current capacitive gold standard in skin hydration measurements. Also,

a second modified Epsilon E100 probe (Proposed ϵ) was included in this study, which had the suggested pixel equalisation algorithm injected prior to the default linearisation algorithm provided by the manufacturer. The instruments' readouts for different solvents with known dielectric permittivity values were recorded for each candidate probe while the room conditions were maintained at $21°C$ and $40-60\%RH$. For the Corneometer CM825, the probe was held vertically and each solvent was applied using a micropipette until the sensing surface is completely covered, before pushing the spring-loaded head from the surrounding plastic bezel to trigger the measurement. For Epsilon E100, $80\mu l$ of the solvent was placed at the centre of the sensing surface and the covered region selected with a RoI before triggering the measurement by software. In-between measurements, the probes were wiped clean with lens wipes and were pad dried with fibre free wipes. The selected solvents for this experiment were: air (1.0), Decanal (6.2), Heptanol (9.1), PG (32), Ethylene Glycol (37), Glycerol (42.5) and deionised water (80.1). The achieved results are presented in Figure 3.11.

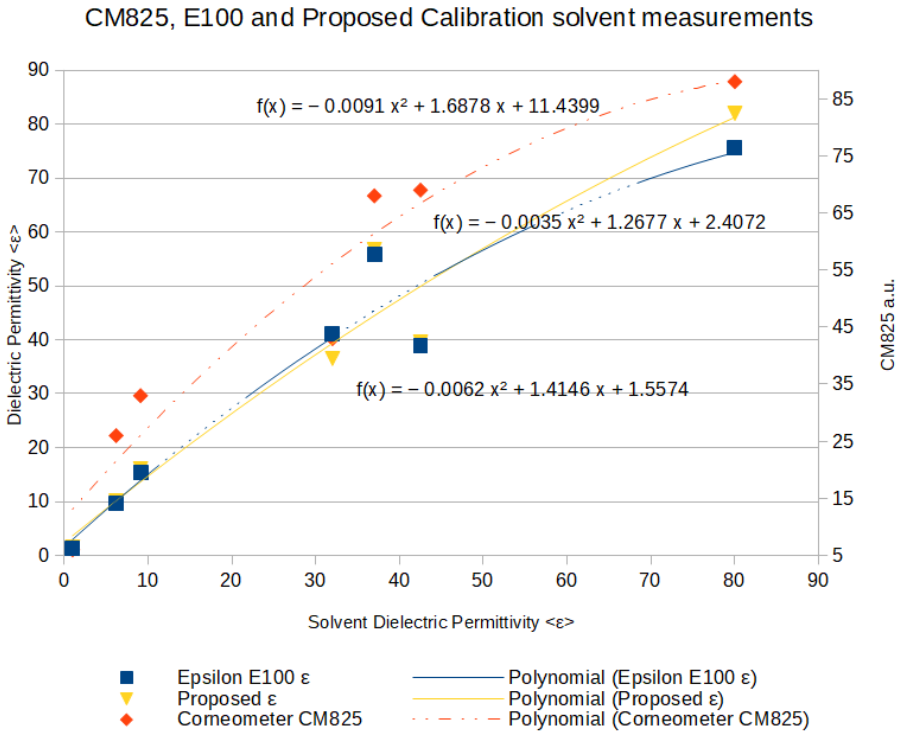

Figure 3.11. In-vitro comparative solvent measurements with Epsilon E100, Corneometer CM825 and the proposed calibration method for Epsilon E100. On x-axis, the named dielectric permittivity values of the solvents. On the left y-axis, the Epsilon E100 readouts for each solvent in ϵ units. On the right y-axis, the output of the Corneometer CM825 in arbitrary units. The second order fitting curves demonstrate that E100 has slightly more linear response than CM825, while the proposed calibration method outperforms both on the subject of the linear dielectric response.

The results of this experiment indicate that Corneometer CM825 uses some sort

of calibration but it does not use a model to convert the measured system frequency, affected by pixel capacitance changes as presented in Chapter 2, into a material property such as dielectric permittivity. The Epsilon E100 is more linear to dielectric response but still lacks in performance over the proposed calibration because it does not take into account pixel abnormality across the sensor array (second order gain of -0.0062 against the achieved -0.0035). In this dataset, it is also observed that Epsilon E100 measurement apparatus cannot cope satisfactorily with specific insulating materials. More specifically, the sensor overshoots for Ethylene Glycol and undershoots for Glycerol, for which solvents CM825 does not. Also, the same behaviour is noticed in digital values readout (Figure 3.3) as well as with the proposed calibration method, which indicates that the sensor generates the error at hardware level. These could be caused by the miniaturised pixels that are more vulnerable to noise, by crystals on the protective layer surface or by the solvent temperature change once it comes in contact with the sensor.

Capacitive Array Homogeneity

The previous experiment demonstrated that Epsilon E100 performs better in in-vitro solvent measurements than Corneometer CM825, but it also generated questions on the actual Epsilon E100 pixel response consistency across the same sensor array. This is an important aspect because many skin research experiments are based on the skin hydration homogeneity or textural characteristics. In order to examine the homogeneity of Epsilon E100 measurement apparatus, a droplet of water was placed at the central area of the sensor surface and a snapshot of dielectric permittivity was captured using the manufacturer's software. The dielectric permittivity range threshold was then used in order to calculate the average dielectric permittivity and standard deviation for the pixels that are in contact with the deionised water. The pixel distribution (Figure 3.12) shows that about 20% of the sensor surface was covered with water and that the average dielectric permittivity and standard deviation for this set of pixels were 78.67 ± 7.86, instead of the expected 80.1. The standard deviation indicates that Epsilon E100 does not take into account hardware abnormalities between pixels. This might be considered approximately correct in specific applications, dielectric measurements of solvents, but it can introduce errors when the hydration map is used in order to study the microrelief of the skin (see Chapter 4).

The measured error in Figure 3.12 is large enough to be visually observed on the recorded snapshots. This is presented in Figure 3.13 alongside the equivalent measurement when the array equalisation is enabled in the calibration process. Also, in the same figure, the image fast Fourier transformations confirm the inhomogeneity by showing higher pixel frequencies when the pixel equalisation algorithm is disabled.

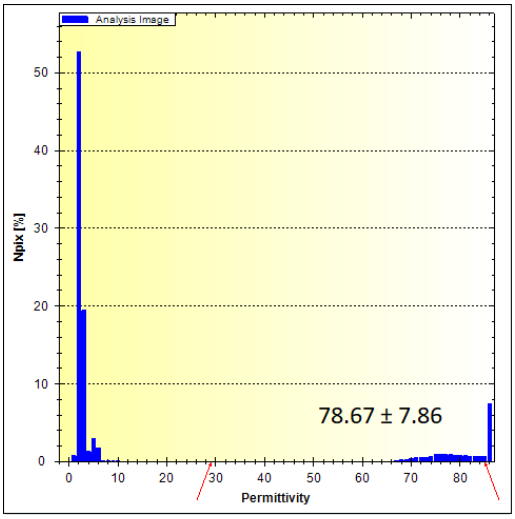

Figure 3.12. Pixel dielectric permittivity histogram for Epsilon E100 with a droplet of deionised water at the centre of the sensing surface. On y-axis, the percentage of pixel in the x-axis corresponding dielectric permittivity group. The cluster on the left corresponds to the pixels that are not in contact with the water drop, while the cluster on the right is of the pixels that are in contact with the water droplet. The two red arrows mark the low (30) and high (85) threshold used in order to calculate the instrument's average readout and standard deviation for the pixels that are in contact with water.

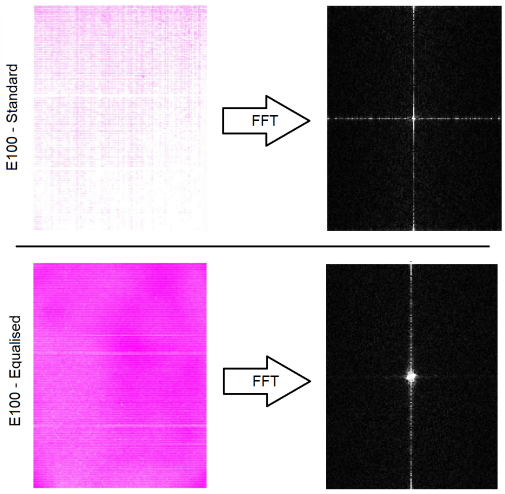

Figure 3.13. Epsilon E100 dielectric permittivity snapshots for deionised water samples with and without the pixel equalisation algorithm alongside their FFT. It is observed that the array inhomogeneity is higher when the pixel equalisation algorithm it is not used, since its shifted frequency spectrum has sharper geometric features denoting more energy in the higher frequencies away from the centre of the FFT output [95].

A second experiment was conducted in order this time to estimate the readout error in different regions on the sensor surface, as well as to compare again how pixel equalisation affects this error. For this purpose, nine sensor regions were selected (Figure 3.14a), to be covered with 10μl of deionised water droplets and capture the dielectric response of the sensor for each of them. The frame capture timer of the instrument was configured to capture each measurement 30 seconds after the

automatic detection of a droplet, this way it was ensured that each of the nine measurements was taken under the same conditions. The experiment was repeated twice, once with and once without pixel equalisation. The captured frames were then processed with the RoI tool in order to isolate the average dielectric permittivity of the region in contact with the water droplet. The achieved numeric results are presented in Figure 3.14b. It was also calculated that the RMSE was reduced from 2.58 to 1.29 when the pixel equalisation was introduced. At the same time, the two-tailed paired t-test shows that there is 6.7% chance that the null hypothesis is true for this dataset, which could be blamed on the limitation of the samples and the number of instruments included in this experiment.

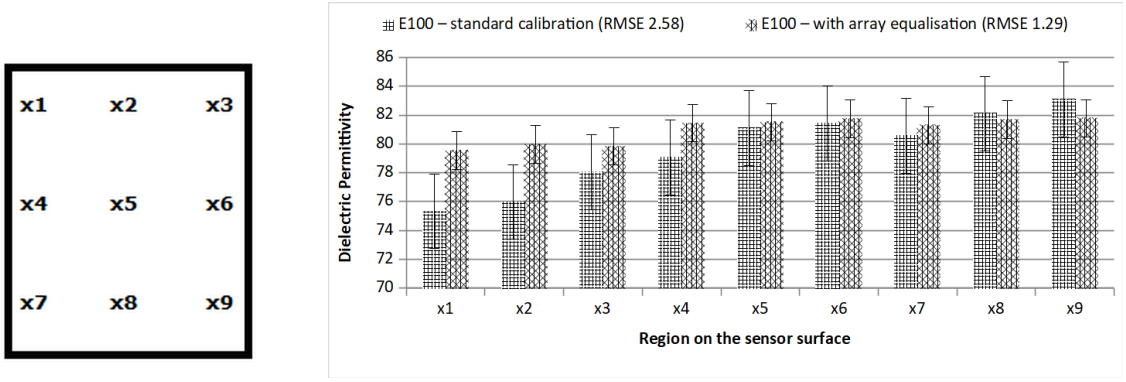

(a) (b)

Figure 3.14. Experimental results for the evaluation of Epsilon E100 sensor homogeneity across its sensing surface. (a) The nine selected regions were droplets of deionised water were placed. (b) The average dielectric permittivity readouts for each of these regions, with and without the array equalisation algorithm.

Consistency among Epsilon E100 Probes

In order to produce evidence to support Epsilon E100 measurement repeatability, ten instruments were used, five of them calibrated by Biox System Ltd. and five of them equipped with the pixel equalisation algorithm alongside the standard calibration. The volar forearm of three subjects was acclimatised for 30 minutes in 21°C and 35–55%RH before three different areas of their volar forearm (Figure 3.15) were recorded with all ten of Epsilon probes. The captured hydration frames of all instruments and subjects were post-processed with a range filter $[5, 50]$ to remove bad contact and possible sweat activity, but no region of interest was used. The selected skin sites were marked to ensure that the probe head will be located at exactly the same place each time. The spring-loaded sensor ensured constant contact force between measurements and probes.

The average dielectric permittivity readouts for each subject, skin site and instrument are presented in Figure 3.16. In order to draw conclusions from this dataset,

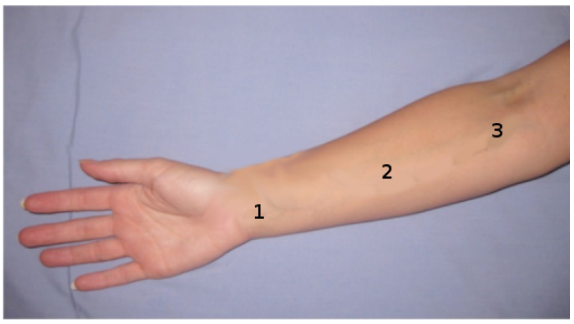

Figure 3.15. Three volar forearm sites that were used for determining the Epsilon E100 measurement repeatability.

the coefficient of variation (CoV) between instrument readouts per subject and skin site were calculated. The Epsilon E100 achieved good repeatability (Figure 3.17a), with maximum CoV of $\pm 11.6\%$. While its array is not equalised satisfactorily on hardware level, the averaged pixel readouts overcome this pitfall when a large portion of the sensor surface is averaged. The results achieved with the second set of Epsilon instruments (Figure 3.17b), after array equalisation, show further improvement in reproducibility between Epsilon probes, with maximum CoV of $\pm 8.9\%$.

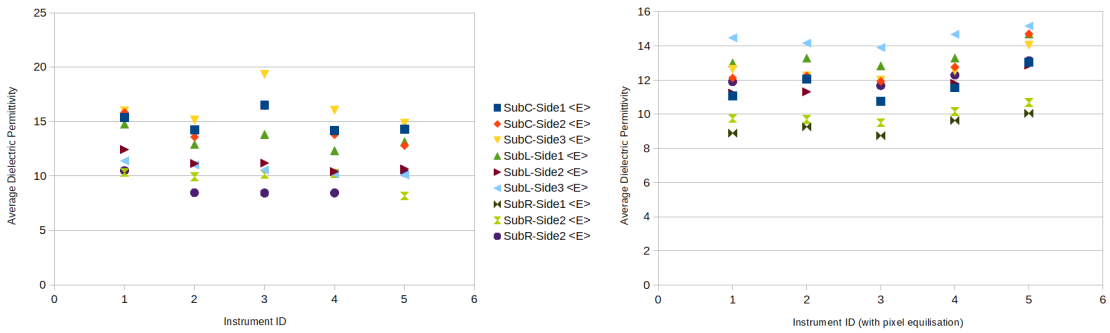

(a) (b)

Figure 3.16. Presentation of filtered dielectric permittivity measurements on three different skin site for three volunteers using ten Epsilon E100 probes. Graph (a) plots the measurements taken by probes with the default Epsilon E100 calibration while graph (b) the ones recorded with Epsilon E100 after the introduction of pixel equalisation.

Effect of Environment Conditions

In this subsection, the Epsilon E100 sensor temperature levels and readouts are studied against room temperature and humidity changes. These environment conditions are very important during dielectric permittivity measurements because they can affect the accuracy of the readouts and the subjects in in-vivo experiment. In capacitive skin measurements, it is recommended acclimatisation in comfortable room environment (i.e. $20-21^{\circ}\mathrm{C}$ and $55\pm 5\%\mathrm{RH}$ [67]) for at least 30 minutes in order to ensure good and consistent measurement quality. Also, the acclimatisation protocols

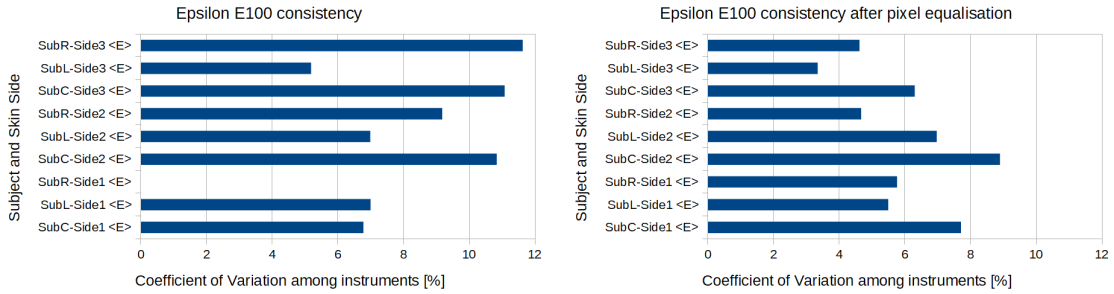

(a) (b)

Figure 3.17. Coefficient of variation between Epsilon E100 probes measurements for the same skin site and volunteers, corresponding to Figure 3.16 data-series.

should always accompany the achieved results in order to allow the reproducibility of an experiment.

To begin with, the temperature of the sensor surface was monitored with a Martindale DT173 (Type K) thermocouple while the room temperature was logged with the SHT31 temperature and relative humidity sensor module by Sensirion. Figure 3.18 shows that the Epsilon E100 sensor surface is 6°C to 4.4°C higher than the room temperature while this changes from 18°C to 25.5°C. This means that when a subject or sample has been acclimatised at 21°C it comes suddenly in contact with the measurement apparatus that is at 26.5°C, which may activate sweat glands and introduce measurement errors. Barel and Clarys [67] state that room temperature above 22°C affect skin capacitance measurements, since the horny layer hydration increases at the beginning of invisible perspiration. An example of experiments that could be affected by this temperature variation is the occlusion based experiments, presented in later subsections, for skin damage characterisation and solvent concentration in in-vivo skin measurements.

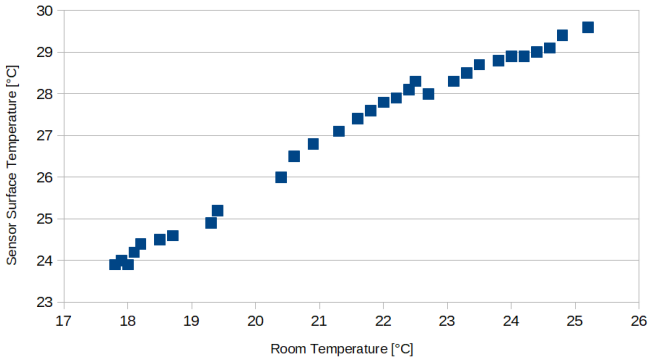

Figure 3.18. Epsilon E100 sensing surface temperature against room temperature changes. The temperature difference ranges from 6°C to 4.4°C for room temperature between 18 and 25.5°C. This is important information in both in vivo and in vitro experiments because it could affect the acclimatisation of the samples.

Whilst the effect of the sensor surface temperature on the results depends on

the nature of the experiment, the effect on the actual instrument readouts can be determined experimentally and be accounted for. Real time temperature and humidity data would allow more accurate calibration to dielectric response as well as real time measurement correction during an experiment. In order to collect the required dataset, an Epsilon E100 probe was taken apart and a simple cooling system was introduced (Figure 3.19a). The source of the heat was found to be the electronics lying on the back of the fingerprint IC, thus a OD2510 Series axial fan for cooling applications with variable speed was used in order to blow the heat out of the system while a thermocouple was providing the temperature feedback. Every five minutes, the dielectric permittivity readouts were logged and the fan speed was modified in order to determine how temperature affects the lower end of the instrument's scale. The results in Figure 3.19b show 0.76% dielectric permittivity readout error for air samples in temperature variations from $24^{o}\mathrm{C}$ to $37.5^{o}\mathrm{C}$. Using the same experiment set up, we recorded videos of the sensor's dielectric response to deionised water samples when the fan is off and when it is in full speed (Figure 3.20). The results show a 5.1% error in the readouts for the same temperature range $(24 - 37.5^{o}\mathrm{C})$. The above reported errors have two sources, the change of the samples' dielectric permittivity and the drift of the electronic components in different temperatures. It is interesting to notice how the water droplet dielectric permittivity readout drifts over time while the sample is being warmed up (Figure 3.20 right E(RoI)-NOFAN).

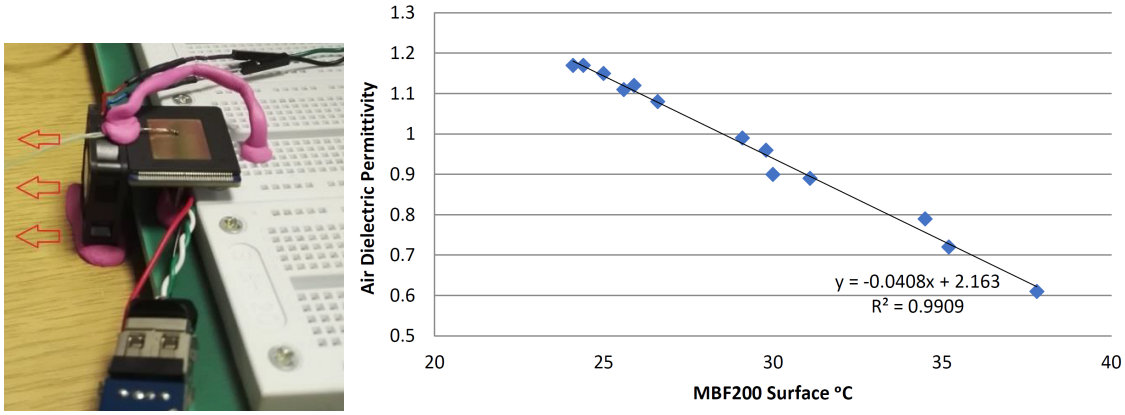

(a) (b)

Figure 3.19. (a) The experimental set up to record air measurements while controlling the sensor surface temperature. (b) The Epsilon E100 sensor readouts for air samples while its surface temperature changes from 24 to $38^{o}\mathrm{C}$. The temperature on the sensor surface was monitored using a thermocouple and it was controlled by a variable speed fan.

Last, the contribution of the room relative humidity to the observed error was examined using a new experiment set up. The sensor was firmly mounted on the side of a plastic cap that allows to maintain the relative humidity stable inside the chamber with silica-gel or saturated salt solutions (Figure 3.21a). The sensor was left to be recording dielectric permittivity frames while an SHT32 was logging the

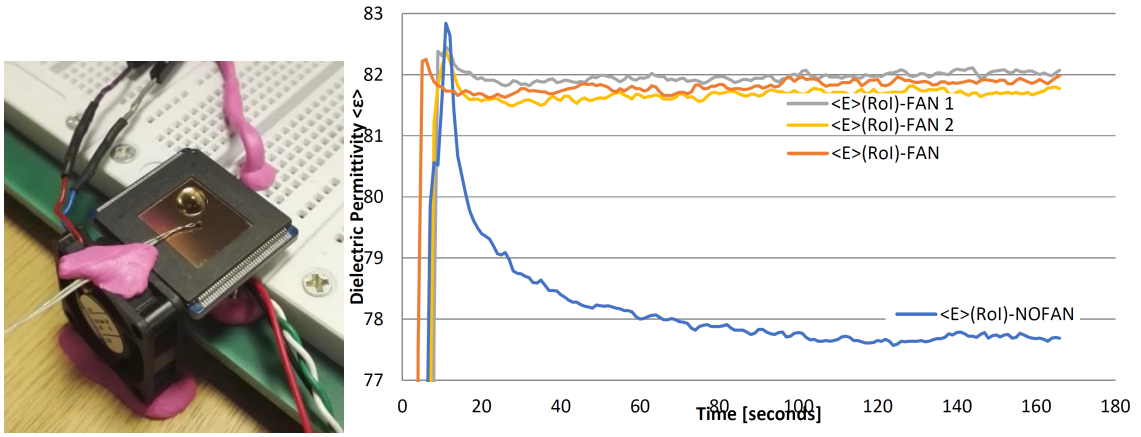

(a) (b)

Figure 3.20. (a) The experiment set up for deionised water measurements with and without cooling the Epsilon E100 sensor electronics. (b) Four videos of dielectric permittivity readouts from the moment that a droplet was brought in contact with the sensor surface - three with the fan on and one with the fan off. The experimental results show that without cooling, the dielectric permittivity readout is significantly reduced i.e. by 5.1%.

relative humidity and the temperature inside the chamber. The experiment was repeated three times, once with silica-gel, once with saturated Magnesium Chloride and once with saturated Magnesium Nitrate saltwater solution. The achieved results (Figure 3.21b) confirm that the relative humidity as well as the temperature affect the sensor readouts and they both have to be taken into account in order to improve the calibration accuracy of Epsilon E100.

Digital Response of Various Capacitive Sensors

Target of this subsection was to evaluate how various fingerprint sensors perform in skin hydration measurement applications, as well as to compare their accuracy to this of Epsilon E100. The latter's sensor is based on a discontinued biometrics sensor by Fujitsu. This fingerprint sensor makes Epsilon E100 unique in the field of skin research because it allows configuration of pixels' discharge time and current by software, which provides flexibility in calibration options. Modern biometrics equipment restrict access to sampling parameters, embed security protocols and in many cases do not even provide access to the un-processed greyscale image.

The main competitor of Epsilon E100 in the field of skin research is the MoistureMap MM100 by Courage + Khazaka electronic GmbH [84] (Figure 3.22). The manufacturer does not disclose the actual sensing module, but it is very likely that the UPEK TCS1CT biometrics model is used [96]. While evaluating its development kit, it became obvious that the silver bezel around the sensing surface plays multiple roles that affect dielectric permittivity measurements. According to the documen-

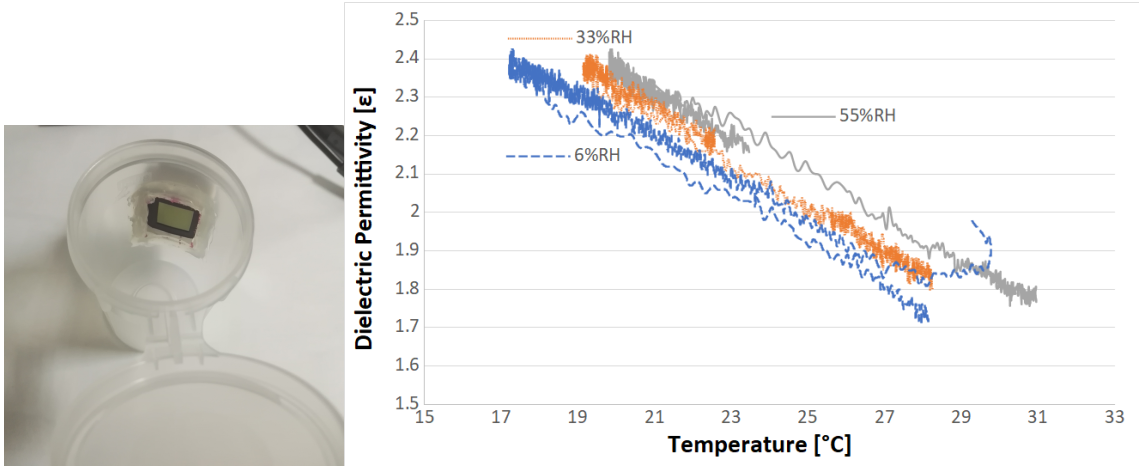

(a) (b)

Figure 3.21. (a) The Epsilon E100 sensor mounted firmly in the custom relative humidity control chamber. Silica gel and saturated saltwater solutions were keeping the relative humidity stable inside the chamber while the temperature was fluctuating from 17°C to 30°C. (b) The recoded dielectric permittivity readouts against the temperature fluctuations confirming that both the environment temperature and humidity affect the sensor readouts for air samples. Note that the sensor used for this experiment differs from the one used in the previous three measurements, which explains the shift in the calibration.

tation, it protects from electrostatic discharge, triggers automatic frame captures and enables advanced calibration and pixel equalisation. Luckily, the technical documentation provides a broad circuit diagram and implies which components have to manually be removed from the circuit in order to disable the bezel (Figure 3.23). There is no way of knowing whether the manufacturer of MoistureMap MM100 applies these hardware modifications but in-vitro measurements would not be possible without them.

The chipset of Epsilon E100 has been analysed in Chapter 2, so details will not be repeated here. In this experiment, two Epsilon E100 probes are tested, named in the results as E100-1 and E100-2, each with different pixel discharge configuration options. The first option is the one preferred by the manufacturer for achieving maximum greyscale resolution. The second current discharge option was solely selected for matching the resolution of UPEK TCS1CT in order to offer equivalent comparison between the modules. The next competitor that was included in this experiment is the FPC1080A swipe biometrics sensor by Fingerprint Cards AB [97] (Gothenburg, Sweden). To the best of my knowledge this is not currently used in any scientific instrument for skin research, but its geometrical characteristics could make it an ideal candidate for measuring hydration level on body sites that it is hard to reach by the previously mentioned bulky sensors. Furthermore, the vendor's software capabilities in swipe-stitching images could be utilised in order to expand possible applications in skin research.

The experimental procedure is simple, all sensing surfaces were cleaned with wet

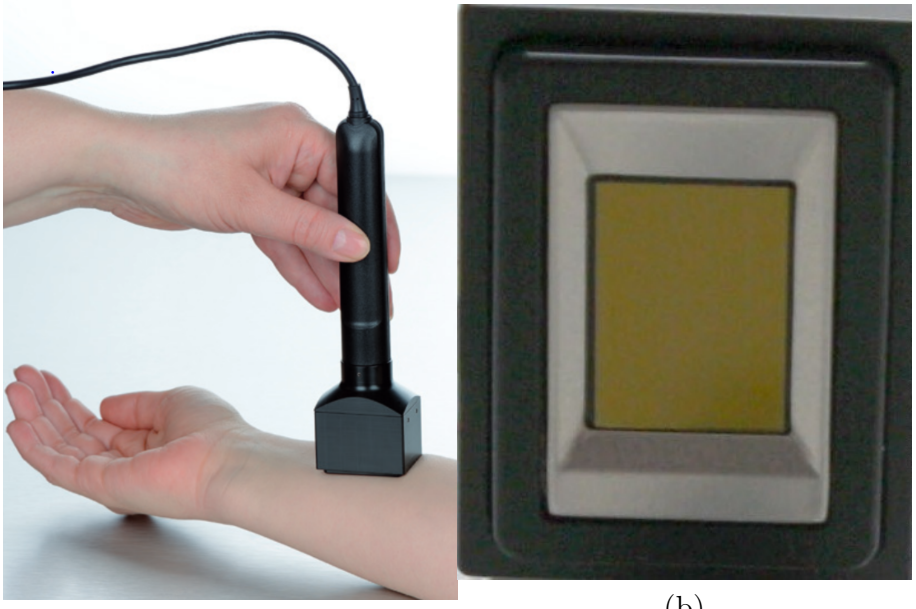

(a) (b)

Figure 3.22. (a) The MoistureMap MM100 instrument as presented in the brochure and (b) a close-up picture of the sensor as presented on the manufacturer's website [84].

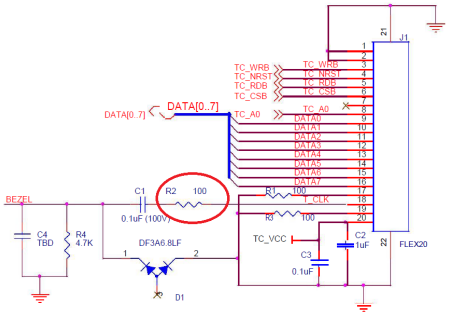

Figure 3.23. UPEK TCS1CT bezel circuit schematics [96]. The circled resistor disconnects the clock pulse from the fingerprint sensor MCU to the bezel. Removing this resistor allows to record measurements without having the sample in contact with the bezel.

lens' wipes and then dried with fibre free laboratory tissues to remove residues from alcohol evaporation. Then, the list of solvent presented in Table 3.1 were placed on the sensor surface and instrument readouts were recorded, while the cleaning process was repeated between each measurement. The results, in Table 3.1 and Figure 3.24 show that the UPEK sensor has the best logarithmic fitting but very low resolution. The custom Epsilon E100 calibration achieved similarly low resolution but its correlation to the expected values remained low. The low correlation of Epsilon E100 chipset derives from the under-shooting readout when measuring Methanol, as similarly observed with Ethylene Glycol and Glycerol in Figure 3.11. Given that the Corneometer CM825 and the UPEK did not show similar over- and under-shoots for the same solvents side-by-side, this indicates a vulnerability of the Epsilon E100 measurement apparatus at hardware level that is not taken into account during

calibration. The swipe sensor readouts demonstrated the higher resolution but the water sample gave a very large undershoot, indicating that the sensor is not designed to operate in a full dielectric permittivity scale and as a result unfit for skin research applications.

Table 3.1. In-vitro solvent measurements with multiple candidate capacitive sensors to determine best logarithmic fit and measurement resolution. The results are in arbitrary units, representing the digital response of the sensors under test. Note CM825 that always provides results in arbitrary units.

Solvents	**Expected**[ε]	**E100-1**	**Swipe**	**CM825**	**UPEK**	**E100-2**
Air	1.0	212.0	239.4	7.0	253.0	234.7
Decanol	6.2	190.0	226.4	26.0	239.0	224.1
Heptanol	9.1	179.0	211.8	34.0	235.0	219.3
PG	16.5	150.0	169.2	57.0	229.0	206.2
Methanol	32.7	105.0	145.2	64.0	222.0	185.0
DMSO	46.7	115.0	128.2	72.0	216.0	191.1
Water	80.1	105.0	13.5	85.0	213.0	187.3
R^2	-	0.90	0.74	0.96	0.99	0.89
Resolution	-	1.35	2.85	0.98	0.5	0.59

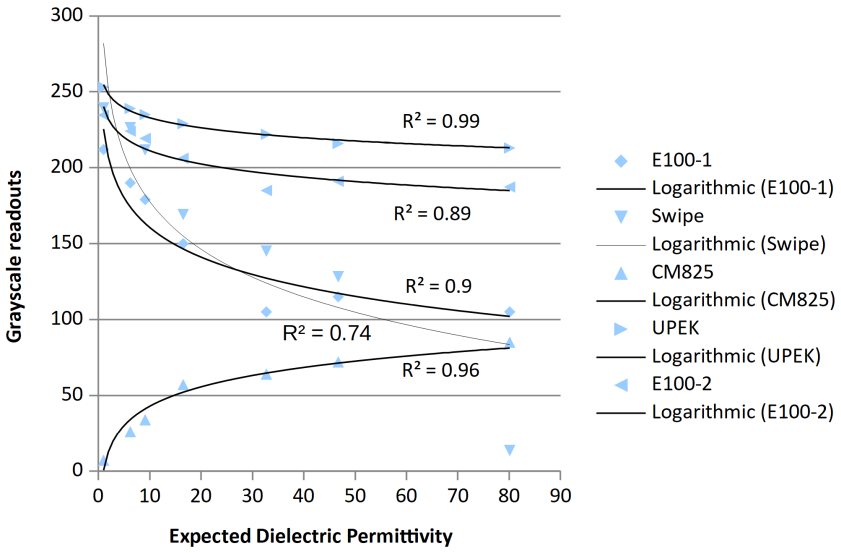

Figure 3.24. Graphical representation of results from the in-vitro comparative study between multiple capacitive biometrics modules.

It worth mentioning that two more biometric ICs were initially included in this experiment but they did not meet the requirements to reach the actual measurement phase. These are the SFC160S-D [98] module by STARTEK Engineering Inc. (Taiwan, R.O.C.) and the FPC1020AM [99] by Fingerprint Cards AB (Gothenburg, Sweden). The SFC160S, although bezel-free and with promising high image sampling rate (30 FPS), was eliminated because the image quality was very low by lossy

data compression and its communication API was not providing access to the raw greyscale image. The manufacturer supports that gain, offset and reference voltage can tune the image quality but the way of achieving it was not clear from the available interface. The FPC1020AM was taking very clear images as long as the sample was in contact with the surrounding bezel. According to the manufacturer the bezel was used only for electrostatic discharge and internal sensor protection. Unfortunately, in Figure 3.25 a quick measurement confirmed that contact with the bezel is required to achieve a clear image, implying that removing the bezel will invalidate its operational function. At the same time, the presence of bezel as vital part of the sampling mechanism will not be in agreement with our electrostatic models and pixel-level dielectric permittivity calibration or measurements are not feasible.

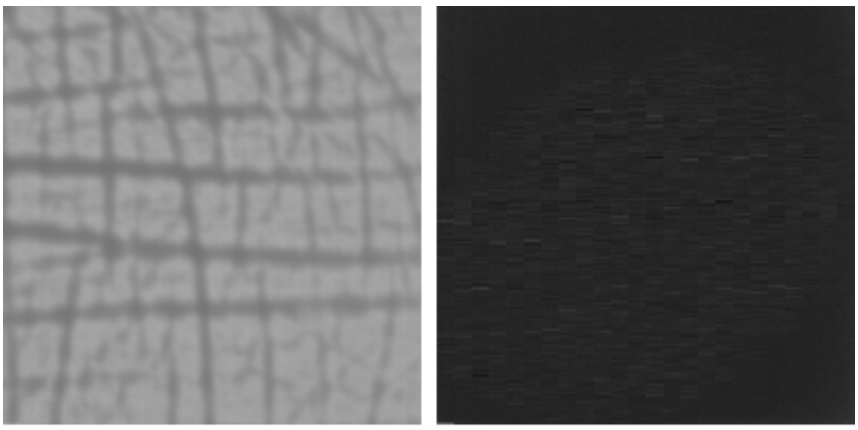

(a) (b)

Figure 3.25. (a) A greyscale image of palm thena area captured with FPC1020AM while the sample is in contact with the sensor's bezel. (b) A greyscale image captured by the same skin area and sensor without touching the sensor's bezel.

Measurement Consistency among Skin Hydration Probes and Skin Sites

A comparative experiment between the capacitive array Epsilon E100 and existing widely used hydration instruments was conducted in order to establish the array's repeatability in relation with the expected standards in the field of skin research. One male and two female subjects were taught how to use three different scientific instruments and they were asked to take repetitive measurements with each probe from specific skin sites, after acclimatising for 30 minutes at $21°\mathrm{C}$ and $35-55\%\mathrm{RH}$. In this way, the coefficient of variation between measurements from the same site, subject and instrument readouts indicate the measurement reproducibility of each apparatus, i.e. smaller the coefficient of variation better the instrument's measurement consistency.

The selected skin areas were the palm, abdomen, cheek, volar forearm and the back of the hand. The subjects were acclimatised before they repeated three measurements on each skin site and with each instrument (Table 3.2). Between each measurement, the sensing surfaces of the probes were decontaminated with alcohol wipes and pad dried with fibre free wipes.

Table 3.2. Experimental results of multi-probe comparative study. Three subjects used three different scientific instruments and recorded five different skin sites of their body. Each measurement was repeated three times in order to determine the measurement repeatability of each instrument. Subject RP requested no measurements on facial skin.

Instrument	**Palm**	**Abdomen**	**Cheek**	**Volar Forearm**	**Back of Hand**
	Subject CB				
E100[ϵ]	5.39	5.2	6.44	7.77	8.88
E100[ϵ]	5.06	4.81	4.54	8.08	9.32
E100[ϵ]	5.77	4.09	5.68	8.14	11.54
CM825[a.u.]	33	44	49	50	50
CM825[a.u.]	33	37	52	50	56
CM825[a.u.]	32	40	43	49	57
Cortex[μS]	70	110	270	140	170
Cortex[μS]	70	110	300	130	140
Cortex[μS]	70	100	200	140	170
	Subject RP				
E100[ϵ]	17.45	3.84	-	4.88	11.22
E100[ϵ]	21.4	3.77	-	4.9	10.72
E100[ϵ]	21	4.05	-	5.02	12.01
CM825[a.u.]	59	37	-	40	49
CM825[a.u.]	63	43	-	40	51
CM825[a.u.]	62	42	-	40	44
Cortex[μS]	250	110	-	90	130
Cortex[μS]	270	80	-	100	90
Cortex[μS]	340	110	-	100	100
	Subject HI				
E100[ϵ]	11.23	3.02	16.63	4.46	3.59
E100[ϵ]	8.92	4.09	19.37	5.36	4.13
E100[ϵ]	8.86	3.57	17.95	4.91	5.64
CM825[a.u.]	44	38	74	38	50
CM825[a.u.]	50	39	74	37	43
CM825[a.u.]	40	36	68	40	47
Cortex[μS]	300	120	170	100	100
Cortex[μS]	260	110	200	90	130
Cortex[μS]	170	110	180	90	120

In order to analyse the above dataset, the data was normalised because the participating instruments have different measurement scales, i.e. Epsilon E100 in dielectric permittivity [ϵ], CM825 in arbitrary units [a.u.] and Cortex in μS (con-

ductive probe). The minimum and maximum scale range of each instrument were identified by sampling air and deionised water. Then, the coefficient of variation for each skin site and subject was calculated and the averaged results per skin site and instrument in Figure 3.26 indicate that Epsilon E100 provides worse measurement repeatability than the existing skin hydration probes in the market.

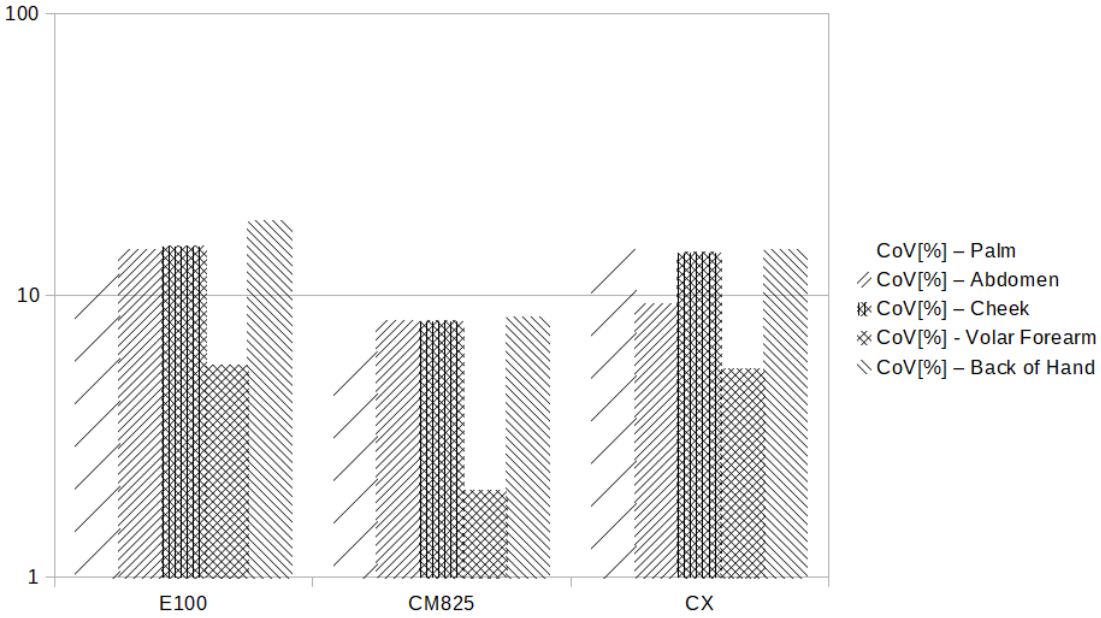

Figure 3.26. Coefficient of variation per skin hydration instrument and skin site to determine suitability of Epsilon E100 in comparison to existing scientific equipment in the skin research market. The achieved high percentage shows that Epsilon E100 has worse measurement repeatability than other skin hydration probes.

Skin Damage Characterisation via Occlusion

Probably the biggest disadvantage of capacitive and conductive measurement apparatuses in skin research is occlusion [48] by prevention of transepidermal water loss or sweat gland activity. When the sensing surface of the capacitive sensor remains in contact with the subject long enough, occlusion will saturate the readings making the results unusable. In order to overcome the occlusion effect, most manufacturers have introduced a fixed timer that triggers when the instrument is pressed against the subject and it forces the sampling within 1-2 seconds time. In this experiment Epsilon E100 is used, which allows recordings of dielectric permittivity videos, in order to explore how skin occlusion under the sensing surface for a period of time can be perceived as an opportunity to expand technology applications in skin research. Non-invasive transepidermal water loss instruments are widely used in literature to examine the skin water barrier function and impairment [100, 101, 102]. So, it is of interest to examine whether the skin hydration percentage change, while the sensor is occluding the skin test site for one minute, can provide adequate information

about the skin barrier function. It has to be noted that the combination of non-calibrated capacitive imaging and TEWL measurements of the occlusion effect for skin damage assessment has been previously studied by Pan et al. [103].

In order to examine this hypothesis, three methods of skin irritation are investigated i.e. intensive washing, tape stripping and application of sodium lauryl sulphate. Repetitive washing, as well as the skin drying method, has shown to be affecting the skin barrier and increasing the transepidermal water loss [101]. Tape stripping is also expected to increase the transepidermal water loss which will return to the baseline while the stratum corneum layers regenerate over a period of days [104]. As it is shown in Chapter 1 and 2, the electrical based measurements will be affected by the reduced thickness of stratum corneum since the electric field will reach deeper skin layers, which is expected to further increase the hydration readouts. The SLS treatment, a common ingredient in soaps for removing dirt and grease from the skin, alters the quality of the lipids in the stratum corneum and increases its hydration levels [105]. These "are speculated to cause a reduction in water binding capacity" [105] of the skin causing skin dryness and irritation [105, 106].

In this experiment skin irritation and damage were introduced, using the three methods above, in the volar forearm skin area of two male subjects between $20-40$ years old. The subjects were first acclimatised in $21 \pm 1^{o}\mathrm{C}$ and $45 \pm 5\%\mathrm{RH}$ for 20 minutes before the skin damage was introduced. The hydration percentage of the affected area was captured with Epsilon E100 before and during the experiments using each time a continuous video capture with one frame per second sampling rate. For the skin irritation with intensive washing, the Fairy product (P&G, Weybridge, UK) was used and the skin was rubbed with it gently for three minutes. Videos of the hydration percentage were recorded before, directly after as well as 10 and 60 minutes after the intensive wash (Figure 3.27a). For the tape stripping experiment, standard clear 3M Scotch sellotape ($25\mathrm{x}66\mathrm{mm}^2$) was used. The occlusion from skin was recorded with the same method before as well as after 2, 4 and 14 strips (Figure 3.27b). Last, Sodium Lauryl Sulfate (SLS) irritation was introduced using a 2% volume ration SLS water solution, held on the skin test area using a plastic well for 5 minutes, before it wiped clean to ensure that no residue left on skin (Figure 3.27c).

The achieved experimental results (Figure 3.27) indicate that capacitive imaging sensors have the potential to characterise skin damage based on the occlusion. For the intensive wash and SLS irritation, increased occlusion and hydration levels are observed right after the treatment while skin dryness is detected 10 and 60 minutes later, which agrees with the reports in the literature [105]. The tape stripping damage results show stable increment in occlusion which also agrees with results in the literature [104, 107].

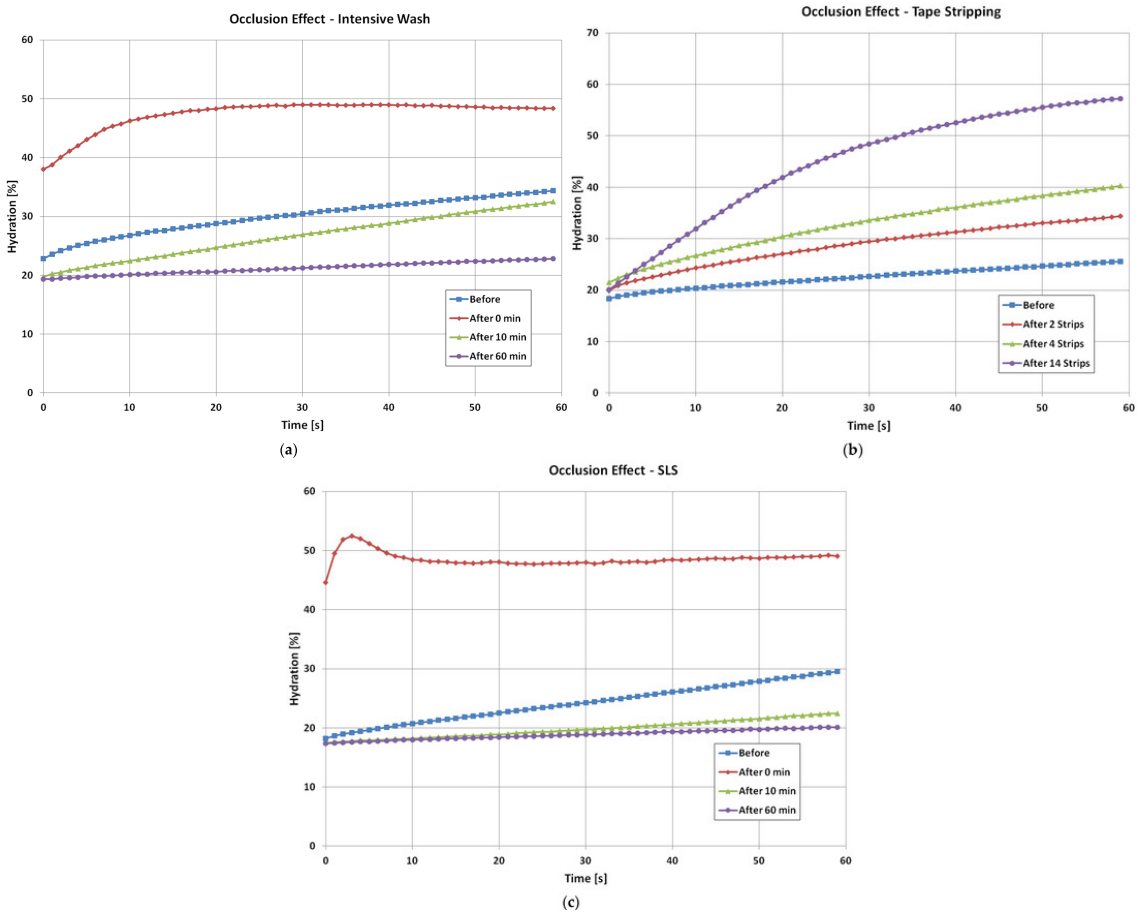

Figure 3.27. Occlusion measurements in the area of volar forearm using a capacitive imaging array after the introduction of skin damage by (a) intensive washing, (b) tape stripping and (c) application of sodium lauryl sulphate

Skin Solvent Penetration

The occlusion effect could also be used in order to study skin solvent penetration. In order to test this assumption, 3ml of pure ethanol, ethylene glycol and glycerol were applied on neighbouring areas of the volar forearm for 5 minutes. In order to avoid evaporation and keep the solvents within the test area, each skin area was covered firmly with a plastic cap during this period. Then, the test areas were carefully wiped clean to remove solvent residue. In order to measure the skin occlusion, bursts of dielectric permittivity snapshots were recorded, with one frame per second frequency, for the period of one minutes before and every 10 minutes after the solvent application. The skin test area was automatically detected in each frame using the relocation tool (Equation 3.5 and Equation 3.6), while the solvent concentration levels in these regions were calculated for each frame using Equation 3.4 and averaged to construct the results in Figure 3.29.

According to Horita et al. [108], ethanol alters the permeability of hydrophilic compounds, and in large concentrations it removes lipids and water from the stratum corneum. This is observed in Figure 3.28, where the concentration percentage

returns back to the baseline within 10 minutes after the solvent application. Based on the review article by Fluhr et al. [109], glycerol is widely known for its moisturising properties, it improves the water holding capabilities, the skin barrier function and the water retention in the skin. This is also observed in the experimental results of Figure 3.28, where the hydration levels of the skin remain high throughout the experiment after the solvent application. At this point it has to be mentioned that while the trends observed match with the literature, the calculated solvent concentration values are not absolute. Since the Equation 3.4 assumes only two compounds involved, i.e. the applied solvent and skin, and does not take into account the water held in stratum corneum. This could also explain the percentage overshoot after the applications of ethylene glycol. Unfortunately, other than the slow permeability of ethylene glycol into human skin [110], no further information was found for comparison with the presented results.

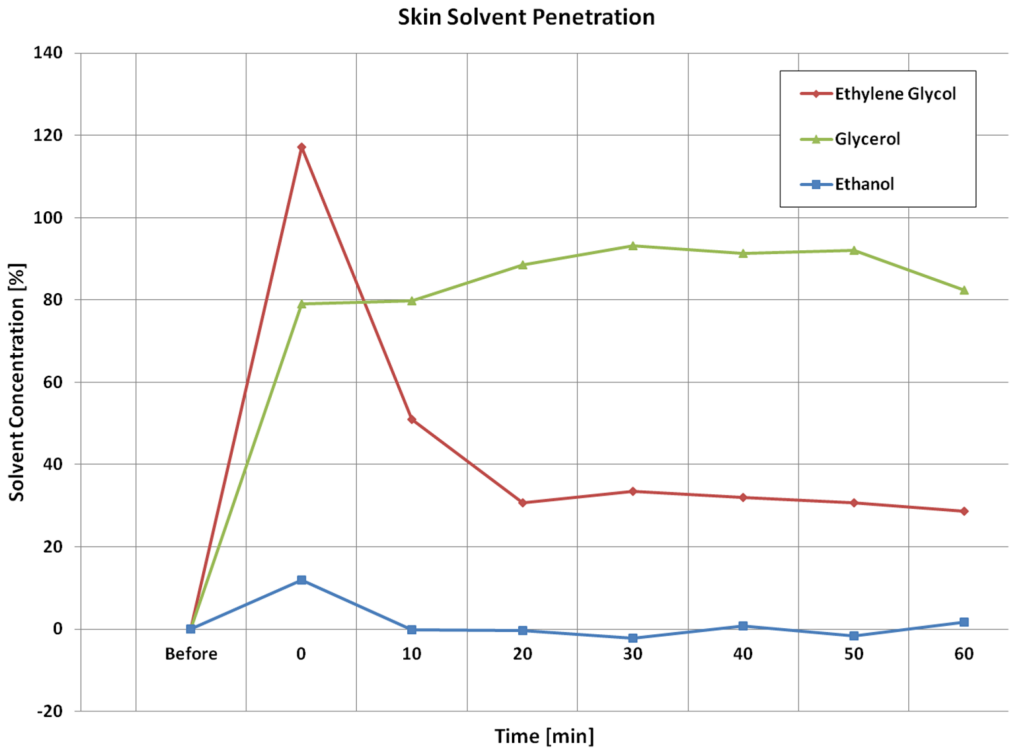

Figure 3.28. In-vivo experimental results from solvent penetration measurements in the volar forearm area by taking advantage of the occlusion effect against the capacitive sensing surface [90]. The results provide information on how fast the solvents permeate stratum corneum, how long they remain in the test area and how they affect the water holding capacity of the stratum corneum.

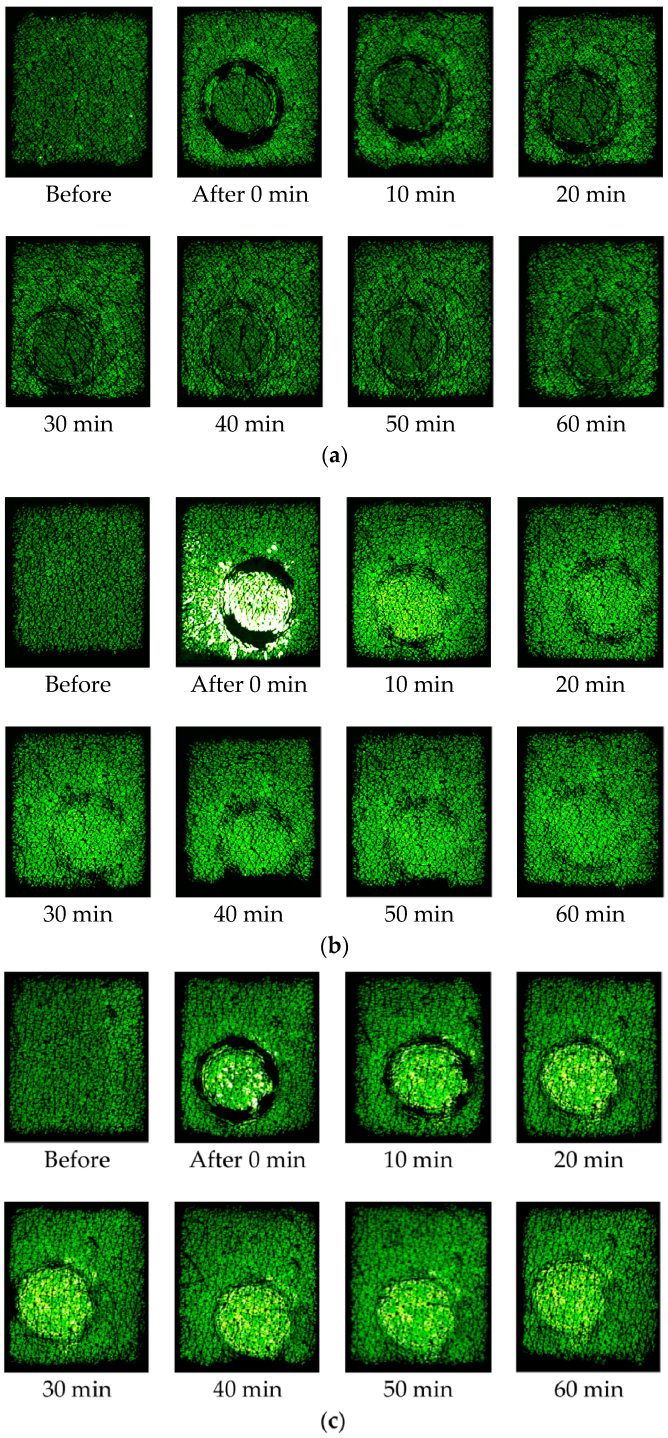

Figure 3.29. Dielectric permittivity video frame instances during the skin solvent permeation measurements corresponding to the experimental results presented in Figure 3.28 [90]. Where (a) corresponds to Ethanol, (b) to Ethylene Glycol and (c) to Glycerol.

Water Desorption in Hair Samples

This subsection extends the experimental work on the evaluation of capacitive imaging arrays in measuring water content percentage of human scalp hair. As it has experimentally shown in the literature [32], the water holding capabilities of hair

can indicate damage from treatments in the cosmetic science. In this experiment, using Equation 3.4, the possibility of using a capacitive array to measure water desorption rate in order to access hair damage, and acclimatisation procedures of the samples, is evaluated.

Figure 3.30. Acclimatisation chamber for hair samples. The bottom of the chamber was housing the saltwater solution to control the relative humidity. A foil with holes was placed in the middle of the chamber and it was holding the sample in distance from the solution but within the same %RH. Last, at the very top of the chamber, a relative humidity and temperature sensor by Sensirion [111] was monitoring the environment condition in the chamber during acclimatisation.

In order to evaluate the performance of a capacitive array in studying the water holding capabilities of hair samples, an experiment was conducted using Epsilon E100 alongside a custom acclimatisation chamber (Figure 3.30). Scalp hair samples from three individuals (30, 33 and 50 years old) were collected, rinsed with deionised water and left to dry in room temperature before being acclimatised in the custom chamber overnight. The acclimatisation environment was regulated using room air conditioning at $21°C$ whilst saturated saltwater solutions were maintaining the relative humidity within the chamber in the desirable levels. After acclimatisation, the samples were taken out of the chamber and held against the measurement surface of Epsilon E100 using an in-vitro plastic plug provided by the manufacturer (Figure 3.31). Dielectric permittivity videos were recorded until the gradient approaches zero or the video length exceeds 5.5 hours. The room conditions were at $21°C$ and $35-45\%RH$.

The experiment was repeated three times for each subject, where each time a different saturated saltwater solution was used in order to achieve different relative humidity in the acclimatisation chamber i.e. potassium nitrate ($85\%RH$), sodium chloride ($75\%RH$) and magnesium nitrate ($67\%RH$). Video instances of dielectric permittivity frames for one of the samples during each repetition are presented in Figure 3.32. The achieved numeric results, after application of a dielectric permittivity range filter and conversion of average readouts to water content percentage, are presented in Figure 3.33 and Table 3.3. It is observed that the calculated water

Figure 3.31. Left, the Epsilon E100 in-vitro stand as presented in the product brochure [70]. Right, the hair sample held against the sensor surface with the plastic plug during the experiment.

content percentage right after removing the sample from the acclimatisation chamber correlates very well (> 0.97) with the relative humidity level inside the chamber. This indicates that such equipment can be used for assessing the correct application of the acclimatisation process prior the conduction of an experiment on hair samples, which comes in agreement with reported results by Claudine Piérard-Franchimont et al. "The method was sensitive enough to disclose a gradient of moisture from the base to the tip of the hair shafts" [112]. Also, the experimental results come in agreement with previous scientific work on water desorption measurements from human hair [23, 113], because they validate that lower diffusion rates are observed in younger subjects (see Slope in Table 3.3). At the same time, the experiment exposed a vulnerability of the in-vitro measurement stand. The need to hold the sample firmly against the sensor surface reduces the surface area of the sample that can be exposed to the room environment. For this reason, the desorption curves recorded by Epsilon E100 show lower gradient throughout the measurement than these we have observed with well established scientific equipment [23, 113].

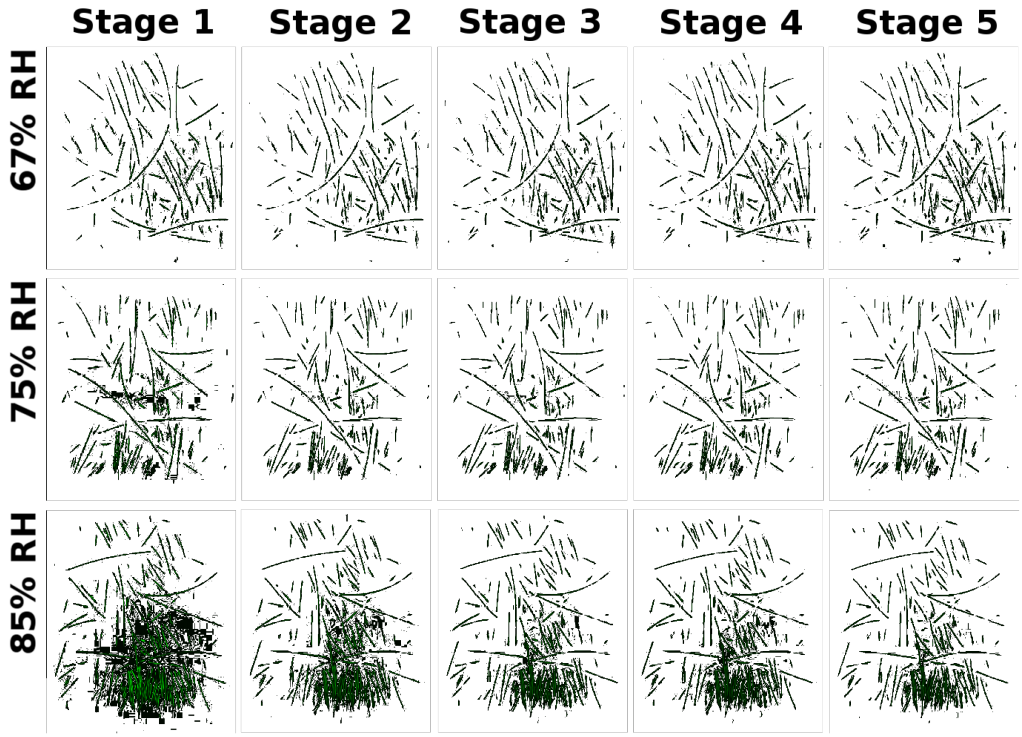

Figure 3.32. Video instances from water desorption experiment in scalp hair samples. The first row shows five frames over time after acclimatization in 67%RH. The following two rows of frames show the same experiment instances when the sample was acclimatised in 75% and 85%RH [114]. The background colours have been removed so the samples are visible in printout.

Table 3.3. Analysis of scalp hair water loss experimental results achieved with Epsilon E100. The left side of the table shows that the water content % correlates well with the %RH in the acclimatization chamber. The right side of the table shows how long it takes for the sample to lose 75% of its initial water content [114].

	Water Content [%]				**75% Water Loss [s]**		
%RH	**Age 30**	**Age 33**	**Age 50**	**%RH**	**Age 30**	**Age 33**	**Age 50**
85	6.0	3.9	4.1	85	2625	2810	2377
75	4.7	3.3	3.7	75	1728	2135	1100
67	3.8	3.0	3.4	67	1490	1604	914
R^2	0.99	0.97	0.99	Slope	64.1	67	83.2

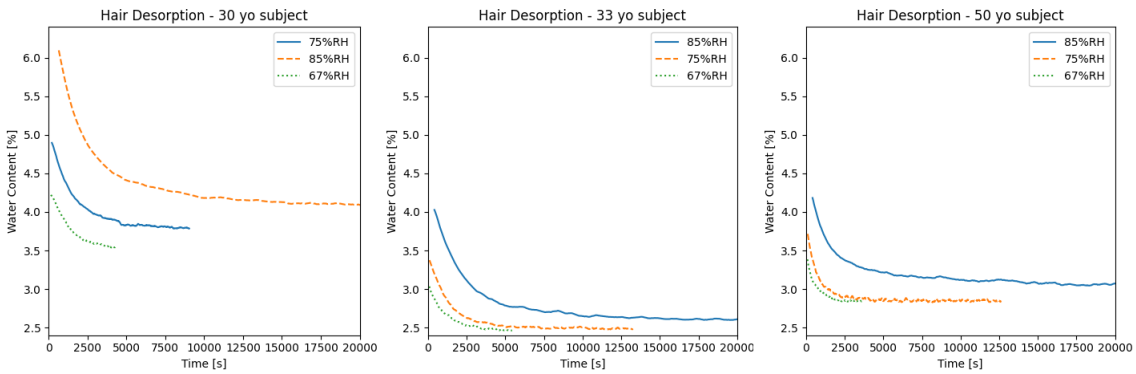

Figure 3.33. Hair water content desorption curves recorded with Epsilon E100 after the applications of dielectric permittivity range filtering. The experiment included hair samples from three volunteers and three different humidity acclimatization levels [114].

3.7 Summary

In this chapter, the advantages of capacitive imaging systems over single sensor probes were presented. First, the importance of data visualisation during data collection was highlighted based on findings in the literature. Then, a watered-down pixel model was used in order to explain how the voltage readings are converted to capacitance and then to dielectric permittivity SI units. Using a sample data-set, the significance of array equalisation was presented and a method for its implementation during system calibration was suggested. Next, a collection of developed algorithms and image analysis methods were presented in order to expand the information extraction beyond skin visualisation and mean dielectric permittivity readouts. The above mentioned were evaluated experimentally in order to determine the measurement quality of Epsilon E100, to identify possible calibration improvements, and to confirm that the instrument meets the skin research community expectations.

In order to examine the linearity of the Epsilon E100 readouts a side-by-side in-vitro experiment with Corneometer CM825 was conducted. The findings suggest that E100 has slightly improved dielectric response when compared against CM825, but the provided calibration method in this chapter has shown margins for further improvement (Figure 3.11). Using similar experimental procedures, the homogeneity of Epsilon E100 array was evaluated and compared against the suggested pixel equalisation algorithm. The results in Figure 3.14 imply that the array homogeneity of Epsilon E100 is very good but there is still space for improvement. Then, the consistency between different Epsilon E100 probes was inspected, with and without the suggested calibration techniques, by in-vivo skin measurements. An in-vivo experiment was selected this time in order to ensure that the results are representative of an actual use case. The coefficient of variation for each subject and skin site among Epsilon E100 probes was satisfactory after the array equalisation was applied, but without the array equalisation the achieved error percentage was twice the one reported by competitor instruments' specification. In the last experiment for this group, the effect of temperature and humidity on the instrument readouts was explored by a series of measurements in different set-ups. The results underlying the importance of proper subject acclimatisation as well as the requirement of consistent environment conditions throughout experiments.

In the next group of experiments, the Epsilon E100 measurement resolution and consistency were directly compared with various skin capacitive systems in-vitro and in-vivo. The results from the in-vitro experiments in Table 3.1 indicate that E100 measurement apparatus has better resolution than the rest of the evaluated systems on hardware level. At the same time, it confirms that Epsilon E100 readouts over- or undershoot for specific solvents, which is not taken into account during

calibration. The in-vivo experimental results in Table 3.26 show that Epsilon E100 lacks measurement consistency when compared with the rest of the instruments in the market. More specifically, the average coefficient of variation is ±13% for Epsilon E100 against ±6.6% that was calculated for the Corneometer CM825.

Next, the proposed water content calculation and image analysis algorithms were assessed via case study experiments. More specifically, skin damage characterisation was achieved by calculating the hydration percentage of occlusion in excess of damaged skin sites, solvent permeation rate and persistence in stratum corneum was measured by calculating the solvent concentration percentage over time, and proof-of-concept experiments of water sorption rate in human body appendages were presented. The results of these experiments demonstrate the advantages in using calibrated capacitive imaging system as well as the possible new applications of this technology in skin research.

All in all, the Epsilon E100 at its current development stage is within the expectations for skin research measurements but there are still possibilities for improving the measurement quality. Furthermore, the sensor array implementation showed improved measurement sensitivity and linearity as well as potential for new application. The latter is examined further in Chapter 4, where advanced image processing algorithms are employed.

Chapter 4

Skin Mirco-relief Analysis using Capacitive Imaging

This chapter focuses on the use of capacitive imaging systems in skin characterisation based on parameters that are not directly related to hydration, in order to replicate measurements that usually require advanced dermoscopic equipment. Many studies in the literature have correlated skin surface micro-relief with skin aging or effects of cosmetic products. Corcuff et al. [54] detected skin furrow orientation, density and depth by taking pictures of rotating volar forearm negative skin replicas under oblique illumination. They concluded that subjects have either one or two main micro-relief orientations in the volar forearm area and that the percentage of subjects with two orientations decreases with age. Also, by repeating the experiment for different elbow angles in order to change skin strain, they confirmed that younger subjects tend to buffer strain between the two orientations (Figure 4.1a-c) while in elderly subjects the single micro-relief orientation is rotating during arm extension (Figure 4.1d-f).

Zahouani et al. [115] arrived in similar conclusions using 3D confocal microscopy images of volar forearm from 120 Caucasian women. Based on their results (Figure 4.2), they explained that the lines in the primary orientation are related to the Langer's line, they intensify with age and they are deeper than $60\mu m$ [115]. The lines in the second mirco-relief orientation are related to the elastic fibres network of the skin, so they are shallower and fade with age [115].

Gao et al. [116] used an image acquisition device alongside a segmentation algorithm to count the Number of Grids Automatically (NGA). They verified its reliability by comparing the results with manual grid counting in dorsal hand and they found negative correlation between NGA and age, sun-exposure and Beagley-Gibson score. Their results come in agreement with [117], where Trojahn et al. studied the number of polygons and skin roughness against age in the area of volar forearm. They concluded that the number of grids correlate with age but not with

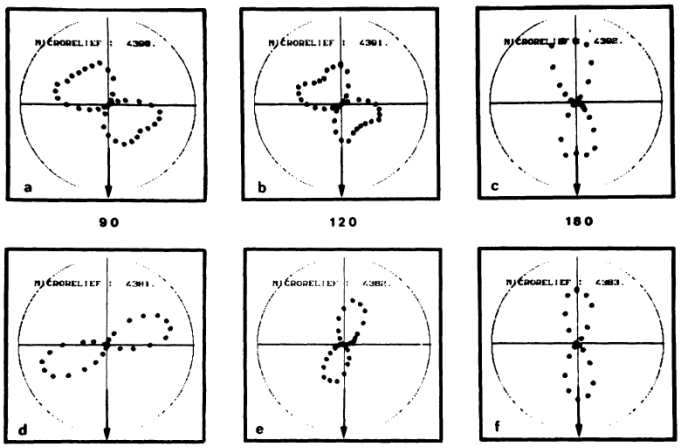

Figure 4.1. Mirco-relief angular distribution in a young subject (a, b, c) and an aged subject (d, e, f) for 90°, 120° and 180° elbow angle [54]. The skin furrow orientation, density and depth were detected by taking pictures of rotating volar forearm of negative skin replicas under oblique illumination. [54] concluded that subjects have either one or two main micro-relief orientations in the volar forearm area.

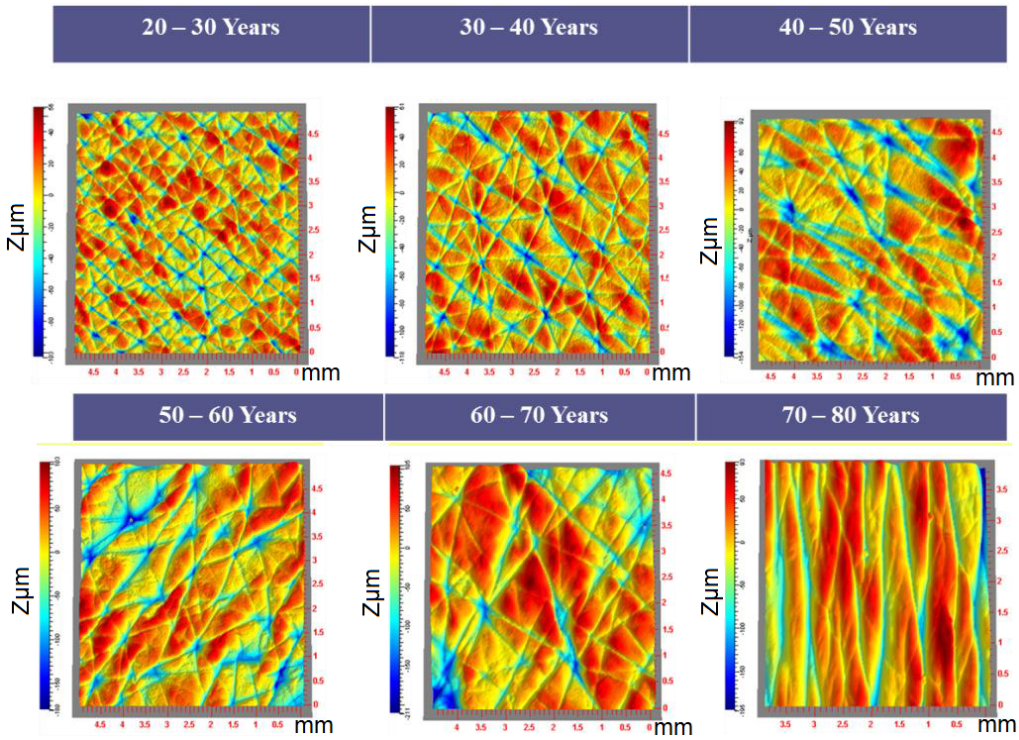

Figure 4.2. 3D confocal spectroscopy snapshots from volar forearm of Caucasian women in different age groups [115].

skin toughness. Also, they identified the need of algorithm development to automate the grids counting process [117]. Furthermore, researchers from Kao Corporation examined annual variations in the intensity of facial wrinkles by capturing images and creating replicas of "wrinkles on the forehead, corner of the eye, lower eyelid and nasolabial groove" [118]. While they did not find changes in the intensity of wrinkles, 3D analysis of skin replicas indicated annual increment of their depth in

the area of eyes for men. Eunjoo Kim et al. [119] compared how age correlates with skin bio-mechanical properties of neck in contrast to other body sites. This site was selected because, in contrast to face, skin is flexible and extensible with intense aging patterns while still exposed to the sun. The results shown that average wrinkles' depth in the area correlates better with age, skin elasticity, skin color and TEWL than in other body sites.

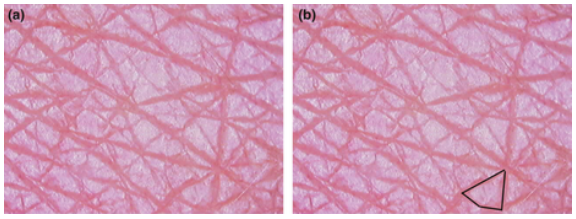

Figure 4.3. Example of human skin grid [116].

The majority of these studies depend on light-based imaging devices and 3D representation of skin surface to allow micro-topographic feature extraction. During the last decade, capacitive imaging systems for skin hydration are becoming commercially available. These are more affordable and portable than conventional skin imaging systems and studies indicate they are capable of providing adequate information on micro-topography. Lévêque and Querleux [120] achieved to detect the orientation of skin lines and calculated the number of intersections and the density of corners. Bevilacqua et al. [16] used a different approach to detect micro-relief orientation and produced a wrinkles-enhanced image (Figure 4.6), which helps to control over-segmentation of skin grid counting algorithms [121]. The latter group stretched the technology further by equipping the device with a pressure sensor and achieving accurate wrinkles depth profiling up to 50µm [122]. While 50µm is poor for skin profiling, it clearly demonstrates future capabilities of capacitive imaging.

In the rest of this chapter the Epsilon E100 capacitive imaging system is introduced and existing algorithms for micro-topographic texture analysis are presented alongside suggested modifications for their application on the specific equipment. Then, the implemented algorithms are evaluated through comparison of experimental results with those reported in the literature. Based on these, conclusions are drawn and suggestions for algorithm optimisation are provided.

4.1 The Epsilon E100 capacitive imaging system

The major advantage of Epsilon E100 system over other capacitive imaging, and single sensor, skin hydration systems is the calibrated response to dielectric permittivity units (ε). The visual representation of ε is black for the lowest dielectric

permittivity and becomes brighter with scale value increment. The scale ranges from 1 for air to 80.1 for water (Figure 4.4).

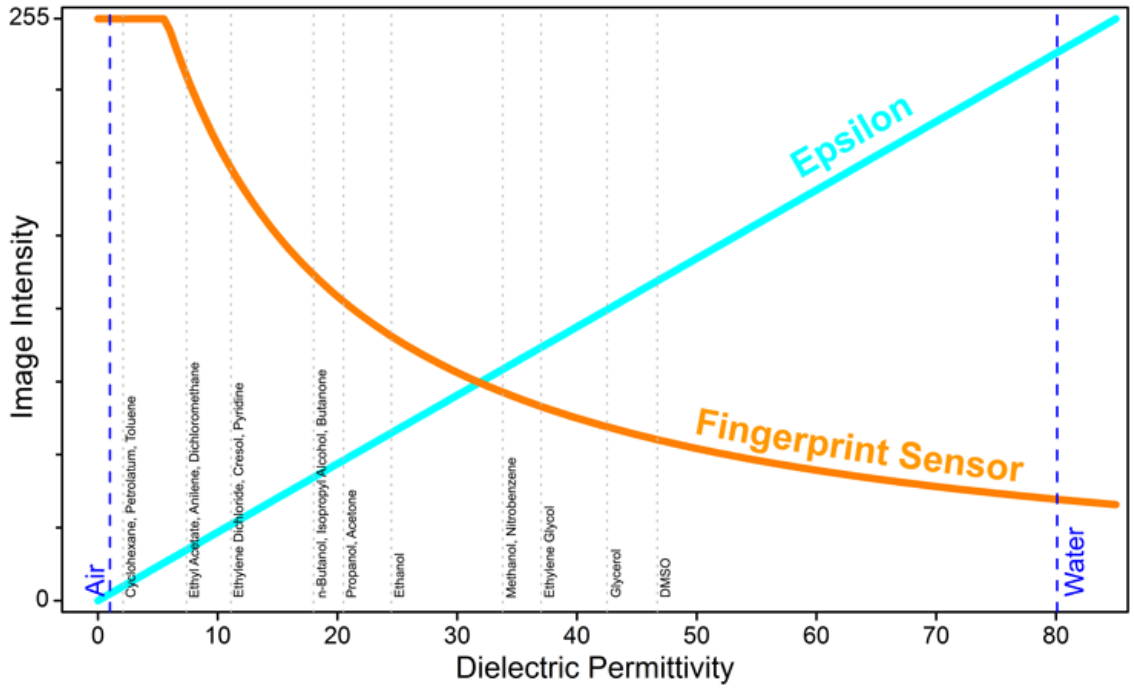

Figure 4.4. Representation of Epsilon E100 linear calibration.

According to the manufacturer's website [1]:

> *"The reason we emphasise dielectric permittivity rather than capacitance is calibration. Dielectric permittivity is a material property that can be used for calibration, whereas capacitance is a device property for which no calibration standards are available".*

Moreover, the software provides competitive advantages with unique analysis tools. The user can analyse snapshots (ε-snapshot) and videos of dielectric permittivity, focus the results on different frame areas using a circular region of interest and filter out artefact of the skin surface using a range threshold filter (ε-filter). The ε-filter plays an important role in micro-relief algorithms' development because it allows to focus on different components of the skin texture. Figure 4.5a-b illustrates how the ε-filter can exclude (gray-out) hair, bad contact and wrinkles as well as the effect of these artefacts in skin hydration measurements. Similarly, Figure 4.5c-d shows how we exclude wrinkles and sweat activity.

4.2 Skin Micro-relief Orientation

The literature review sets major targets of micro-relief analysis in volar forearm the orientation and intensity detection of skin primary and secondary lines. These,

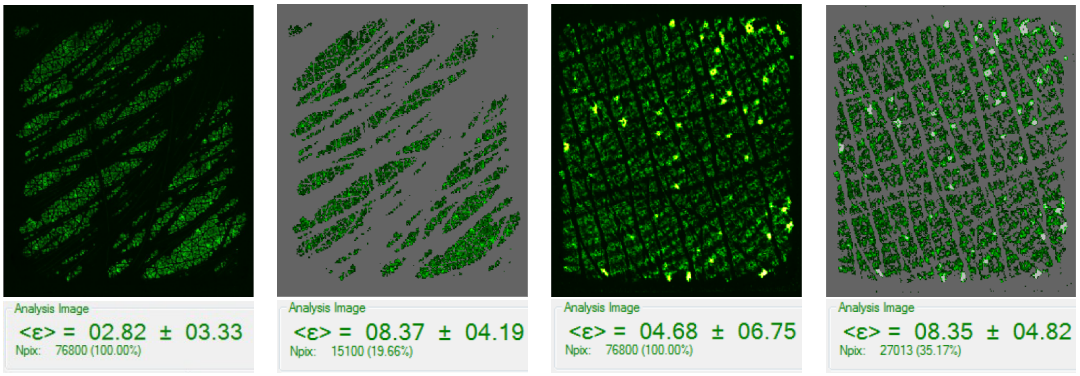

(a) (b) (c) (d)

Figure 4.5. ε-filter usage examples: (a,b) in the area of dorsal forearm to exclude bad contact and hair, and (c,d) in the area of thenar eminence to exclude bad contact and sweat gland activity (bright spots)

along others, are well defined by Hashimoto [123]:

- The primary lines are clearly marked and are between 20 and 100μm deep.
- The secondary lines are more discrete, correspond to a depth of 5-40μm and are perpendicular to the primary lines.

There are two candidate image processing algorithms for extracting the orientation of lines from an image. The first approach is based on a rotating bidimensional Gaussian filter and the second one is based on Grey Level Co-occurence Matrix. In the following sub-sections, both of these approaches are summarised, adapted and evaluated for capacitive imaging systems. Furthermore, enhancements are proposed to further expand possible applications in skin research. Last, experimental results are presented and conclusions are drawn based on these.

Bidimensional Gaussian Filter

Bevilacqua et al. [16], after applying a normalisation algorithm, scan all the pixels of a grayscale capacitive image with a rotating asymmetric bidimensional Gaussian window (Equation 4.1) to detect the skin lines orientation. When the skin micro-relief lines are aligned with the selected orientation θ, the filter's product will indicate a peak value.

$$G(x, y; \theta) = \exp\{-\frac{1}{2}[\frac{x_\theta^2}{\sigma_{x_\theta}^2} + \frac{y_\theta^2}{\sigma_{y_\theta}^2}]\},$$
$$\text{where } x_\theta = x \sin\theta + y \cos\theta \text{ and } y_\theta = x \cos\theta - y \sin\theta \tag{4.1}$$

The major advantage of this method is the production of the line-enhanced snapshot in Figure 4.6, which is useful in further image analysis (e.g. image stitching or counting of skin grids). The line-enhanced image (E) is calculated by Equation 4.2.

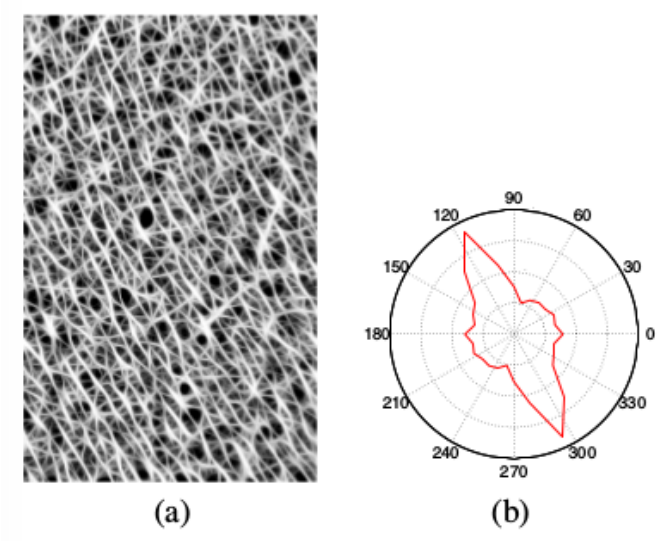

Figure 4.6. (a) The line-enhanced image of a 44 y.o female and (b) the corresponding lines orientation chart using 2D asymmetric Gaussian filter [16].

$$E(x,y) = max\{O_{\theta_i}(x,y), \theta_i = i\frac{\pi}{N}, i = 0...N-1\},$$
where N the number of examined orientations
and O the filtered frame in orientation θ (4.2)

Unfortunately, when this approach was tested with capacitive skin images, the pre-required image normalisation proved unable to cope with various hydration levels which means that a global system calibration was not possible (data not shown). Poorly hydrated samples require greater standard deviation than more hydrated ones. Correspondingly, insufficient normalisation may hide parts of micro-relief from the Gaussian filter output, while intense normalisation will augment wrinkles. Furthermore, as [16] concluded, the algorithm cannot cope with long and short or wide and narrow wrinkles simultaneously, since the configuration of $\sigma^2_{\theta_x}$ and $\sigma^2_{\theta_y}$ in Equation 4.1 contradict.

Grey Level Co-occurrence Matrix (GLCM)

To the best of my knowledge, Lévêque and Querleux first suggested the use of contact imaging systems to study skin micro-relief alongside hydration. In their study [120], the correlation feature of GLCM was plotted against different angles allowing to detect skin micro-relief orientation. The GLCM P of a grayscale image

I for displacement d and angle θ is calculated by [124] and [125] as in Equation 4.3.

$$\begin{aligned} P(i,j,d,\theta) &= \sum_{x=0}^{n}\sum_{y=0}^{m} 1, \text{ if } I(x,y)=i \text{ and } I(x+d\cos\theta, y+d\sin\theta)=j \\ P(i,j,d,\theta) &= \sum_{x=0}^{n}\sum_{y=0}^{m} 0, \text{ otherwise.} \end{aligned} \tag{4.3}$$

Then, the correlation feature can be extracted by Equation 4.4.

$$\begin{aligned} COR(d,\theta) &= \frac{\sum_{i=0}^{G-1}\sum_{j=0}^{G-1} ij\hat{P}(i,j,d,\theta) - \mu_1\mu_2}{\sigma_1^2\sigma_2^2}, \\ &\text{where, G the gray-tone levels and} \\ &\quad \mu \text{ and } \sigma \text{ the mean and standard deviation.} \end{aligned} \tag{4.4}$$

An example output provided by [120] is shown in Figure 4.7, where the micro-relief orientation intensity peaks at 116.1^o and 31.1^o for the vental forearm area of a young woman. This approach was preferred over the bidirectional Gaussian filter because it does not require configuration of parameters to specific hydration levels. In order to confirm the basic performance of this implementation, the micro-relief orientation intensity in the area of volar forearm between a 15 and a 48 years old volunteers were compared. Figure 4.8a was found to be in agreement with results presented in the literature, where the young subject indicated two peaks with 90^o angle between them. In contrast, Figure 4.8b demonstrates that the older subject has only one main micro-relief line orientation. Moreover, the intensity percentage comparison confirms that the main lines in one orientation, related to Langer's line, intensifies with age, as it is only at 4.85% for the young volunteer against 8.17% for the older volunteer. Please, note that there is a 90^o offset in the presentation scale between Figure 4.7 and Figure 4.8.

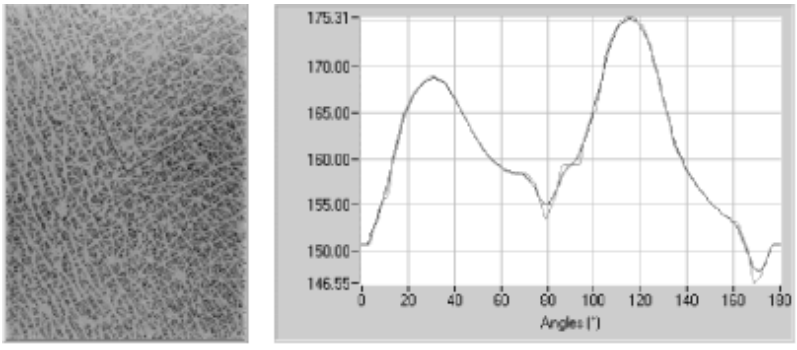

Figure 4.7. (Right) Main directions (31.1^o and 116.1^o) of the micro-relief primary lines of the ventral forearm of a young woman. (Left) Typical plot of the correlation feature vs. the angle (relative to the line perpendicular to the forearm axis). [120]

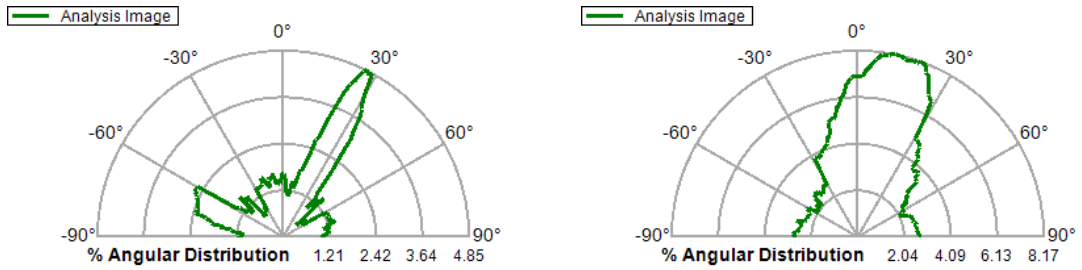

(a) (b)

Figure 4.8. Example of changes in primary and secondary lines with age in volar forearm using the developed algorithm after this was imported in Epsilon E100 suite. Where (a) for a 15y.o. male and (b) for a 48y.o. male.

Combining ε-filter and GLCM

According to Haralick et al. [126], the correlation feature "is a measure of gray-tone linear-dependencies in the image", so the output of this algorithm is affected by all topographic structures of the skin. It indicates the average orientation of all color-tone components in the snapshot, not only the lines, and results to distorted anisotropy index. In order to overcome the above disadvantage, the frames are pre-processed with a dielectric permittivity range filter (ε-filter). More specifically, before applying Equation 4.3, the frame pixels are separated into three groups according to their ε value: ε_{under}, ε_{target} and ε_{over}, where ε_{target} represents the dielectric permittivity of the feature under examination. Figures 4.9 to 4.11 demonstrate use cases in which ε-filter enhances GLCM performance.

Feature Length Estimation

GLCM practically maps the relation between any pixel in the image and its neighbouring pixels. Knowing the dielectric permittivity range values of the target feature, a length estimation of this feature to a given orientation $\theta_{target} \in [0^o\ 180^o)$ can be extracted by the assumption that d approximates averaged feature length in $P(i_{target}, j_{target}, \forall d \in [1, d_{max}], \theta_{target})$ when $\nabla P \approx 0$ (Figure 4.12).

In order to examine the reliability of feature length estimation with capacitive imaging, frames of the same volar forearm skin area (Figure 4.13) were captured with Epsilon E100 and C-Cube [56] (a calibrated digital dermoscope by Pixience, France) and the outputs were compared. While the achieved results have shown very good correlation, the reproducibility is very low because of the skin distortion when the fingerprint sensor is brought in contact. For this reason, only a small sample is presented and this equipment is not recommended for the specific application.

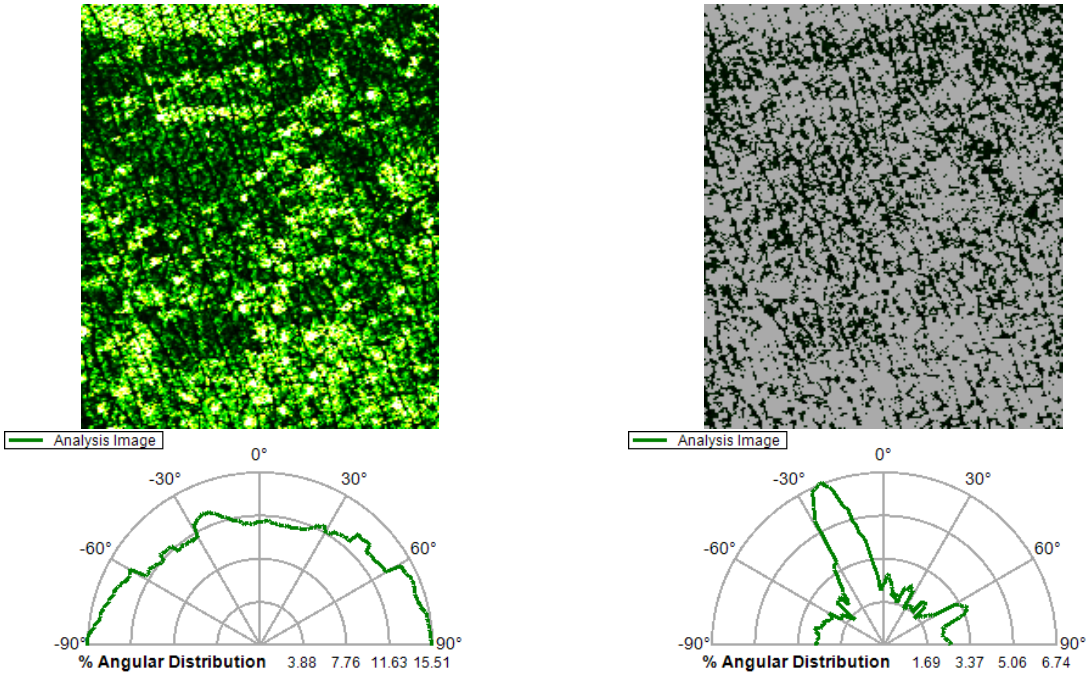

Figure 4.9. Detection of lines with and without ε-filter in abdomen after patch application for 24h. Top left & right the ε-snapshot without and with ε-filter ($\varepsilon_{target} \in [0, 2]$). Bottom left and right the corresponding output of GLCM correlation feature. We notice that the micro-relief lines at -25° are completely shadowed without ε-filter. This happens because the bright marks (damaged skin) have stronger correlation than the lines across all orientations.

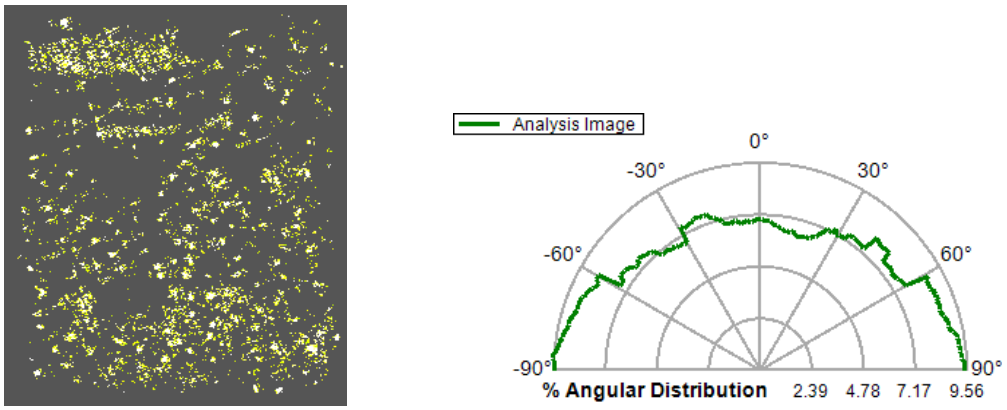

Figure 4.10. Detection of damaged skin by long use of patch in abdomen with ε-filter. Left the ε-snapshot with ε-filter targeting the marks left from the patch ($\varepsilon_{target} \in [50, 85]$). Right the corresponding angular distribution of GLCM correlation feature.

Table 4.1. Results of comparative study between C-Cube spectroscope and Epsilon E100 to examine accuracy of wrinkle length estimation using GLCM. The length of three wrinkles in the area of volar forearm was compared and the correlation between the two measurement methods is calculated to 0.9 [114]. While the presented results show good correlation, the reproducibility is very low because of the skin distortion during the contact image capturing, and this application is not recommended.

Apparatus	**R2**	**R3**	**R4**	R^2
C-Cube [mm]	0.6	0.9	1.1	-
Epsilon E100 [mm]	0.7	0.8	1.0	0.9

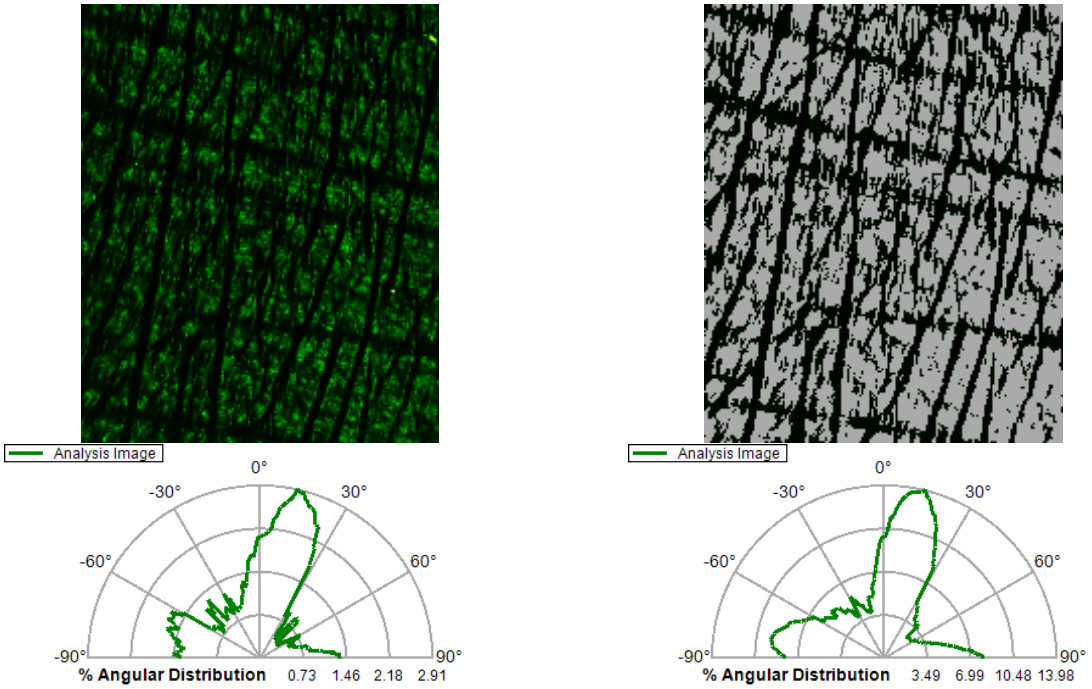

Figure 4.11. Detection of primary and secondary lines with and without ε-filter in thenar eminence site. Top left & right the ε-snapshot without and with ε-filter ($\varepsilon_{target} \in [0, 4]$). Bottom left and right the output of GLCM correlation feature correspondingly.

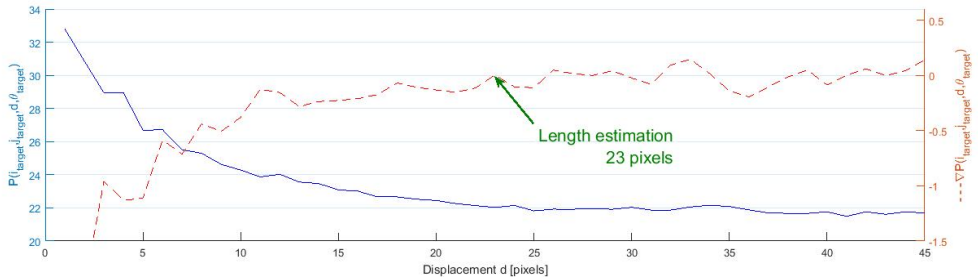

Figure 4.12. Example of feature length estimation when $\nabla P \approxeq 0$.

At this point published work by Liu et al. [127] has to be mentioned, which provides more accurate detection of secondary line micro-relief but immobilizes the ability to measure length. They used the same equation as in Equation 4.3 but they decided to study the area under the GLCM features' curves (e.g. correlation feature in Equation 4.4) for a constant distance range $d \in [1, D]$ per target orientation $\theta_{target} \in [0^o\ 180^o)$. This also improved exponentially the algorithm execution time, since a small distance range d (e.g. 1 to 15) was found sufficient. Their experimental results show that the contrast and correlation features have very strong relation with age [127]. This method can be embedded in the suggested approach by calculating the area S under then curve P of Figure 4.12 (Equation 4.5).

$$S(\theta_{target}) = \sum_{d=1}^{D} P(i_{target}, j_{target}, d, \theta_{target}) \tag{4.5}$$

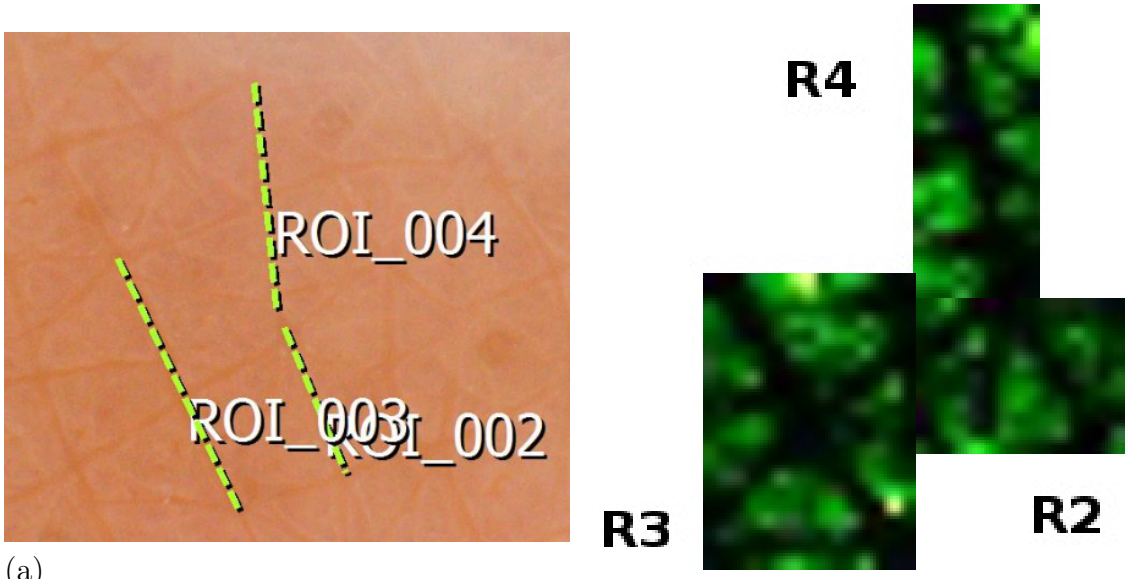

(a) (b)

Figure 4.13. Length measurements comparison between (a) digital dermoscope C-Cube and (b) Epsilon E100. C-Cube measures R2=0.6mm, R3=1.1mm and R4=0.9mm while Epsilon E100 measures R2=0.7mm, R3=1.05mm and R4=0.8mm [114].

Anisotropy Index

The anisotropy index is a way of interpreting the same results but with a single scalar value instead of an angular distribution. Lagarde et al. [128] defined the Anisotropy Index of skin micro-relief angular distribution as: "the level of anisotropy, i.e. the percentage of furrows oriented in a different direction. It is the ratio of the minimal spectral moment of the surface to the maximal spectral moment of the surface. The higher this level, the greater the anisotropy of the surface, i.e. the less the furrows are uniformly oriented in all directions.". Zahouani et al. [115] provided the equation to calculate this quantity, based on autocorrelation, using Equation 4.6.

$$AI = 0.5\frac{\sum_{i=0}^{N-1}|R_i - S/N|}{S - S/N}100$$
$$Where\ S = \sum_{i=0}^{N-1} R_i, \tag{4.6}$$

R_i *the angular distribution values and N samples total from 0 to* π.

The latter group also produced experimental results, demonstrating correlation between the anisotropy index and age in 120 Caucasian women (Figure 4.14).

4.3 Skin Grids Counting

Trojahn et al. [117] expressed the importance of automatic grid area counting after finding -0.65 correlation between $grids/mm^2$ in volar forearm and chronological

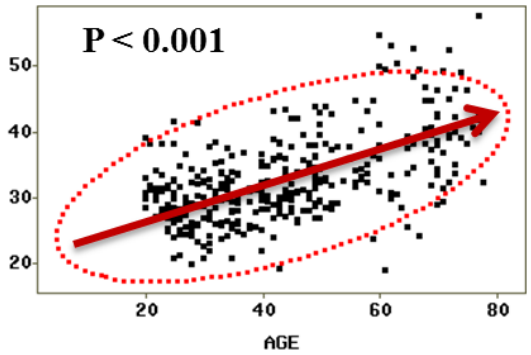

Figure 4.14. Anisotropy index against age for 120 Caucasian women [115]. It should be noted that while the p-value indicates good statistical significance, it might also be misleading since there are a lot of points on the top left which are higher than the bottom right. As a result, one might reach completely different correlation with a smaller dataset.

age. At the same time, they strengthened the reliability of automatic grids counting algorithm by [116], which is based on Matlab software (MathWorks, Natick, MA, USA) and also gives correlation -0.64 between age and $\mathrm{grids/mm^2}$. Unfortunately, Gao's approach [116] involves morphological opening and closing which cannot be performed on capacitive images. The combination of image resolution and skin non-uniformity makes the filter application impossible. The morphological window will either be very wide and hide micro-relief components or small enough to be ineffective. The key required segmentation algorithm features for its efficient application on skin capacitive images with $50\mu\mathrm{m}$ resolutions are:

- The focus on skin grids only
- The suppression of furrows between skin grids until they become width-less
- The auto-discovery of superpixels within skin polygons
- The support of non-uniform superpixels in size or shape.

According to [129] segmentation algorithms are separated in two main categories, the graph and gradient-based segmentation. The graph-based algorithms calculate a weight for each pair of neighbouring pixels and finds the superpixels by minimizing a cost function. Figure 4.15 illustrates the output of a graph-based algorithm [130]. This group is not appropriate for skin grid detection because it creates grids within skin furrow.

The gradient-based algorithms conditionally select initial pixels and extend them into superpixels using ascent gradient methods. Out of the algorithms in literature, Vincent and Soille [131] was proven the best fit for our application. They start to ascent from local minima pixels until catchment basins are filled and watersheds, i.e. width-less lines, are formed in-between (Figure 4.16). The only modification required to fit the dielectric permittivity images of Epsilon E100, was to start from

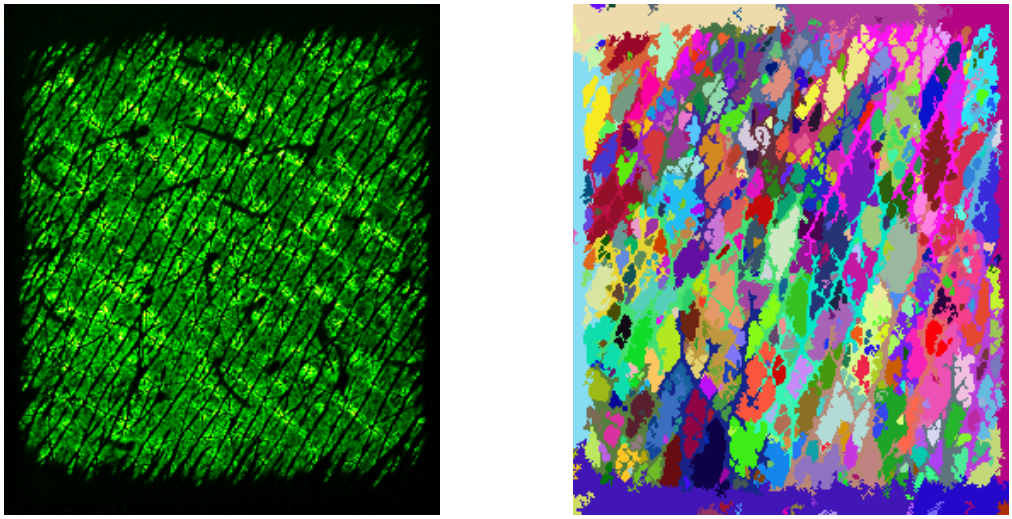

(a) (b)

Figure 4.15. Demonstration of graph-based segmentation [130] for volar forearm area of 48y.o. male volunteer. (a) the ε-snapshot and (b) the segmented output [114].

local maxima, pixels with high ε value that represent skin, and use descent gradient method so that the algorithm suppresses furrows between skin polygons. Figure 4.17 illustrates how this approach performs on ε images. Note that the skin grids expand to completely suppress furrow, which is represented by blue lines. Also, the watersheds overlap in the middle of the furrows, confirming the superpixel uniformity.

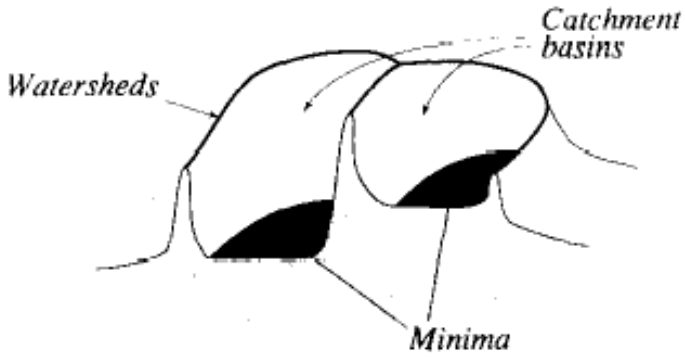

Figure 4.16. Visualisation of Vincent & Soille [131] immersion process analogy watersheds segmentation.

4.4 Corner Density & Intersections

Corner density and intersections are defined by counting the line crossings after application of threshold and thinning process, such as the Zhang and Suen algorithm [132], on the skin hydration map [120]. Major drawback of this technique is that the threshold value is not a universal constant, because there is great difference in hydration levels between skin sites and volunteers. Also, the thinning algorithms

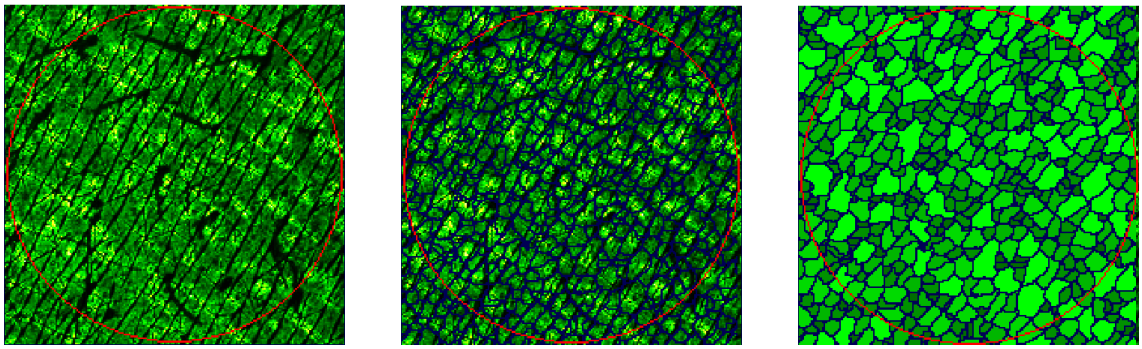

Figure 4.17. Application of Vincent & Soille segmentation algorithm on ε-snapshot in the area of volar forearm from 48y.o. volunteer. From left to right, the original ε-filter, the grid borders and the grid (superpixel) coloured labels.

themselves do not guarantee 'perfect' pixel-width lines, adding a random percentage of error on the results. Figure 4.18 demonstrates how the number of intersections and output quality shift with small changes in threshold value. The corner density and number of intersections can be calculated with more accuracy using the segmentation algorithm presented in Figure 4.17 rather than a thinning process.

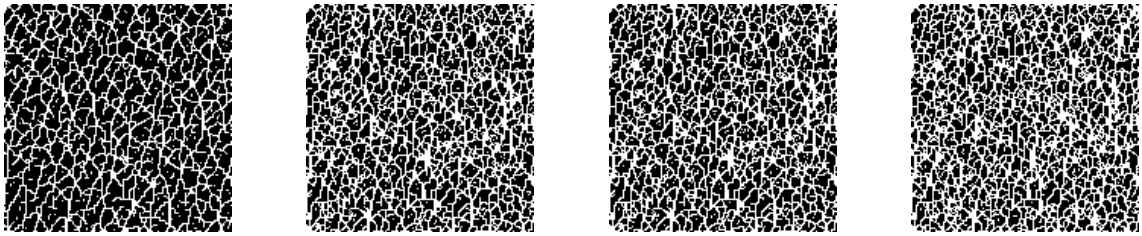

Figure 4.18. Vulnerability of threshold in thinning process for calculation of line density and intersections. We note the significant output offset with small shift in threshold value. From left to right ε-filter threshold changes from 1 to 4 with constant step.

4.5 Algorithm Testing

This section exposes vulnerabilities that were observed during development as well as evaluation of performance. The first experiment was conducted in order to specify measurement errors in micro-relief orientation, intensity and length estimation against the angle of the probe when capturing the skin frame. For this purpose a capacitive image with distinct micro-relief orientation was selected. In order to exclude human error, only one image was used and this was rotated digitally with 10^o angular step before being fed into the suggested algorithm. The normalised peak micro-relief magnitude and angular shift per frame step rotation are presented in Figure 4.19. The micro-relief intensity errors was measured as $\pm 8.4\%$, while $\pm 7.2\%$ error was detected in the length estimation algorithm. Furthermore, Figure 4.19b shows errors in the micro-relief orientation detection when the frame is rotated,

mainly close to the original image alignment with y-axis. The latter indicates that possible root cause of these errors is that the GLCM offset vectors derive from line digitalization in windows as small as 12-by-12pixels while the implementation does not anticipate for sinusoidal function errors.

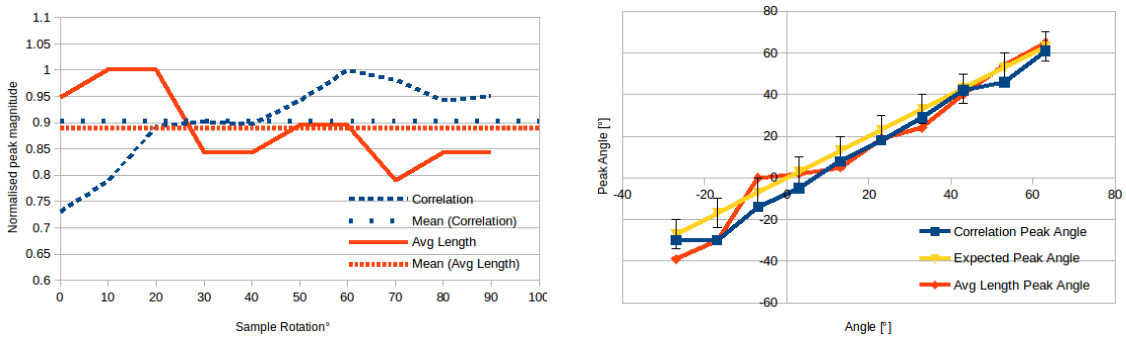

(a) (b)

Figure 4.19. Comparison between GLCM correlation feature with and without ε-filter. (a) The normalised peak magnitude and (b) the peak angle over different snapshot angles.

Next, the segmentation algorithm reproducibility was examined. For this experiment five volunteers were asked to acclimatise five different body sites for 20 minutes in $21°C$ and $45-55\%RH$. The selected sites were palm, cheek, calf, abdomen and upper arm. For each of these sites and for each volunteer, five non-overlapping capacitive images were recorded with Epsilon E100. Given the snapshots have been taken for neighbouring skin areas per site, the number of skin polygons per surface area is not expected to vary drastically and thus indicate the reproducibility of the algorithm results.

The corner density, grid density and intersections mean and standard deviation of all subjects for each site can been seen in Figure 4.20a-c. Based on these results, it is concluded that the suggested segmentation algorithm performs satisfactorily with an expected error of less than 13%, given that no skin artefacts are present in the skin capture (e.g. hair, scars, surface water etc.). Also, a slight underperformance is observed when measuring the corner density and intersections, still with expected error below 15%..

The same dataset is also presented per person and per body site in Figure 4.21a. It would be expected that less hydrated skin sites with thicker stratum corneum layers would have a smaller ratio of grids per surface area, so no solid conclusions can be drawn from this data interpretation. Cause of this might be the mixed gender volunteers that affect the reading, e.g. by rougher cheek skin in male subjects. The averaged grid density for these sites has been also plotted against the chronological age of the subjects (Figure 4.21b). Again, no solid conclusion can be drawn, but without implying any errors in the algorithms since no such correlation was found in the literature for any of these sites and for mixed gender studies.

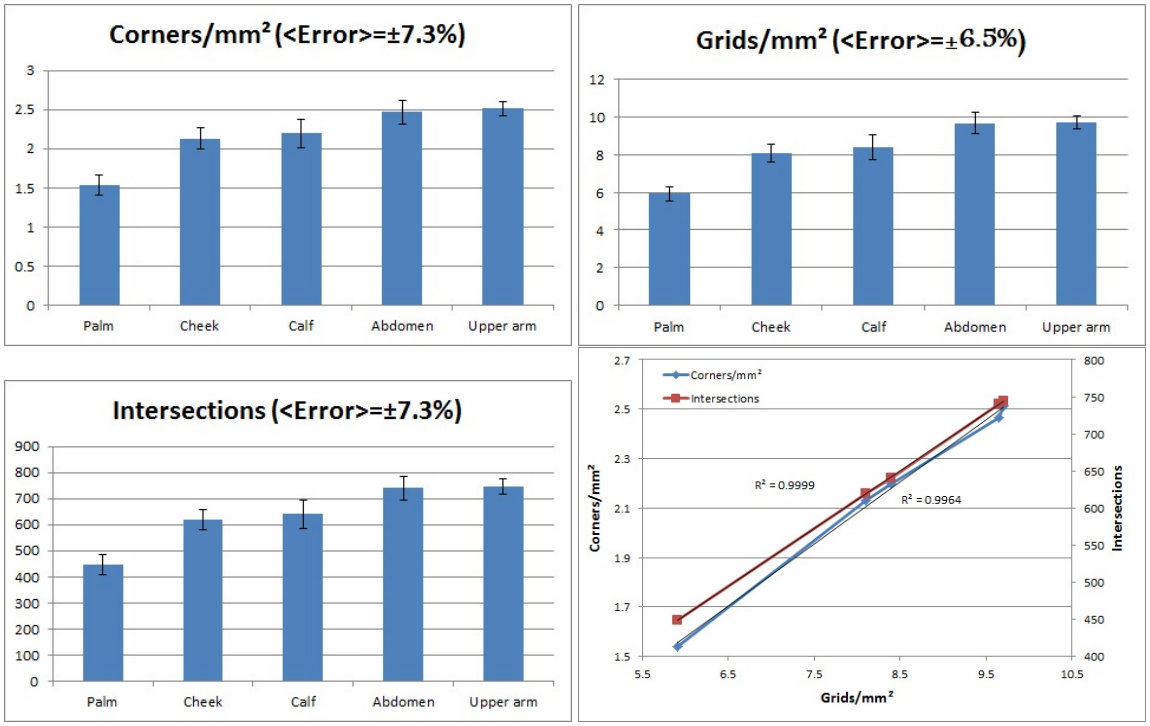

Figure 4.20. Mutli-subject and skin site experiment to determine reliability of segmentation derivative parameters. (a) corners density, (b) grids density, (c) number of intersections and (d) correlation between them.

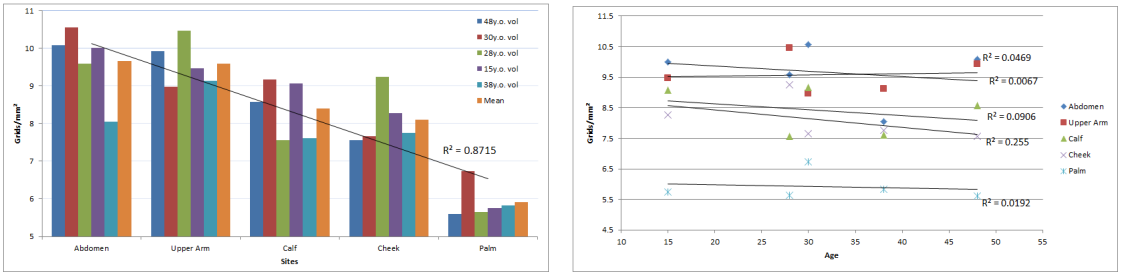

Figure 4.21. Experimental measurement of grids/mm^2 (a) against different skin site and (b) against subject's chronological age.

Last, a vulnerability of the suggested segmentation algorithm was demonstrated through a skin over-hydration experiment. Whilst the suggested gradient-based algorithm does not require calibration of universal variables, it still cannot cope with edge skin conditions that will cause over- or under-segmentation. In this experiment, the grid density of the middle volar forearm was measured before and every ten minutes from the moment over-hydration was introduced (event at moment zero). One would expect that when soaking the skin, due to water absorption, the polygons enlarge resulting to smaller number of polygons per surface area. But the experimental results in Figure 4.22 demonstrate the opposite trend. This is because skin absorbs water in a very inhomogeneous way which appears to the segmentation algorithm as creating multiple catchment basins within the same enclosed polygon, subsequently resulting to over-segmentation. This is an extreme case, but it underlines the im-

portance of proper skin acclimatisation before conducting an experiment.

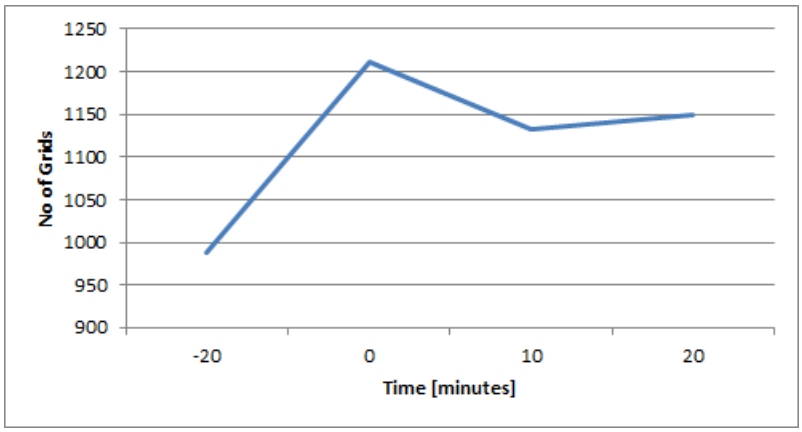

Figure 4.22. Segmentation algorithm fault after skin over-hydration (Time -20mins before and 0mins right after over-hydration).

4.6 Experimental Results

The evaluation of the algorithms has provided important information, but the implementation still has to be tested for its tentative merits against the existing literature via comparison of experimental results. For this purpose, capacitive images from the middle volar forearm of 12 volunteers in different age groups were recorded in two different elbow positions, 90° and 180°, after acclimatisation while the palm was in resting position. These snapshots were used in order to calculate (a) the sum of the absolute intensity change in primary and secondary lines (whenever detectable) during arm extension, (b) the anisotropy index and (c) the skin polygon density at 90° elbow resting position. The achieved results are presented in Figures 4.23-4.25 respectively. Figure 4.23 provides solid evidence that the suggested algorithm meets the criteria required in skin research, since it demonstrates how younger subjects buffer strain between primary and secondary lines during arm extension resulting to a low sum of absolute magnitude changes. The anisotropy index results do not match the previous analysis, although they are based on the same algorithm output for line intensity detection. But, as it is noted in Figure 4.14, a larger dataset is required to achieve statistically significant results. Last, the investigation of skin polygons per surface area comes in agreement with the literature, where [116] and [117] have calculated it around -0.65 and in this work it was found to be -0.7.

4.7 Optimisation, Tools & Techniques

Algorithm optimisation, as always in general programming, comes down to optimum utilisation of the CPU and memory. All the software tasks running on a computer

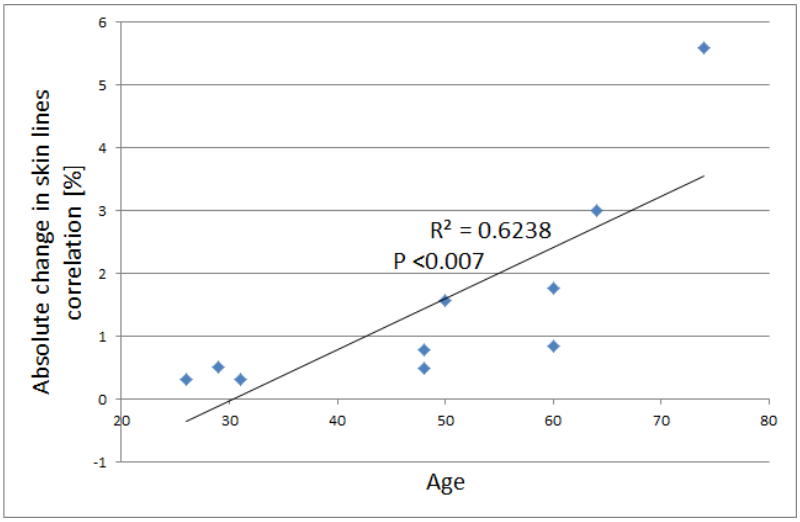

Figure 4.23. Total skin lines correlation change during arm extension against chronological age [133].

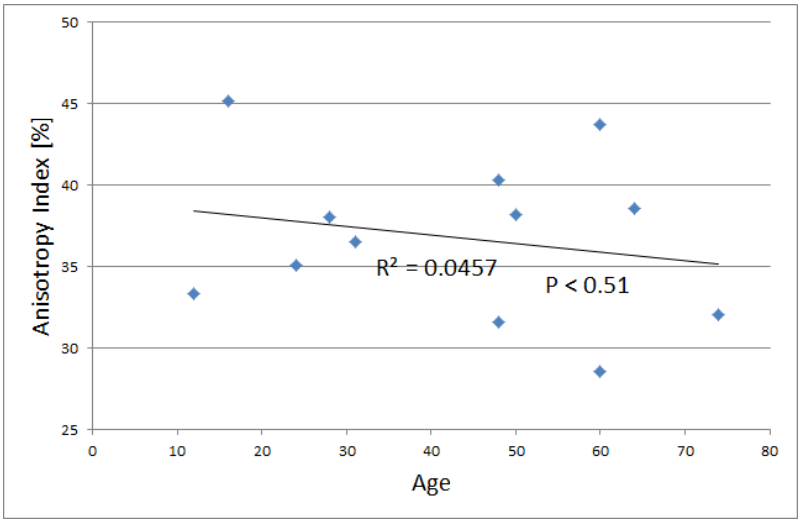

Figure 4.24. Anisotropy index against chronological age [133].

any given time, whether as hidden Daemon or user interface applications, continuously demand both of these components in order to execute. The rules of sharing each CPU core is straight-forward, only one process is executed at any given time and the OS scheduler decides when and for how long, with time defined in OS scheduler quanta based on the system clock. In the case of memory, things are more complicated. Multiple tasks can read simultaneously from the same memory (or cache) but when a process writes new data to a memory location this has to be inaccessible for any other task. Of course, all operating systems provide functions to regulate memory access, i.e. semaphores, mutexes and IPC (Inter-Process Communication), but the fastest and safest approach is always the one that completely avoids conflicts in shared memory regions. In this section, we will explain the optimum algorithmic solution from a programmer's point of view in order to boost execution time of all algorithms described in this chapter.

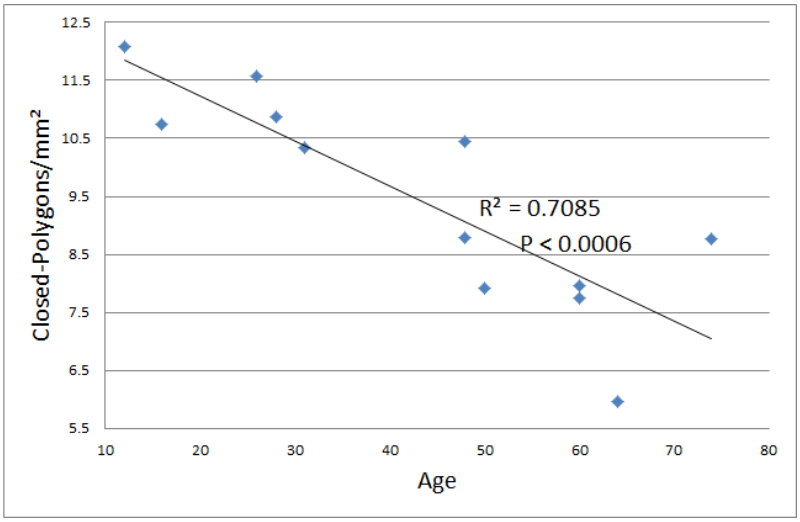

Figure 4.25. Average number of closed polygons per surface area against chronological age [133].

The modern CPUs have multiple cores, so we compile our algorithms in C++11 that provides multi-threading and portability (compatible with Windows, Linux and Mac). The creation of multiple threads increases the execution speed since all CPU cores are utilised. Our implementation detects the available cores in the CPU and ensures that at least equal number of tasks are created to solve each equation. So, if four cores are available our algorithm brakes the work-load in four tasks and each of our equations is performed up to 4 times faster. Unfortunately, the sequence and execution moment of each task is not deterministic. The operating system uses the same cores to perform hundreds of other tasks, from updating the screen and scanning peripheral devices to running the scheduler who decides which task will take the resources next. In order to avoid memory clash during indeterministic thread execution time, we split the equation calculations based on the output array. This means that the subtasks may read from the shared memory (the input array or image), but they never attempt to write in the same memory location, making needless the use of inter-task communication tools. This approach also ensures that no thread is placed in waiting state until others release locked memory locations, ensuring stability in execution time.

Another 'trick' to improve timing performance lies on the architecture of memory design at lower level. First, memory locations in hardware are always addressed in series. Although we index each dimension of an array separately, to make programmer's life easier, the information is always stored in one,or more, single-dimension arrays. So, when we store a 2D array, such as in image, in memory we store each row of the array sequentially, i.e. each pixel has distance one from horizontal and distance equal to the array width from vertical neighbouring pixels. Second, the main memory space is long in order to serve as many concurrent applications as

possible, which creates a trade between manufacturing cost and data access speed. Solution to this trade is given with the use of cache memories between the main memory and the consumer CPU. These are more expensive, faster and smaller storage areas that improve access speed by holding a copy of the most commonly used variables and their neighbouring data. Combining these two concepts, we realise that the execution speed is many times faster when we read the pixels of an image in rows than in columns, because the horizontal neighbouring pixels will be found in cache (cache hit) whilst the vertical ones will have to be retrieved from the main memory (cache miss). This technique halves execution time.

'Valgrind' framework is proven very useful throughout this project because it allows to measure execution speed, it counts time spent per line of code and also detects memory leaks.

4.8 Summary

This chapter focused on the texture analysis of skin surface using the capacitive imaging system Epsilon E100 in order to create new system applications via a different interpretation of the hydration maps. Through a literature review in this area, it was identified that the extraction of micro-relief orientation and intensity, the automatic skin polygons count as well as the corner density and number of intersections would be appreciated by the users of this technology.

In order to detect the micro-relief orientation and intensity, two major approaches were found in the literature, adopted and evaluated. The first one is based on a rotating bidirectional Gaussian filter which was found to perform well, while at the same time producing a wrinkles enhanced image. Unfortunately, this could not cope with the various hydration levels and inhomogeneity of skin micro-relief between body sites and subjects without a dedicated algorithm calibration per frame. Also, the intensity of the relief orientation is provided in arbitrary units, depending on the algorithm calibration, and as a result unreliable for comparative studies. The second approach is based on the correlation feature of the GLCM after the image normalisation. This was found to cope satisfactorily independently of the body site or skin hydration levels. Furthermore, different analysis of the GLCM allows the extraction of more information about the skin texture, such as the line wrinkle length estimation that was presenting in this chapter.

The segmentation algorithms are widely used in image processing, but the challenge in capacitive imaging applications was that the fingerprint sensor resolution is low in contrast to the highly inhomogeneous skin surface. Research groups that use high resolution imaging system were able to detect the skin polygons with the application of morphological opening and closing or graph-based segmentation. These

approaches were tested on skin capacitive images but unfortunately the results were suffering from over or undersegmentation. Finally, the gradient-based segmentation by Vincent and Soille was found to be ideal for our purpose. Furthermore, the corner density and number of intersections became derivatives of the algorithm output by a simple matrix scan.

Finally, the validity of the algorithm implementations was determined by a set of software tests before they were evaluated by case study experiments. The results of these experiments came in agreement with the literature, thus strengthening the use of capacitive imaging systems in the analysis of skin micro-relief alongside hydration.

Chapter 5

Conclusions and Future Work

5.1 Conclusions

The importance of evolving the capacitive imaging technology into a multi-purpose, affordable and portable scientific instrument for closing an existing gap in the skin research laboratory equipment has been stressed throughout this work. In a first step, the theoretical physics background of the electric based measurement principle as well as the analysis of the human skin as measurand were presented and further utilised in software simulations to evaluate the suitability of capacitive arrays in skin hydration measurements. The comparative simulation output against established single sensor hydration probes showed that fingerprint sensors have the potential of outperforming the current user expectations by achieving better measurement penetration depth and sensitivity.

After the reliability of the measurement principle was theoretically validated, methodologies for converting greyscale biometrics images of arbitrary units into false colour dielectric permittivity maps were presented. These involved pixel equalisation to linear dielectric response across the apparatus array on hardware level, as well as units conversion from voltage levels to capacitance and dielectric permittivity. From that point on, without underestimating the existing application of this technology for sample inspection via visualisation, data interpretation methodologies and image processing algorithms were developed and presented. In order to strengthen the selected methodologies, multiple experiments were conducted. These demonstrated the successful dielectric response linearisation and improved pixel homogeneity as well as measurement reliability and reproducibility close to this of single sensor probes. At the same time, the experiments highlighted a set of new technology applications including, calculation of stratum corneum hydration percentage, isolation of skin regions, skin barrier damage characterisation, solvent permeability measurements and water desorption measurements from human appendages.

The above mentioned methodologies and experimental applications fulfilled the

research aim of this work by mainly utilising the bioelectric properties of the sample. In Chapter 4, methodologies were presented to further expand the laboratory applications of this equipment by studying the human skin texture using only the false colour feedback of the system, essentially by automating and enhancing the visual inspection of the sample with advanced image processing algorithms. The outcome of that chapter was the detection of skin micro-relief orientation and intensity as well as the automatic skin grid count per surface area. All of these parameters play important role in pharmaceutical and cosmetic industries, since they are indicative of the human skin aging process, and for their determination high resolution dermatoscopes with sophisticated and expensive software have to be employed. Furthermore, alternative data interpretation was suggested in order to measure feature length or track progress of superficial skin damage.

All in all, it is believed that the main research objectives of this work have been achieved, with their methodologies clearly presented and their implementations evaluated with experimental results. Furthermore, the majority of the suggested work has been already commercialised by Biox System Ltd. and is being stringently tested in laboratories across the world since 2018. However, there is still space for improvements since throughout this study vulnerabilities of the capacitive imaging technology have been exposed, which should be addressed in the future in order to gain further trust from the skin research community.

5.2 Future Work

Real-time Temperature-based Correction

During the evaluation of the capacitive imaging sensor, the effect of environmental conditions in the results was experimentally studied (Figure 3.18-3.21). Currently, there is no evidence that the sensor temperature is taken into account during the calibration of the instrument or during a measurement capture, since no such sensor is embedded. The preferred solution to this problem could be to ensure that the temperature of the sensor surface does not exceed this of the room conditions, in order to avoid changing the acclimatisation status of the sample - whether in-vivo or in-vitro. At a second stage, real time temperature and humidity data have to be recorded alongside the capacitive frames in order to apply corrections on the false coloured output, taking into account the temperature dependence of the dielectric permittivity. The latter will enable consistent readouts when the acclimatisation protocols are not strict, or impossible because of the nature of an experiment.

Sorption Measurements

In Chapter 3, water sorption measurements on hair and nail samples were investigated. While it was concluded that the achieved dataset trends are in accordance to findings in the literature, the desorption rate was affected by the in-vitro plastic plug. The sample need to be in firm contact with the sensor surface in order to be measured, but at the same time it has to be exposed to the room/chamber conditions in order to control its acclimatisation status efficiently while the sensor provides feedback on its thermodynamic equilibrium. In order to reliably replicate the functionality of a DVS instrument using a capacitive array, an in-vitro sample holder has to be developed that holds the sample firmly against the sensor surface without blocking the sample interaction with the environment conditions. Such equipment would strengthen in-vitro sorption applications using the capacitive imaging probes. Furthermore, the existing ability of Epsilon E100 to record false colour videos could enable the visualisation of sample's sorption mechanisms, creating a new set of possible applications.

Hydration Profiling

A capacitive imaging probe has certain advantages over high accuracy laboratory equipment for hydration measurements such as the OTTER and the Confocal Raman Spectroscopy. It is more affordable and it is a hand-held instrument that can capture hydration measurements in-vivo from almost any body site. At the same time, the capacitive imaging technology at its current development stage for skin research has a crucial conceptual disadvantage, it cannot separate between displacement and hydration level i.e. lack of profiling. The manufactures of electric-based hydration probes solve this problem using a spring loaded measurement head that ensures the minimum required force against the sample. This is more of a temporary solution, because drift in spring force over long term use could result to drifts in the readouts.

A more permanent solution, that could at the same time enable a low resolution hydration profiling, would be the use of multiple sensing electrodes in different geometries and displacements in reference to the pixel driving electrode. This will result to multiple readouts per pixel for a variety of measurement depths in the same skin area and virtually at the same instance using techniques such as time division multiple access. Such development could increase the standards in capacitive imaging for skin measurements and it would be of great interest to study in the future. Of course, multiple scientific and engineering challenges have to be faced, including the further technology minutarization and noise vulnerability, the development of high resolution sampling electronics, and the increased complexity of the electro-

static models to account for changes in the electric field strength against distance in samples with undefined multi-layered structure.

Bibliography

[1] Biox Systems Ltd, "Biox Epsilon Model E100 Specifications," https://www.biox.biz/Products/Epsilon/E100PSpecs.php, accessed: 2019-6-1.

[2] G. K. Johnsen, "Skin electrical properties and physical aspects of hydration of keratinized tissues," Ph.D. dissertation, University of Oslo, Jun. 2010.

[3] iStock - Paladjai, "Vol.2 Structure of the skin info graphics illustration vector on white background," https://www.istockphoto.com/vector/vol-2-structure-of-the-skin-info-graphics-illustration-vector-on-white-background-gm953892302-260419264?clarity=false, accessed: 20-08-08.

[4] Rice University, *Anatomy and Physiology*. Creative Commons Attribution 4.0 International License, ch. 5.1 Layers of the Skin, accessed: 2020-07-25.

[5] merkelcell.org, "What is a Merkel cell?" https://merkelcell.org/about-mcc/what-is-a-merkel-cell/, accessed: 2020-07-25.

[6] Wikimedia Foundation, Inc, "Langerhans cell," https://en.wikipedia.org/wiki/Langerhans_cell, accessed: 2020-07-25.

[7] BiologyOnline, "Stratum lucidum," https://www.biologyonline.com/dictionary/stratum-lucidum, accessed: 2020-07-25.

[8] D. Mohammed, P. J. Matts, J. Hadgraft, and M. E. Lane, "Variation of stratum corneum biophysical and molecular properties with anatomic site," *The AAPS Journal*, vol. 14, pp. 806–812, 2012.

[9] Z. Ya-Xian, T. Suetake, and H. Tagami, "Number of cell layers of the stratum corneum in normal skin - relationship to the anatomical location on the body, age, sex and physical parameters," *Arch Dermatol Res*, vol. 291, pp. 555–559, 1999.

[10] A. Ishida-Yamamoto and S. Igawa, "The biology and regulation of corneodesmosomes," *Cell and tissue research*, vol. 360, no. 3, pp. 477–482, 2015.

[11] G. K. Menon, G. W. Cleary, and M. E. Lane, "The structure and function of the stratum corneum," *International journal of pharmaceutics*, vol. 435, no. 1, pp. 3–9, 2012.

[12] H. J. Cha, C. He, H. Zhao, Y. Dong, I.-S. An, and S. An, "Intercellular and intracellular functions of ceramides and their metabolites in skin (review)," *International Journal of Molecular Medicine*, vol. 38, pp. 16–22, 2016.

[13] A. V. Rawlings and P. J. Matts, "Stratum corneum moisturization at the molecular level: An update in relation to the dry skin cycle," *Journal of Investigative Dermatology*, vol. 124, pp. 1099–1110, 2005.

[14] J. A. Bouwstra, A. de Graaff, G. S. Gooris, J. Nijsse, J. W. Wiechers, and A. C. van Aelst, "Water distribution and related morphology in human stratum corneum at different hydration levels," *Journal of Investigative Dermatology*, vol. 120, pp. 750–758, 2003.

[15] R. R. Warner, K. J. Stone, and Y. L. Boissy, "Hydration disrupts human stratum corneum ultrastructure," *Journal of Investigative Dermatology*, vol. 120, pp. 275–284, 2003.

[16] A. Bevilacqua, A. Gherardi, and R. Guerrieri, "In vivo quantitative evaluation of skin aging by capacitance image analysis," in *Proc. of the IEEE International Workshop on Applications of Computer Vision (WACV), Colorado, USA*, vol. 1. IEEE Computer Society, 2005, pp. 342–347. [Online]. Available: http://www.scopus.com/inward/record.url?eid=2-s2.0-33846942571&partnerID=tZOtx3y1

[17] B. Isik, M. S. Gurel, A. T. Erdemir, and O. Kesmezacar, "Development of skin aging scale by using dermoscopy," *Skin Research and Technology*, vol. 19, no. 2, pp. 69–74, 2013. [Online]. Available: http://onlinelibrary.wiley.com/doi/10.1111/srt.12033/full

[18] C. Trojahn, G. Dobos, M. Schario, L. Ludriksone, U. Blume-Peytavi, and J. Kottner, "Relation between skin micro-topography, roughness, and skin age," *Skin Res. Technol.*, vol. 21, no. 1, pp. 69–75, Feb. 2015.

[19] H. Zahouani, M. Djaghloul, R. Vargiolu, S. Mezghani, and M. E. L. Mansori, "Contribution of human skin topography to the characterization of dynamic skin tension during senescence: morpho-mechanical approach," *Journal of Physics: Conference Series*, vol. 483, 2014.

[20] J.-M. Sainthillier, S. Mac-Mary, and P. Humbert, "Analysis of skin relief," pp. 177–189, 2017.

[21] W. Manuskiatti, D. A. Schwindt, and H. I. Maibach, "Influence of age, anatomic site and race on skin roughness and scaliness," *Dermatology*, vol. 196, pp. 401–407, 1998.

[22] V. Korn, C. Surber, and G. Imanidis, "Skin surface topography and texture analysis of sun-exposed body sites in view of sunscreen application," *Skin Pharmacology and Physiology*, vol. 29, pp. 291–299, 2016.

[23] C. Bontozoglou, X. Zhang, A. Patel, M. E. Lane, and P. Xiao, "In vivo human hair hydration measurements by using Opto-Thermal radiometry," *Int. J. Thermophys.*, vol. 40, no. 2, p. 22, Feb. 2019.

[24] X. J. Wang, R. P. Dhond, W. V. Sorin, J. S. Nelson, S. A. Newton, and T. E. Milner, "Characterization of human scalp hairs by optical low-coherence reflectometry," *Optics Letters*, vol. 20, no. 6, p. 524, 1995.

[25] M. R. Harkey, "Anatomy and physiology of hair," *Forensic Science International*, vol. 63, pp. 9–18, 1993.

[26] D. V. NESTE, "Thickness, medullation and growth rate of female scalp hair are subject to significant variation according to pigmentation and scalp location during ageing," *European Journal of Dermatology*, vol. 14, no. 1, pp. 28–32, 2004.

[27] B. Buffoli, F. Rinaldi, M. Labanca, E. Sorbellini, A. Trink, E. Guanziroli, R. Rezzani, and L. F. Rodella, "The human hair: from anatomy to physiology," *International Journal of Dermatology*, vol. 53, pp. 331–341, 2014.

[28] N. Otberg, H. Richter, H. Schaefer, U. Blume-Peytavi, W. Sterry, and J. Lademann, "Variations of hair follicle size and distribution in different body sites," *Journal of Investigative Dermatology*, vol. 122, no. 1, pp. 14–19, 2004.

[29] A. C. Wosu, U. Valdimarsdóttir, A. E. Shields, D. R. Williams, and M. A. Williams, "Correlates of cortisol in human hair: implications for epidemiologic studies on health effects of chronic stress," *Ann. Epidemiol.*, vol. 23, no. 12, pp. 797–811.e2, Dec. 2013.

[30] S. K. Kristensen, S. C. Larsen, N. J. Olsen, J. Fahrenkrug, and B. L. Heitmann, "Hair dyeing, hair washing and hair cortisol concentrations among women from the healthy start study," *Psychoneuroendocrinology*, vol. 77, pp. 182–185, Mar. 2017.

[31] A. F. Hamel, J. S. Meyer, E. Henchey, A. M. Dettmer, S. J. Suomi, and M. A. Novak, "Effects of shampoo and water washing on hair cortisol concentrations," *Clinica Chimica Acta*, vol. 412, no. 3-4, pp. 382–385, 2011.

[32] C. Barba, S. Méndez, M. Martí, J. L. Parra, and L. Coderch, "Water content of hair and nails," *Thermochimica Acta*, vol. 494, no. 1-2, pp. 136–140, 2009.

[33] M. S. Boll, K. C. Doty, R. Wickenheiser, and I. K. Lednev, "Differentiation of hair using ATR FT-IR spectroscopy: A statistical classification of dyed and non-dyed hairs," *Forensic Chemistry*, vol. 6, pp. 1–9, 2017.

[34] D. de Berker, "Nail anatomy," *Clinics in Dermatology*, vol. 31, pp. 509–515, 2013.

[35] iStock - Iv__design, "Science of hair. Anatomical training poster. Hair structure. Detailed medical vector illustration stock illustration," accessed: 20-08-30. [Online]. Available: https://www.istockphoto.com/vector/science-of-hair-anatomical-training-poster-hair-structure-detailed-medical-vector-gm926246846-254157288?clarity=false

[36] A. C. Tam and B. Sullivan, "Remote sensing applications of pulsed photothermal radiometry," *Appl. Phys. Lett.*, vol. 43, pp. 333–335, 1983.

[37] R. E. Imhof, D. J. S. Birch, F. R. Thornley, J. R. Gilchrist, and T. A. Strivens, "Optothermal transient emission radiometry," *Journal of Physics E: Scientific Instruments*, vol. 17, no. 6, pp. 521–525, 1984.

[38] X. Zhang, C. Bontozoglou, and P. Xiao, "In vivo skin characterizations by using opto-thermal depth-resolved detection spectra," *Cosmetics*, vol. 6, p. 54, 2019.

[39] C. Raman, "A new radiation," *Indian Journal of Physics*, vol. 2, pp. 387–398, 1928.

[40] Nobel Lectures Physics 1922-1941, Sir Chandrasekhara Venkata Raman. Copyright © The Nobel Foundation 1930. [Online]. Available: https://www.nobelprize.org/prizes/physics/1930/raman/biographical/

[41] E. B. Hanlon, R. Manoharan, T.-W. Koo, K. E. Shafer, J. T. Motz, M. Fitzmaurice, J. R. Kramer, I. Itzkan, R. R. Dasari, and M. S. Feld, "Prospects for in vivo raman spectroscopy," *Physics in medicine and biology*, vol. 45, pp. R1–R59, 2000.

[42] J. A. Koningstein, *Introduction to the Theory of the Raman Effect*. Springer Netherlands, 1972.

[43] P. J. Caspers, H. A. Bruining, G. J. Puppels, G. W. Lucassen, and E. A. Carter, "In vivo confocal raman microspectroscopy of the skin: Noninvasive

determination of molecular concentration profiles," *Journal of Investigative Dermatology*, vol. 116, pp. 434–442, 2001.

[44] P. J. Caspers, G. W. Lucassen, R. Wolthuis, H. A. Bruining, and G. J. Puppels, "In vitro and in vivo raman spectroscopy of human skin," *John Wiley & Sons, Inc. Biospectroscopy*, vol. 4, pp. S31–S39, 1998.

[45] H. Baker and A. M. Kligman, "Measurement of transepidermal water loss by electrical hygrometry. instrumentation and responses to physical and chemical insults," *Arch Dermatol .*, vol. 96, no. 4, pp. 441–452, 1967.

[46] A. Vasti, "The insensible water loss through the skin," *American Journal of Physiology-Legacy Content*, vol. 102, pp. 60–70, 1932.

[47] J. W. H. Mali, "The transport of water through the human epidermis," *Journal of Investigative Dermatology*, vol. 27, pp. 451–469, 1956.

[48] M. Qassem and P. Kyriacou, "Review of modern techniques for the assessment of skin hydration," *Cosmetics*, vol. 6, p. 19, 2019.

[49] R. E. Imhof, M. E. P. D. Jesus, P. Xiao, L. I. Ciortea, and E. P. Berg, "Closed-chamber transepidermal water loss measurement: microclimate, calibration and performance," *International journal of cosmetic science*, vol. 31, pp. 97–118, 2009.

[50] Courage + Khazaka electronic GmbH, "Tewameter® TM 300," https://www.courage-khazaka.de/en/16-wissenschaftliche-produkte/alle-produkte/172-tewameter-e, accessed: 2020-7-19.

[51] C. Driemeier, F. M. Mendes, and M. M. Oliveira, "Dynamic vapor sorption and thermoporometry to probe water in celluloses," *Cellulose*, vol. 19, pp. 1051–1063, 2012.

[52] Surface Measurement Systems Ltd., "Dynamic Vapor Sorption (DVS)," https://www.surfacemeasurementsystems.com/solutions/dynamic_vapor_sorption, accessed: 2020-7-25.

[53] G. K. Johnsen, . G. Martinsen, and S. Grimnes, "Sorption studies of human keratinized tissues," *Journal of Physics: Conference Series*, vol. 224, p. 012094, 2010.

[54] P. Corcuff, O. de Lacharriere, and J. L. Leveque, "Extension-induced changes in the microrelief of the human volar forearm: variations with age." *Journal of gerontology*, vol. 46, no. 6, pp. M223–7, 1991.

[55] Courage+Khazaka electronic GmbH, "Skin-Colorimeter CL 400 ," https://www.courage-khazaka.de/en/scientific-products/all-products/16-wissenschaftliche-produkte/alle-produkte/180-colorimeter-e, accessed: 2020-7-25.

[56] Pixience, "The C-Cube: the new standard for digital dermoscopy," https://www.pixience.com/products/presentation-2/?lang=en, accessed: 2019-6-28.

[57] X. Li, S. Larson, A. Zyuzin, and A. Mamishev, "Design of multichannel fringing electric field sensors for imaging. Part I. General design principles," in *Conference Record of the 2004 IEEE International Symposium on Electrical Insulation*, 2004, pp. 406–409. [Online]. Available: http://ieeexplore.ieee.org/document/1380616/

[58] X. B. Li, C. Kato, A. S. Zyuzin, and A. V. Mamishev, "Design of multichannel fringing electric field sensors for imaging. part ii. numerical examples," in *Conference Record of the 2004 IEEE International Symposium on Electrical Insulation*, 2004, pp. 410–413.

[59] A. Ivorra, "Bioimpedance monitoring for physicians: an overview," *Cent. Nac. Microelectròn. Biomed. Appl. Gr.*, vol. 1, 01 2002.

[60] C. Tronstad, G. K. Johnsen, S. Grimnes, and Ø. G. Martinsen, "A study on electrode gels for skin conductance measurements," *Physiological Measurement*, vol. 31, no. 10, pp. 1395–1410, sep 2010. [Online]. Available: https://doi.org/10.1088%2F0967-3334%2F31%2F10%2F008

[61] J. J. Ackmann and M. A. Seitz, "Methods of complex impedance measurements in biologic tissue." *Critical reviews in biomedical engineering*, vol. 11, no. 4, pp. 281–311, 1984.

[62] Y. Yamamoto and T. Yamamoto, "Characteristics of skin admittance for dry electrodes and the measurement of skin moisturisation," *Medical and Biological Engineering and Computing*, vol. 24, pp. 71–77, 1986.

[63] Ø. G. Martinsen, S. Grimnes, and E. Haug, "Measuring depth depends on frequency in electrical skin impedance measurements," *Skin Research and Technology*, vol. 5, pp. 179–181, 1999.

[64] C. Gabriel, "Compilation of the dielectric properties of body tissues at rf and microwave frequencies." 1996.

[65] S. Grimnes and Ø. Martinsen, *Bioimpedance and bioelectricity basics*. Academic Press, 2008, ch. 4, pp. 105–110.

[66] H. Bauer, "Courage + khazaka electronic, köln - corneometer® CM 825 (e)," https://www.courage-khazaka.de/en/scientific-products/all-products/16-wissenschaftliche-produkte/alle-produkte/183-corneometer-e, accessed: 2019-6-1.

[67] A. O. Barel and P. Clarys, "Skin capacitance," *Non Invasive Diagnostic Techniques in Clinical Dermatology*, pp. 357–366, 2014. [Online]. Available: http://link.springer.com/10.1007/978-3-642-32109-2

[68] Cortex Technology, "Dermalab single," https://cortex.dk/single-parameter-dermalab/, Accessed: 2020-24-04.

[69] "Biox System Ltd." http://www.biox.biz/.

[70] Biox System Ltd., "Epsilon - Hydration imaging," Brochure, 2018. [Online]. Available: https://www.bioxsystems.com/wp-content/uploads/Biox-Epsilon-Brochure-2018-Rev01a.pdf

[71] T. Chen, "Capacitive sensors for measuring complex permittivity of planar and cylindrical structures," Ph.D. dissertation, 2012.

[72] S. Liao, P. Dourmashkin, and J. Belcher, "Course notes: Physics 8.02 Electricity and Magnetism at MIT." [Online]. Available: http://web.mit.edu/viz/EM/visualizations/coursenotes/

[73] H. Hammer, "Analytical model for Comb-Capacitance fringe fields," *J. Microelectromech. Syst.*, vol. 19, no. 1, pp. 175–182, Feb. 2010.

[74] GNU Octave, "Scientific Programming Language," https://www.gnu.org/software/octave.

[75] P. Clarys, R. Clijsen, J. Taeymans, and A. O. Barel, "Hydration measurements of the stratum corneum: Comparison between the capacitance method (digital version of the Corneometer CM 825®) and the impedance method (Skicon-200EX®)," *Skin Research and Technology*, vol. 18, no. 3, pp. 316–323, 2012. [Online]. Available: http://dx.doi.org/10.1111/j.1600-0846.2011.00573.x

[76] J. W. Fluhr, M. Gloor, S. Lazzerini, P. Kleesz, R. Grieshaber, and E. Berardesca, "Comparative study of five instruments measuring stratum corneum hydration (corneometer cm 820 and cm 825, skicon 200, nova dpm 9003, dermalab). part i. in vitro," *Skin Research & Technology*, vol. 5, pp. 161–170, 1999.

[77] R. G. Lorenzini, W. M. Kline, C. C. Wang, R. Ramprasad, and G. A. Sotzing, "The rational design of polyurea & polyurethane dielectric materials," *Polymer*, vol. 54, pp. 3529–3533, 2013.

[78] Scalar Corporation, "Moisture Checker MY-808S," http://www.scalar.co.jp/english/products/my-808s.html, Accessed: 2020-24-04.

[79] X. Ou, W. Pan, and P. Xiao, "In vivo skin capacitive imaging analysis by using grey level co-occurrence matrix (glcm)," *International Journal of Pharmaceutics*, vol. 460, pp. 28–32, 2014.

[80] X. Gao, Y. Zhao, and H. Ma, "Fringing electric field sensors for anti-attack at system-level protection," *Sensors*, vol. 18, no. 9, p. 3034, 2018.

[81] W. Pan, X. Zhang, E. Chirikhina, C. Bontozoglou, and P. Xiao, "Measurement of Skin Hydration with a Permittivity Contact Imaging System," in *SCC Technology Showcase Poster*, 2014.

[82] Slovenian cosmetics, "Koko cosmetics – synergy of goat's milk and CBD oil," Slovenian cosmetics, Apr. 2019. [Online]. Available: https://cosmedoc.si/en/2019/04/18/koko-cosmetics-synergy-of-goats-milk-and-cbd-oil/

[83] G. FRANCK, L. JEAN-LUC, and Q. BERNARD, "Device and method for evaluating the hydration of skin and mucosa," FR Patent EP1 438 922A1, 2004.

[84] H. Bauer, "Courage + khazaka electronic, köln - moisturemap® MM 100 (e)," https://www.courage-khazaka.de/en/scientific-products/efficacy-tests/skin/16-wissenschaftliche-produkte/alle-produkte/167-moisturemap-e.

[85] E. Xhauflaire-Uhoda, C. Piérard-Franchimont, and G. E. Piérard, "Skin capacitance mapping of psoriasis," *Journal of the European Academy of Dermatology and Venereology*, vol. 20, no. 10, pp. 1261–1265, 2006.

[86] E. Xhauflaire-Uhoda and G. E. Piérard, "Skin capacitance imaging of acne lesions," *Skin Res Technol .*, vol. 13, pp. 9–12, 2007.

[87] J.-L. Lévêque, E. Xhauflaire, and G. Pierard, "Skin capacitance imaging, a new technique for investigating the skin surface." *European Journal of Dermatology*, vol. 16, no. 5, pp. 500–6, 2006.

[88] Mathematical treatment of charging and discharging a capacitor, "schoolphysics.co.uk," http://www.schoolphysics.co.uk/age16-19/Electricity%20and%20magnetism/Electrostatics/text/Capacitor_charge_and_discharge_mathematics/index.html, accessed: 2020-08-08.

[89] A. Jabłecka, J. Olszewski, and E. Marzec, "Dielectric properties of keratin–water system in diabetic and healthy human fingernails," *Journal of non-crystalline solids*, vol. 355, no. 50-51, pp. 2456–2460, 2009.

[90] X. Zhang, C. Bontozoglou, E. Chirikhina, M. E. Lane, and P. Xiao, "Capacitive imaging for skin characterizations and solvent penetration measurements," *Cosmetics*, vol. 5(3),52, 2018.

[91] P. Xiao and C. Bontozoglou, "Capacitive contact imaging for in-vivo hair and nail water content measurements," *H & PC*, vol. 10(5), pp. 62–65, 2015.

[92] J. G. M. Logger, C. U. Münchhoff, J. I. Olydam, M. Peppelman, and P. E. J. V. Erp, "Anatomical site variation of water content in human skin measured by the epsilon: A pilot study," *Skin Research and Technology*, vol. 25, pp. 333–338, 2019.

[93] W. Pan, X. Zhang, E. Chirikhina, C. Bontozoglou, and P. Xiao, "Measurement of skin hydration with a permittivity contact imaging system," in *IFSCC Conference Zurich 2015*, Sep. 2015.

[94] M. Egawa, T. Hirao, and M. Takahashi, "In vivo estimation of stratum corneum thickness from water concentration profiles obtained with raman spectroscopy," *Acta dermato-venereologica*, vol. 87, no. 1, pp. 4–8, 2007.

[95] S. W. Smith *et al.*, *The scientist and engineer's guide to digital signal processing*. California Technical Pub. San Diego, 1997, vol. 14, ch. 24, pp. 410–416.

[96] AuthenTec, Inc., *TCS1/TCS2-TCD58E TouchChip Chipset Datasheet*, AuthenTec, Inc., 2011. [Online]. Available: http://m.sztlink.com/uploads/201809/5b91de4db2eee.pdf

[97] F. C. AB, *Fingerprints FPC1080A Swipe Sensor*. [Online]. Available: https://www.fingerprints.com/technology/hardware/sensors/fpc1080a

[98] *Embedded Module SFC160S-D*, STARTEK Engineering Inc., 3F, 54 Park Ave. II, Science-Based Industrial Park Hsinchu 300, Taiwan, R.O.C. [Online]. Available: http://www.startek-eng.com/products_more.aspx?category_id=16&id=346

[99] *Fingerprints FPC1020 Touch Sensor*, Fingerprint Cards AB, Kungsgatan 20, SE-411 19 Gothenburg, Sweden. [Online]. Available: https://www.fingerprints.com/technology/hardware/sensors/fpc1020/

[100] R. Elkeeb, X. Hui, H. Chan, L. Tian, and H. I. Maibach, "Correlation of transepidermal water loss with skin barrier propertiesin vitro: comparison of three evaporimeters," *Skin Research and Technology*, vol. 16, pp. 9–15, 2010.

[101] D. Voegeli, "The effect of washing and drying practices on skin barrier function," *J Wound Ostomy Continence Nurs.*, vol. 35, pp. 84–90, 2008.

[102] I. Buraczewska, B. Berne, M. Lindberg, H. Törmä, and M. Lodén, "Changes in skin barrier function following long-term treatment with moisturizers, a randomized controlled trial," *British Journal of Dermatology*, vol. 156, pp. 492–498, 2007.

[103] W. Pan, X. Zhang, M. Lane, and P. Xiao, "The occlusion effects in capacitive contact imaging for in vivo skin damage assessments," *International Journal of Cosmetic Science*, vol. 37, pp. 395–400, Aug. 2015.

[104] J. Snatchfold and D. Targett, "Exploratory study to evaluate two clinical methods for assessing moisturizing effect on skin barrier repair," *Skin Res Technol*, vol. 25, pp. 251–257, 2019.

[105] F. Kartono and H. I. Maibach, "Irritants in combination with a synergistic or additive effect on the skin response: an overview of tandem irritation studies," *Contact Dermatitis*, vol. 54, pp. 303–312, 2006.

[106] S. G. Danby, K. Brown, A. M. Wigley, J. Chittock, P. K. Pyae, C. Flohr, and M. J. Cork, "The effect of water hardness on surfactant deposition after washing and subsequent skin irritation in atopic dermatitis patients and healthy control subjects," *Journal of Investigative Dermatology*, vol. 138, no. 1, pp. 68–77, 2018.

[107] A. Ezerskaia, S. F. Pereira, H. P. Urbach, and B. Varghese, "Quantification of changes in skin hydration and sebum after tape stripping using infrared spectroscopy," in *Proc. SPIE 10037, Photonics in Dermatology and Plastic Surgery*, 2017.

[108] D. Horita, H. Todo, and K. Sugibayashi, "Effect of ethanol pretreatment on skin permeation of drugs," *Biol. Pharm. Bull.*, vol. 35, pp. 1343–1348, 2012.

[109] J. W. Fluhr, R. Darlenski, and C. Surber, "Glycerol and the skin: holistic approach to its origin and functions," *British Journal of Dermatology*, vol. 159, pp. 23–34, 2008.

[110] S. A. Saghir, M. J. Bartels, and W. M. Snellings, "Dermal penetration of ethylene glycol through human skin in vitro," *International Journal of Toxicology*, vol. 29, pp. 268–276, 2010.

[111] Sensirion, "SHT3x (RH/T) - digital humidity sensor — sensirion," https://www.sensirion.com/en/environmental-sensors/humidity-sensors/digital-humidity-sensors-for-various-applications, accessed: 2019-5-31.

[112] C. Piérard-Franchimont and G. E. Piérard, "Hair weathering and hair capacitance mapping: a pilot study," *Journal of Cosmetic Dermatology*, vol. 11, pp. 179–182, 2012.

[113] P. Xiao, L. I. Ciortea, C. Bontozoglou, and R. E. Imhof, "Hair water content & water holding capacity measurements," in *7th International Conference on Applied Hair Science*, 2016.

[114] C. Bontozoglou and P. Xiao, "Applications of capacitive imaging in human skin texture and hair analysis," *Applied Sciences*, vol. 10, no. 1, p. 256, 2020.

[115] H. Zahouani, M. Djaghloul, R. Vargiolu, S. Mezghani, and M. E. L. Mansori, "Contribution of human skin topography to the characterization of dynamic skin tension during senescence: morpho-mechanical approach," *Journal of Physics: Conference Series*, vol. 483, p. 012012, 2014. [Online]. Available: http://stacks.iop.org/1742-6596/483/i=1/a=012012?key=crossref.c80365706ff0c5975affafd05cd8636e

[116] Q. Gao, J. Yu, F. Wang, T. Ge, L. Hu, and Y. Liu, "Automatic measurement of skin textures of the dorsal hand in evaluating skin aging," *Skin Research and Technology*, vol. 19, no. 2, pp. 145–151, 2013. [Online]. Available: http://onlinelibrary.wiley.com/doi/10.1111/srt.12025/full

[117] C. Trojahn, G. Dobos, M. Schario, L. Ludriksone, U. Blume-Peytavi, and J. Kottner, "Relation between skin micro-topography, roughness, and skin age," *Skin Research and Technology*, vol. 21, no. 1, pp. 69–75, 2015.

[118] K. Tsukahara, O. Osanai, T. Kitahara, and Y. Takema, "Seasonal and annual variation in the intensity of facial wrinkles," *Skin Research and Technology*, vol. 19, no. 3, pp. 279–287, 2013.

[119] E. Kim, G. Cho, N. G. Won, and J. Chos, "Age-related changes in skin biomechanical properties: The neck skin compared with the cheek and forearm skin in Korean females," *Skin Research and Technology*, vol. 19, no. 3, pp. 236–241, 2013.

[120] J. L. Leveque and B. Querleux, "SkinChipR, a new tool for investigating the skin surface in vivo," *Skin Research and Technology*, vol. 9, no. 4, pp. 343–347, nov 2003. [Online]. Available: http://doi.wiley.com/10.1034/j.1600-0846.2003.00043.x

[121] A. Bevilacqua and A. Gherardi, "Age-related skin analysis by capacitance images," in *Proceedings of the 17th International Conference on Pattern Recognition, 2004. ICPR 2004.*, vol. 2, 2004, pp. 703–706.

[122] A. Bevilacqua and A. Gherardi, "Characterization of a capacitive imaging system for skin surface analysis," in *2008 1st International Workshops on Image Processing Theory, Tools and Applications, IPTA 2008.* IEEE, 2008, pp. 1–7. [Online]. Available: http://ieeexplore.ieee.org/xpls/abs{_}all.jsp?arnumber=4743777

[123] K. Hashimoto, "New Methods for Surface Ultrastructure: Comparative Studies of Scanning Electron Microscopy, Transmission Electron Microscopy and Replica Method," *International Journal of Dermatology*, vol. 13, no. 6, pp. 357–381, nov 1974. [Online]. Available: http://doi.wiley.com/10.1111/j.1365-4362.1974.tb05068.x

[124] X. Ou, W. Pan, and P. Xiao, "In vivo skin capacitive imaging analysis by using grey level co-occurrence matrix (GLCM)," *International Journal of Pharmaceutics*, vol. 460, no. 1-2, pp. 28–32, 2014.

[125] F. Bianconi, E. Chirikhina, F. Smeraldi, C. Bontozoglou, and P. Xiao, "Personal identification based on skin texture features from the forearm and multimodal imaging," *Skin Research and Technology*, vol. 23, no. 3, pp. 392–398, 2017.

[126] R. M. Haralick, K. Shanmugam, and I. Dinstein, "Textural Features for Image Classification," *IEEE Transactions on Systems, Man, and Cybernetics*, vol. SMC-3, no. 6, pp. 610–621, nov 1973. [Online]. Available: http://ieeexplore.ieee.org/document/4309314/

[127] J. H. Liu, C. U. Wang, G. Qian, K. Yang, and Z. K. Chen, "Research and implementation for texture of handback skin quantitative analysis based on co-occurrence matrix," in *2009 International Conference on Industrial Mechatronics and Automation, ICIMA 2009*, 2009, pp. 158–161.

[128] J. M. Lagarde, C. Rouvrais, and D. Black, "Topography and anisotropy of the skin surface with ageing," *Skin Research and Technology*, vol. 11, no. 2, pp. 110–119, 2005.

[129] R. Achanta, A. Shaji, K. Smith, A. Lucchi, P. Fua, and S. Süsstrunk, "SLIC superpixels compared to state-of-the-art superpixel methods," *IEEE Transactions on Pattern Analysis and Machine Intelligence*, vol. 34, no. 11, pp. 2274–2281, 2012.

[130] P. F. Felzenszwalb and D. P. Huttenlocher, "Efficient graph-based image segmentation," *International Journal of Computer Vision*, vol. 59, no. 2, pp. 167–181, 2004.

[131] L. Vincent and P. Soille, "Watersheds in Digital Spaces: An Efficient Algorithm Based on Immersion Simulations," *IEEE Transactions on Pattern Analysis and Machine Intelligence*, vol. 13, no. 6, pp. 583–598, 1991.

[132] T. Y. Zhang and C. Y. Suen, "A Fast Parallel Algorithm for Thinning Digital Patterns," *Commun. ACM*, vol. 27, no. 3, pp. 236–239, mar 1984. [Online]. Available: http://doi.acm.org/10.1145/357994.358023

[133] C. Bontozoglou, X. Zhang, and P. Xiao, "Micro-relief analysis with skin capacitive imaging," *Skin Res. Technol.*, vol. 25, no. 2, pp. 165–170, Mar. 2019.

Appendix A

Appendix

A.1 Extension of Equation 2.3

Equations are available on various textbooks, here the [72] textbook is consider as reference of all equations in this Appendix subsection.

Charge: q

Coulomb force:

$$\overrightarrow{F}_e = k_e \cdot \frac{Qq}{r^2} \cdot \hat{r} \tag{A.1}$$

Electric field:

$$\overrightarrow{E} = \frac{\overrightarrow{F}_e}{q} \rightarrow d\overrightarrow{E} = k_e \cdot \frac{dq}{r^2} \tag{A.2}$$

Potential energy charge:

$$dU = -\int_A^B \overrightarrow{F}_e \, d\overrightarrow{s} \tag{A.3}$$

Energy potential:

$$dV = -\int_A^B \overrightarrow{E} \, d\overrightarrow{s} \tag{A.4}$$

When infinity as reference to zero potential:

$$dV = k_e \cdot \frac{dq}{r} \tag{A.5}$$

For a source Q:

$$V = k_e \cdot \frac{Q}{r} \tag{A.6}$$

Where:

$k_e = \frac{1}{4\pi\epsilon_0}$

Assuming the interdigital sensor geometry in Figure A.1, Equation A.5 converts to Equation A.7.

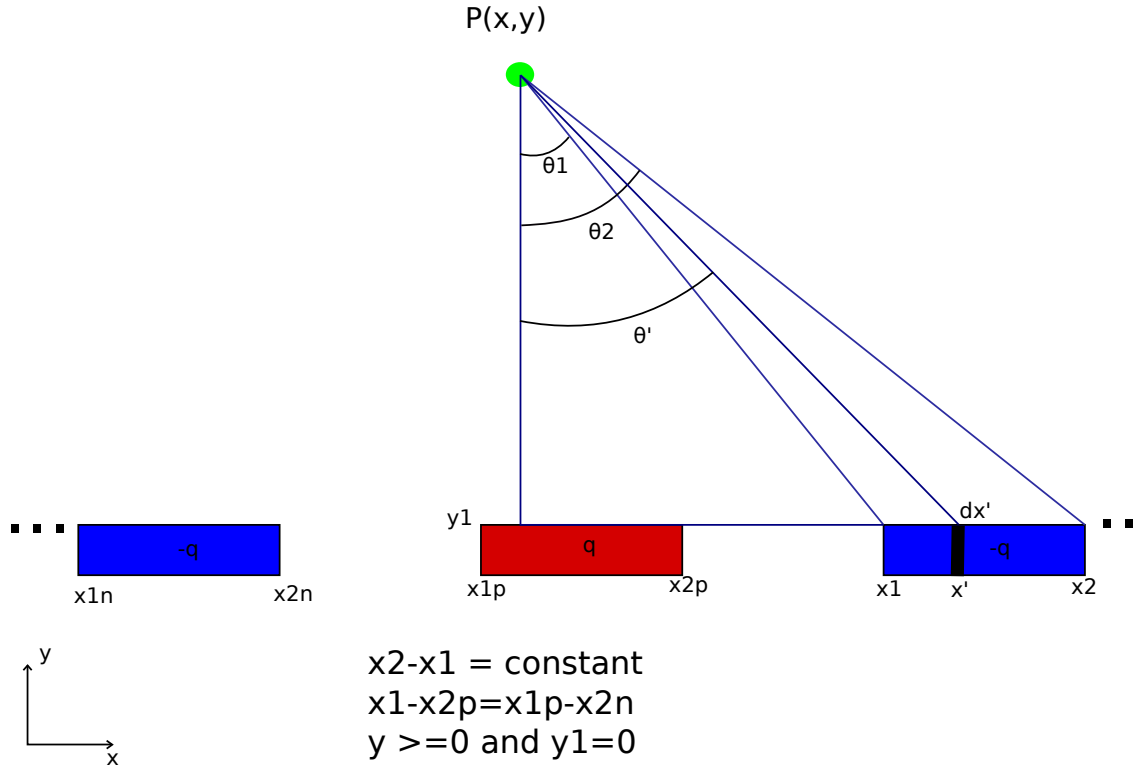

Figure A.1. Target model to solve

$$(A.5) \rightarrow dV = k_e \cdot \frac{\lambda\, dx'}{\sqrt{x'^2 + y^2}} \implies$$

$$V = k_e\lambda \cdot \int_{x_1}^{x_2} \frac{1}{\sqrt{x'^2 + y^2}}\, dx' = \lambda k_e \cdot (\sinh^{-1}\frac{x_2}{y} - \sinh^{-1}\frac{x_1}{y}) \tag{A.7}$$

Where: $\lambda dx' = dq$

Correspondingly, the electric field is calculated as in:

$$(A.2) \rightarrow d\overrightarrow{E} = k_e\lambda \cdot \frac{dx'}{x'^2 + y^2} \tag{A.8}$$

While its y and x components are calculated in Equation A.9 and Equation A.10:

$$dE_y = d\overrightarrow{E} \cdot \cos\theta' \implies E_y = k_e\lambda \cdot \int_{x_1}^{x_2} \frac{1}{\sqrt{(x'^2 + y^2)^2}} \cdot \frac{y}{(x'^2 + y^2)^{1/2}}\, dx' =$$

$$= k_e\lambda y \cdot \int_{x_1}^{x_2} \frac{1}{(x'^2 + y^2)^{3/2}}\, dx', x' = y\tan\theta \rightarrow dx' = y\sec^2\theta' d\theta' =$$

$$= k_e\lambda y \cdot \int_{\theta_1}^{\theta_2} \frac{y\sec^2\theta'}{(y^2\tan^2\theta' + y^2)^{3/2}}\, d\theta' = k_e\lambda y \cdot \int_{\theta_1}^{\theta_2} \frac{y\sec^2\theta'}{y^3(\tan^2\theta' + 1)^{3/2}}\, d\theta' = \frac{k_e\lambda}{y} \cdot \int_{\theta_1}^{\theta_2} \frac{\sec^2\theta'}{(\tan^2\theta' + 1)^{3/2}}$$

$$= \frac{k_e\lambda}{y} \cdot \int_{\theta_1}^{\theta_2} \frac{\sec^2\theta'}{\sec^3\theta'}\, d\theta' = \frac{k_e\lambda}{y} \cdot \int_{\theta_1}^{\theta_2} \cos\theta'\, d\theta' \implies$$

$$\implies E_y = \frac{k_e\lambda}{y} \cdot (\sin\theta_2 - \sin\theta_1) \tag{A.9}$$

$$dE_x = d\overrightarrow{E} \cdot \sin\theta' \implies E_x = k_e\lambda \cdot \int_{x_1}^{x_2} \frac{1}{\sqrt{(x'^2+y^2)^2}} \cdot \frac{x'}{(x'^2+y^2)^{1/2}}\, dx' =$$

$$= k_e\lambda \cdot \int_{x_1}^{x_2} \frac{x'}{(x'^2+y^2)^{3/2}}\, dx', x' = y\tan\theta \rightarrow dx' = y\sec^2\theta' d\theta' =$$

$$= k_e\lambda \cdot \int_{\theta_1}^{\theta_2} \frac{y^2\tan\theta'\sec^2\theta'}{(y^2\tan^2\theta'+y^2)^{3/2}}\, d\theta' = k_e\lambda \cdot \int_{\theta_1}^{\theta_2} \frac{\tan\theta'\sec^2\theta'}{y(\tan^2\theta'+1)^{3/2}}\, d\theta' =$$

$$= \frac{k_e\lambda}{y} \cdot \int_{\theta_1}^{\theta_2} \frac{\tan\theta'\sec^2\theta'}{sec^3\theta'}\, d\theta' = \frac{k_e\lambda}{y} \cdot \int_{\theta_1}^{\theta_2} \tan\theta' cos\theta'\, d\theta' \implies$$

$$\implies E_x = -\frac{k_e\lambda}{y} \cdot (\cos\theta_2 - \cos\theta_1) \tag{A.10}$$

In order to verify the electric field and electric potential calculations, $E_y = -\frac{\partial V}{\partial y}$ is solved and compared with Equation A.9.
Using equation A.7:

$$E_y = -\frac{\partial V}{\partial y} = -k_e\lambda \cdot \frac{\partial}{\partial y}(sinh^{-1}\frac{x_2}{y} - sinh^{-1}\frac{x_1}{y}) =$$

$$= -k_e\lambda \cdot (-\frac{x_2}{y^2\sqrt{\frac{x_2^2}{y^2}+1}} + \frac{x_1}{y^2\sqrt{\frac{x_1^2}{y^2}+1}}) = k_e\lambda\frac{1}{y^2} \cdot (\frac{yx_2}{\sqrt{y^2}\sqrt{\frac{x_2^2}{y^2}+1}} - \frac{yx_1}{\sqrt{y^2}\sqrt{\frac{x_1^2}{y^2}+1}})$$

$$= k_e\lambda\frac{1}{y} \cdot (\frac{x_2}{\sqrt{x_2^2+y^2}} - \frac{x_1}{\sqrt{x_1^2+y^2}}) = \frac{k_e\lambda}{y} \cdot (\sin\theta_2 - \sin\theta_1)$$

A.2 Electrostatic-based Model for Interdigital and Annular Electrode Geometries

```
'''Maxwell-based electrostatic model for
   specific electrode geometries

Author: Christos Bontozoglou (cbontoz@gmail.com)
Date: 28 Jun 2020

'''

import csv
import logging
import argparse
import math
import matplotlib.pyplot as plt

# Vacuum dielectric permittivity
```

```
e0 = 8.8541878128e-12

# Minimum possible displacement from electrode surface
# Zero is mathematically undefined for the interdigital geometry
mindis = 0.15e-6

# Rob electrode class
class robElectrode:
        # x,y top left corner, dx right, dy downwards
        def __init__(self, x, y, dx, dy, V, id):
                self.id = id
                self.x = float(x)
                self.y = float(y)
                self.dx = float(dx)
                self.dy = float(dy)
                self.cx = float(x + (dx/2))
                self.cy = float(y - (dy/2))
                self.V = float(V)

        # Displacement gain G
        def gainG(self, x, y):
                return math.asinh((self.x + self.dx - float(x)) / \
                abs(float(y))) - math.asinh((self.x - float(x))/abs(float(y)))

        # Calculate potential at a given point x, y
        def potential(self, x, y, chargeDensity):
                return (chargeDensity / (4.0 * math.pi * e0)) * \
                                self.gainG(float(x), float(y))

        # Calculate Ex component at a given point x, y
        def Ex(self, x, y, chargeDensity):
                return (chargeDensity / (4.0 * math.pi * e0 * y)) * \
                ( math.cos(math.atan((self.x + self.dx - \
                        float(x)) / abs(float(y)))) - \
                math.cos(math.atan((self.x - float(x)) / abs(float(y)))) );

        # Calculate Ey component at a given point x, y
        def Ey(self, x, y, chargeDensity):
                return (chargeDensity / (4.0 * math.pi * e0 * y)) * \
                ( math.sin(math.atan((self.x + self.dx - \
                        float(x)) / abs(float(y)))) - \
                math.sin(math.atan((self.x - float(x)) / abs(float(y)))) );

# Annular electrode class
class annularElectrode:
        # centre is always at 0,0
        def __init__(self, InnerRadius, OuterRadius, V, chargeDensity, id):
                self.id = id
                self.rin = float(InnerRadius)
                self.rout = float(OuterRadius)
                self.V = float(V)
                self.S = math.pi * ( self.rout**2 - self.rin**2)
                self.dRadius = self.rout - self.rin;
                self.cd = chargeDensity;

        # Depends on overall geometry, so needs to be set after init
        def setChargeDensity(self, chargeDensity):
                self.cd = chargeDensity

        # Electric potential of annular electrode at given z displacement
```

```
        def potential(self, z):
                return (self.cd / (2.0 * e0)) * \
                (math.sqrt(self.rout**2 + float(z)**2) - \
                math.sqrt(self.rin**2 + float(z)**2))

        # Ez
        def Ez(self, z):
                return -(self.cd / (2.0 * e0)) * \
                ((float(z)/math.sqrt(self.rout**2 + float(z)**2)) - \
                (float(z)/math.sqrt(self.rin**2 + float(z)**2)))

# Interdigital sensor class
class interdigitalSensor:
        def __init__(self, pnum, wavelength, width, height, Vpeak):
                self.pnum = pnum
                self.nnum = pnum
                self.wavelength = float(wavelength)
                self.width = float(width)
                self.Vp = float(Vpeak)
                self.Vn = -self.Vp
                self.electrodes = []
                for i in range(self.pnum + self.nnum):
                        self.electrodes.append(robElectrode(i*(wavelength/2.0),
                                        0.0, width, height,
                                        (self.Vn if ((i%2) == 0) else self.Vp), i))
                self.sigma0 = self.chargeDensity(1)
                self.f, self.ax = plt.subplots(1)

        # Positive electrode charge density
        def chargeDensity(self, epsilon):
                cElectrode = int(math.floor(self.pnum + self.nnum)/2)
                cx = self.electrodes[cElectrode].cx
                cy = mindis - mindis/3
                G = 0
                for el in self.electrodes:
                        if el.V > 0:
                                G += el.gainG(cx, cy)
                        else:
                                G -= el.gainG(cx, cy)
                G /= (4.0 * math.pi * e0 * float(epsilon))
                logging.debug('sigma {}'.format(self.Vp / G))
                return -self.Vp / G

        # Calculate electric potential at point x, y
        def potential(self, x, y, epsilon):
                self.ax.plot(x, y, 'go')
                pot = 0.0
                for el in self.electrodes:
                        if el.V > 0:
                                pot += el.potential(x, y, self.sigma0);
                        else:
                                pot += el.potential(x, y, -self.sigma0);
                pot /= float(epsilon)
                return pot

        # Calculate electric field at point x, y
        def electricField(self, x, y, epsilon):
                self.ax.plot(x, y, 'go')
                Ex = 0.0
                Ey = 0.0
```

```
                for el in self.electrodes:
                        if el.V > 0:
                                Ex += el.Ex(x, y, self.sigma0);
                                Ey += el.Ey(x, y, self.sigma0);
                        else:
                                Ex += el.Ex(x, y, -self.sigma0);
                                Ey += el.Ey(x, y, -self.sigma0);
                Ex /= float(epsilon)
                Ey /= float(epsilon)
                return Ex, Ey

        # Draw the sensor electrodes
        def drawSensor(self):
                for el in self.electrodes:
                        self.ax.plot([el.x, el.x+el.dx, el.x+el.dx, el.x, el.x],
                                        [el.y, el.y, el.y-el.dy, el.y-el.dy, el.y],
                                        'b—' if (el.V < 0) else 'r')

        # Export csv
        def exportCsv(self, Vres, Ex, Ey, disp, csvFilename):
                with open(csvFilename, 'wb') as fout:
                        fwriter = csv.writer(fout, delimiter=',', quotechar='"',
                                        quoting=csv.QUOTE_MINIMAL)
                for i,_ in enumerate(disp):
                        fwriter.writerow([disp[i] ,  Vres[i], Ex[i], Ey[i]])


# Analysis on vertical or horizontal linear segment
def linearSegmentAnalysis(self, xStart, yStart, distance, steps, isHorizontal, epsilon):
        Vres = []
        disp = []
        Ex = []
        Ey = []
        res = float(distance) / float(steps)
        if isHorizontal == True:
        for i in range(int(steps)):
        Vres.append(self.potential(xStart + float(i)*res, yStart, epsilon))
        ex, ey = self.electricField(xStart + float(i)*res, yStart, epsilon)
        Ex.append(ex)
        Ey.append(ey)
        disp.append(xStart + float(i)*res)
        else:
        for i in range(int(steps)):
        Vres.append(self.potential(xStart, yStart + float(i)*res, epsilon))
        ex, ey = self.electricField(xStart, yStart + float(i)*res, epsilon)
        Ex.append(ex)
        Ey.append(ey)
        disp.append(yStart + float(i)*res)
        return Vres, Ex, Ey, disp

class annularSensor:
        def __init__(self, electrodes):
                self.electrodes = electrodes

        def potential(self, z, epsilon):
                pot = 0.0
                for el in self.electrodes:
                        pot += el.potential(z);
                pot /= float(epsilon)
                return pot
```

```
        def electricField(self, z, epsilon):
                E = 0.0
                for el in self.electrodes:
                        E += el.Ez(z);
                E /= float(epsilon)
                return E

        # Analysis on vertical linear segment
        def linearSegmentAnalysis(self, distance, steps, epsilon):
                Vres = []
                disp = []
                E = []
                res = float(distance) / float(steps)
                for i in range(int(steps)):
                Vres.append(self.potential(float(i)*res, epsilon))
                E.append(self.electricField(float(i)*res, epsilon))
                disp.append(float(i)*res)
                return Vres, E, disp

# Thesis data presentation
def thesisPresentation(sensor, name, ydisplacement, pLayer, plotPotential=True):
        ctrElec = sensor.pnum + (1 if (sensor.pnum % 2 == 0) else 0);
        cx = sensor.electrodes[ctrElec].cx
        eps = [1.0, 4.0, 7.0]
        if not plotPotential:
        eps[:] = []
        eps.append(4.0)
        f, ax = plt.subplots(1)
        lineStyles = ['—', '-.', ':']
        for inx, e in enumerate(eps):
                Vy, Ex, Ey, locy = sensor.linearSegmentAnalysis(cx, mindis,
                                ydisplacement, 50.0, False, eps[inx]);
                locy = [x / 1e-6 for x in locy]
                Ex = [x / 1e6 for x in Ex]
                Ey = [x / 1e6 for x in Ey]
                if plotPotential:
                ax.plot(locy, Vy, lineStyles[inx],
                        label = u'\u03B5' + '={}'.format(eps[inx]))
                else:
                ax.plot(locy, Ey, lineStyles[inx],
                        label = u'\u03B5' + '={}'.format(eps[inx]))

        if plotPotential:
                g3 = [0]*len(locy)
                g3 = [1.8*0.03 for x in locy]
                ax.plot(locy, g3, '-', label = u'\u03B3' + '3%␣threshold')
        else:
                pl = [0]*len(locy)
                lploc = [0]*50
                if (pLayer > 0.0):
                pl = [float(i) * 0.6 / 50.0 for i in range(50)]
                lploc = [pLayer/1e-6 for i in range(50)]
                ax.plot(lploc, pl, '-', linewidth=5, label='Protective␣layer')

        ax.legend()
        if plotPotential:
        plt.ylabel('Potential␣[V]')
        plt.xlabel('y␣Displacement␣[' + u'\u03BC' +'m]')
        plt.title(name + '␣measurement␣depth')
```

```
        else:
        plt.ylabel('Electric Field [V/' + u'\u03BC' + 'm]')
        plt.xlabel('y Displacement [' + u'\u03BC' +'m]')
        plt.title(name + ' Ey Component')

def thesisPresentationA(sensor, name, zDisplacement, pLayer, plotPotential=True):
        eps = [1.0, 4.0, 7.0]
        if not plotPotential:
                eps[:] = []
                eps.append(4.0)
        f, ax = plt.subplots(1)
        lineStyles = ['—', '-.', ':']
        for inx, e in enumerate(eps):
                V, Ez, locy = sensor.linearSegmentAnalysis(zDisplacement,
                        50.0, eps[inx]);
                locy = [z / 1e-6 for z in locy]
                Ez = [z / 1e6 for z in Ez]
                if plotPotential:
                ax.plot(locy, V, lineStyles[inx],
                        label = u'\u03B5' + '={}'.format(eps[inx]))
                else:
                ax.plot(locy, Ez, lineStyles[inx],
                        label = u'\u03B5' + '={}'.format(eps[inx]))

        if plotPotential:
                g3 = [0]*len(locy)
                g3 = [1.8*0.03 for x in locy]
                ax.plot(locy, g3, '-', label = u'\u03B3' + '3% threshold')
        else:
                pl = [0]*len(locy)
                lploc = [0]*50
                if (pLayer > 0.0):
                        pl = [float(i) * 0.08 / 50.0 for i in range(50)]
                        lploc = [pLayer/1e-6 for i in range(50)]
                        ax.plot(lploc, pl, '-', linewidth=5,
                                label='Protective layer')

        ax.legend()
        if plotPotential:
                plt.ylabel('Potential [V]')
                plt.xlabel('y Displacement [' + u'\u03BC' +'m]')
                plt.title(name + ' measurement depth')
        else:
                plt.ylabel('Electric Field [V/' + u'\u03BC' + 'm]')
                plt.xlabel('y Displacement [' + u'\u03BC' +'m]')
                plt.title(name + ' Ey Component')

# Epsilon E100
def E100():
        # need to constuct electrodes manually and calculate charge density
        electrodes = []
        electrodes.append(annularElectrode(0.0001e-9, 3.0e-6,
                        1.8, 0, 0))
        electrodes.append(annularElectrode(13.0e-6, 44.0e-6,
                        -1.8, 0, 1))
        electrodes[0].setChargeDensity(2.0 * e0 * electrodes[0].V / \
                        (electrodes[0].dRadius - \
                        (electrodes[1].dRadius * \
                        (electrodes[0].S/electrodes[1].S))))
        electrodes[1].setChargeDensity(-electrodes[0].cd * \
```

```
                    (electrodes[0].S/electrodes[1].S))

        e100 = annularSensor(electrodes)
        logging.debug('Charge density: {} {}'.format(electrodes[0].cd,
                    electrodes[1].cd))
        thesisPresentationA(e100, 'Epsilon E100', 30e-6, 2.0e-6, True)

# Cortex probe (Cortex Technologies)
def Cortex():
        # need to constuct electrodes manually and calculate charge density
        electrodes = []
        electrodes.append(annularElectrode(0.75e-3, 3.1e-3, -1.8, 0, 0))
        electrodes.append(annularElectrode(3.9e-3, 7.8e-3, 1.8, 0, 1))
        electrodes.append(annularElectrode(8.6e-3, 12.7e-3, -1.8, 0, 2))

        sigma = -1.8 / ((((electrodes[0].S+electrodes[2].S)* \
        electrodes[1].dRadius)/ \
        (2.0*e0*electrodes[1].S)) - (electrodes[0].dRadius/(2.0*e0)) - \
        (electrodes[2].dRadius/(2.0*e0)))

        electrodes[0].setChargeDensity(sigma)
        electrodes[2].setChargeDensity(sigma)
        electrodes[1].setChargeDensity(-sigma * \
                    (electrodes[0].S+electrodes[2].S) / electrodes[1].S)
        logging.debug('Charge density: {} {}'.format(electrodes[0].cd,
                    electrodes[1].cd))

        cortex = annularSensor(electrodes)
        thesisPresentationA(cortex, 'Cortex', 50e-3, 0, True)

# Just use the exact same sensor geometry with Hanno Hammer publication
def MaxwellVsHammer():
        # Number of electrodes / 2
        elnum = 20
        # Implement interdigital sensor geometry
        hammer = interdigitalSensor(elnum, 8.0e-6, 2.0e-6, 1.0e-6, 1.8)
        hammer.drawSensor()
        calcy = 0.1e-6
        cx = hammer.electrodes[elnum + (1 if (elnum % 2 == 0) else 0)].cx
        Vy, Ex, Ey, locy = hammer.linearSegmentAnalysis(cx, calcy,
                    10.0e-6, 32.0, False, 1)
        Vy2, Ex2, Ey2, locy2 = hammer.linearSegmentAnalysis(cx - (2e-6),
                    calcy, 4e-6, 32.0, True, 1)
        # Correct against distance scale m -> um
        locy = [x / 1e-6 for x in locy]
        locy2 = [(x / 1e-6)-85 for x in locy2]
        Ex = [x / 1e6 for x in Ex]
        Ey = [x / 1e6 for x in Ey]
        Ex2 = [x / 1e6 for x in Ex2]
        Ey2 = [x / 1e6 for x in Ey2]
        hammer.exportCsv(Vy, Ex, Ey, locy, './hammer.csv')
        hammer.exportCsv(Vy2, Ex2, Ey2, locy2, './hammer_x.csv')
        f, ax = plt.subplots(2)
        ax[0].plot(locy, Vy)
        ax[1].plot(locy, Ex)
        ax[1].plot(locy, Ey)
        f2, ax2 = plt.subplots(2)
        ax2[0].plot(locy2, Vy2)
        ax2[1].plot(locy2, Ex2)
        ax2[1].plot(locy2, Ey2)
```

```
# Corneometer CM825 sensor geometry
def CM825():
        # Number of electrodes / 2
        elnum = 20
        # Implement interdigital sensor geometry
        cm825 = interdigitalSensor(elnum, 250.0e-6, 50.0e-6, 1.0e-6, 1.8)
        cm825.drawSensor()
        thesisPresentation(cm825, 'Corneometer CM825', 60e-6, 20e-6, False)


# MoistureChecker
def MoistureChecker():
        # Number of electrodes / 2
        elnum = 20
        # Implement interdigital sensor geometry
        mc = interdigitalSensor(elnum, 850.0e-6, 250.0e-6, 1.0e-6, 1.8)
        mc.drawSensor()
        thesisPresentation(mc, 'MoistureChecker', 260e-6, 0)

# Custom sensor geometry
def none_main():
        print('Custom sensor geometry')

if __name__ == "__main__":
        # Command line arguments
        parser = argparse.ArgumentParser(description='Model configs')
        # Select log level
        parser.add_argument('--log', dest='log', default='warning')
        # Pick from standard models
        parser.add_argument('--std', dest='std', default='none')

        # Set selected log level configuration
        args = parser.parse_args()
        logging.basicConfig(level=getattr(logging, args.log.upper()))

        # Run simulation for selected model
        if args.std == 'cm825':
                CM825()
        elif args.std == 'hammer':
                MaxwellVsHammer()
        elif args.std == 'mc':
                MoistureChecker()
        elif args.std == 'e100':
                E100()
        elif args.std == 'cortex':
                Cortex()
        else:
                none_main()
        plt.show()
```

A.3 Hanno Hammer Analytical Model for Comb-Capacitance Fringe Fields in Octave

This piece of code implements functions as reported in [73].

```
clear all;
clear;
clc;

%//Analytical Model for Comb Capacitance Fringe Fields
%///Units in um and Volt
pi = 3.1415;
N = 10;
Nstep = 1;
e0 = 8.854e-12;
w = 2e-6;
d = 2e-6;
xmin = -w;
xmax = w;
ymin = 0e-6;
ymax = 20e-6;
y_height = 0.1e-6;
x_width = 0;
xy_step = 0.1e-6;
phi0 = 3.6; %//volt
study = "x" % Change x to y to study y displacement

function ak_ret = ak_f(k, width, distance)
        ak_ret = (2*k+1)*(pi/(width + distance));
endfunction

% Calculate Ak variable
function AKcap_ret = AKcap_f(PHI_0, k, width, distance)
        AKcap_ret =
        ( (4*PHI_0)/(distance * (width + distance) *
        (ak_f(k, width, distance)^2) ) ) *
        ( cos(ak_f(k, width, distance)* (width/2) ));
endfunction

% Calculate electric potential
function PHI_ret =
phi_f(Nmin, Nstep, Nmax, PHI_0, width, distance,x ,y)
        result = 0;
        for summer=Nmin:Nstep:Nmax
                result = result +
                (AKcap_f(PHI_0, summer, width, distance) )*
                (cos(ak_f(summer, width, distance)*x)) *
                exp(-ak_f(summer, width, distance)*y);
        end
        PHI_ret = result;
endfunction

% Calculate Ex
function Ex_ret =
EX_f(Nmin, Nstep, Nmax, PHI_0, width, distance,x ,y)
        result = 0;
        for summer=Nmin:Nstep:Nmax
                result = result +
                (AKcap_f(PHI_0, summer, width, distance) *
                ak_f(summer, width, distance) )*
                (sin(ak_f(summer, width, distance)*x)) *
                exp(-ak_f(summer, width, distance)*y);
        end
        Ex_ret = result;
endfunction
```

```
% Calculate Ey
function Ey_ret =
EY_f(Nmin, Nstep, Nmax, PHI_0, width, distance,x ,y)
        result = 0;
        for summer=Nmin:Nstep:Nmax
                result = result +
                (AKcap_f(PHI_0, summer, width, distance) *
                ak_f(summer, width, distance) ) *
                (cos(ak_f(summer, width, distance)*x)) *
                exp(-ak_f(summer, width, distance)*y);
        end
        Ey_ret = result;
endfunction

% (Main) Iterate through linear segment points
xindex = 1;
yindex = 1;
if study == "x" % if study X
        potential = zeros( round((xmax-xmin)/xy_step),1 );
        EX_array = zeros( round((xmax-xmin)/xy_step),1 );
        EY_array = zeros( round((xmax-xmin)/xy_step),1 );
        for x=xmin:xy_step:xmax
                potential(xindex,yindex) =
                phi_f(0, Nstep, N, phi0, w, d, x, y_height);
                EX_array(xindex,yindex) =
                EX_f(0, Nstep, N, phi0, w, d, x, y_height);
                EY_array(xindex,yindex) =
                EY_f(0, Nstep, N, phi0, w, d, x, y_height);
                xindex = xindex +1;
        end
else            % else if study y
        potential = zeros( round((ymax-ymin)/xy_step),1 );
        EX_array = zeros( round((ymax-ymin)/xy_step),1 );
        EY_array = zeros( round((ymax-ymin)/xy_step),1 );
        for y=ymin:xy_step:ymax
                potential(xindex,yindex) =
                phi_f(0, Nstep, N, phi0, w, d, x_width, y);
                yindex = yindex +1;
        end
end

% Plot data
if study == "y"
        figure;
        plot((ymin:xy_step:ymax)*1e6, potential);
        xlabel("y[um]");
        ylabel(["Potential [V] at height="
        mat2str(y_height) "um"]);
else
        figure;
        plot(xmin:xy_step:xmax, potential);
        xlabel("x[um]");
        ylabel(["Potential [V] at height="
        mat2str(y_height) "um"]);
        figure;
        plot(xmin:xy_step:xmax, EX_array*1e-6);
        xlabel("x[um]", "fontsize", 12);
        ylabel(["Ex[V/um] at height=",
        mat2str(y_height), "um"], "fontsize", 12);
```

```
        figure;
        plot(xmin:xy_step:xmax, EY_array*1e-6);
        xlabel("x[um]", "fontsize", 12);
        ylabel(["Ey[V/um] at height=",
        mat2str(y_height), "um"], "fontsize", 12);
end
```

A.4 Cortex Hypothetical Measurement Principle Circuit Simulation

```
clear
clear all;
clc;
colorsplot =["k-"; "r--";"g:";"b-.";"k-:"];

function ZC = zccalc(C, frequency)
        Xc = 1/(2*pi*frequency*C);
        ZC = complex(0, -Xc);
endfunction


function ZR = zrcalc(R)
        ZR = complex(R, 0);
endfunction

function [Z] = RCinparallel(R, C, frequency)
        Zc = zccalc(C, frequency);
        Zr = zrcalc(R);
        Z = (Zc*Zr)/(Zc+Zr);
endfunction

function [Z] = RCinseries(R, C, frequency)
        Zc = zccalc(C, frequency);
        Zr = zrcalc(R);
        Z = (Zc+Zr);
endfunction

function Z = ZZinparallel(Z1, Z2)
        Z = (Z1*Z2)/(Z1+Z2);
endfunction

function Z = ZZinseries(Z1, Z2)
        Z = Z1+Z2;
endfunction

function [Sensing, Orange, White] =
        findsignals(Rin, Cin,
                SignalIn, SINpeak,
                Blue, frequency)

        if Cin == 0
                Zs = Rin;
        elseif Rin == 0
                Zs = zccalc(Cin, frequency);
        else
```

```
                Zs = RCinparallel(Rin, Cin, frequency);
        endif
        Z1 = 0.1e3;
        Z2 = 100e6;
        Z2s = ZZinparallel(Z2, Zs);
        Z12s = ZZinseries(Z1, Z2s);

        Parallel = abs(Z2s);
        Sensing = SignalIn - (SignalIn/(Z1+Parallel))*Z1;
        Orange = Sensing + Blue - SignalIn;
        White = Sensing + Blue;
endfunction

tstart = 0;
tstep = 0.0000002;
tstop = 0.00002;%secs
t = tstart:tstep:tstop;

Freqin = 100e3; %Hz
Vpeak = 1.3;
Vin = Vpeak*sin(2*pi*Freqin*t);
Vmid = 2.5;

figure;
hold on;
cind = 1;
for Cin = 5.0695e-12:0.5e-10:2.4e-10
        index1 = 1;
        for rin=200e3:-1000:15e2
                [Vsen, Vor, Vwh] =
                        findsignals(rin, Cin, Vin, Vpeak, Vmid, Freqin);
                VwhtMDC = Vwh-Vmid;
                Vspeak(index1) =
                        abs( (VwhtMDC(20))/(sin(2*pi*Freqin*t(20))) );
                Rt(index1) = rin;
                St(index1) = 1/rin;
                index1 = index1+1;
        end
        p1 = plot(St, Vspeak, colorsplot(cind,:), 'linewidth',2);
        legstr(cind) = Cin;
        cind = cind + 1;
end

leg1 = legend(strcat(num2str(legstr(:)),'F'));
set(leg1, 'fontsize', 13);
xlabel('Conductance[S]','fontsize',13);
ylabel('Vpeak[V]','fontsize',13)
title('Effect of skin capacitance on Cortex linearity',
        'fontsize',13);
hold off;
```

A.5 Cortex Capacitance Calculation

```
clear
clear all;
clc;
```

```
function [ElectPot]= annularpotential(z, sigma,k, rin, rout)
        ElectPot = (sigma/(2*k)) * (sqrt(rout^2+z^2) - sqrt(rin^2+z^2));
endfunction

function [ElectField] = annularfield(z, sigma, k, rin, rout);
        ElectField = -(sigma/(2*k))*( (z/sqrt(z^2+rout^2)) - (z/sqrt(z^2+rin^2)));
        if isnan(ElectField)
                ElectField = 0;
        endif
endfunction


Rin1 = 0.75e-3
Rout1 = 3.1e-3
S1 = pi * (Rout1^2 - Rin1^2)
Rin2 = 3.9e-3
Rout2 = 7.8e-3
S2 = pi * (Rout2^2 - Rin2^2)
Rin3 = 8.6e-3
Rout3 = 12.7e-3
S3 = pi * (Rout3^2 - Rin3^2)
z = 0
e0 = 1 * 8.854e-12
phi_t = -1.3


G1 = (sqrt(Rout1^2+z^2) - sqrt(Rin1^2+z^2))
G2 = (sqrt(Rout2^2+z^2) - sqrt(Rin2^2+z^2))
G3 = (sqrt(Rout3^2+z^2) - sqrt(Rin3^2+z^2))

sigma = phi_t / ((((S1+S3)*G2)/(2*e0*S2)) - (G1/(2*e0)) - (G3/(2*e0)))

sigmaPlus = -sigma * (S1 + S3) / S2
Qplus = sigmaPlus * S2
C = Qplus / abs(phi_t)
```